Experimental Study on Mechanical Behavior of Reinforced Liquefied Stabilized Soil Subjected to Monotonic and Cyclic Loading

By

HUNG KHAC LE

Course of Advanced Sustainable and Environmental Engineering

Division of Engineering

MURORAN INSTITUTE OF TECHNOLOGY

March 2023

ACKNOWLEDGEMENTS

I would like to take this opportunity to express my gratitude to those who have contributed to the development of this thesis.

Firstly, I am greatly indebted to my supervisor Professor Yukihiro Kohata for his encouragement, guidance, and support, and for many valuable discussions throughout the course of this study. His passion and enthusiasm in his work have always inspired me. Having the opportunity to work with Prof. Yukihiro Kohata was an experience that helped me gain a broader perspective and insight into many areas of life.

I would also like to thank my co-supervisors, Professor Shima Kawamura and Associate Professor Noriyuki Sugata, for their guidance, encouragement, and insightful comments on the revision of my doctoral thesis and the doctoral thesis defense presentation.

I would also like to express my deep gratitude to my teacher, Associate Professor Nghiem Manh Hien, for the useful discussions, suggestions and encouragement throughout the course of this study.

I am grateful to all the staff of the International Center for Relations of Muroran Institute of Technology for making my family life in Hokkaido really comfortable and enjoyable. They always extended instant help whenever I needed. Especially thanks to Associate Professor Naoko Yamaji, who gave me the very first Japanese classes patiently and carefully.

I would like to express my gratitude to all Kohata's laboratory members, Mr. Moteki, Mr. Onodera, Mr. Okada, Ms. Watanabe, and Ms. Xi, for their friendship, kindness, timely help, and encouragement. They not only support me in my experiment but also help me enjoy the life in Muroran.

I am grateful to the Geotechnical Department, Civil Engineering Faculty, and Hanoi Architectural University in Vietnam, for creating good conditions to study at MIT. I would also like to thank Assoc. Prof. Le Quan, Assoc. Prof. Vuong Van Thanh, Assoc. Prof. Nguyen Ngoc Phuong, Assoc. Prof. Vu Hoang Hiep, Dr. Nguyen Cong Giang, Dr. Duong Quang Hung, Dr. Nguyen Ngoc Thanh, and Dr. Dao Minh Hieu for their introduction and recommendation and supported me in applying for this Ph.D. position at MIT.

Last but not least, I am profoundly thankful to my parents, parents-in-law, brother, and sister for their encouragement. Finally, to my wife, Le Thi Thu Huong, and my son, Le Khac Hai Long, who has been by my side throughout. We got there in the end. I am grateful for their encouragement, lasting love, patience, and unending support. I could not have done this without them.

ABSTRACT

In this study, the mechanical behavior of reinforced and unreinforced Liquefied Stabilized Soil (LSS) subjected to monotonic and cyclic loading is discussed based on a database with about Consolidated-Undrained monotonic and cyclic triaxial tests of 102 cases.

In the monotonic tests, the influences of slurry density and curing time on the strength and deformation of LSS are investigated. Also, LSS mixed with the pulverized newspaper in the amount of 0 and 10 kg/m^3 cured laboratory and in-situ are compared and investigated. Based on the test results, the effect of slurry density on the strength of LSS was found to be greater than the effect of curing time. The pre-peak behavior of the q~ε_a curve became more non-linear under the effect of changing slurry density, in contrast to the effect of curing time. Moreover, the damage degree of LSS with shearing becomes small with curing time, while it seems to be rather independent of slurry density. With in-situ LSS, the influence of curing time on the initial Young's modulus, E_0, is lower than the effect of slurry density.

In the cyclic tests, in order to investigate the effect of cyclic load on the deformation property, the deviator stress amplitude, the initial stress, consolidation pressure, strain rate, and the control method (stress vs. strain cycles) were changed and LSS material which includes slurry density, fiber material, and cement on LSS cured 28 days at the laboratory have been also varied. Based on the test results, it is found that the true liquefaction ($q = p = 0$) did not reach reinforced and unreinforced LSS. The failure mode is highly dependent on the cyclic deviator stress amplitude (σ_d) and initial deviator stress (σ_s). For symmetrical loading ($\sigma_s = 0$), the pore water pressure and double amplitude axial strain grew with an increasing number of cycles. LSS mixed with fiber material finally collapsed due to too large strain amplitudes. In the final stage, the loops of effective stress indicate a "Butterfly" stress path shape. For nonsymmetrical loading ($\sigma_s > 0$), an accumulation of compressional axial strain with each subsequent cycle occurred, while the mobilized double amplitude axial strain remained almost constant. Therefore, the failure criterion was fulfilled due to an excessive accumulation of permanent strains. The shape of the stress loop at the final stage did not pass the "butterfly" shape or lens shape to migrate to pass over the Critical State Line (CSL), then return to the touch again of the failure envelope. It means the LSS mixed fiber material tends to dilate before reaching the failure criterion. The range of critical cyclic stress ratio (*CSR*), which indicates the limitation of stress level, was between 0.275 to 0.344. If the stress level is lower than that value, the LSS sample is more dilative by accumulating permanent axial strain and does not reach failure. The cyclic shear resistance of LSS decreases when reducing the confining pressure, displacement rate and cement content. In contrast, the cyclic shear resistance increases when adding fiber and increasing slurry density.

The Finite Element Method (FEM) is used widely in the analysis of seismic vibration. However, the results depend critically on the constitutive models used and the model parameters adopted in the numerical analyses. The implementation of a specific model to analyze the behavior of LSS mixed fiber material under cyclic loading, the Ramberg-Osgood model, in the Delphi code is performed. Based on the result of the comparison of model simulations with experimental data, the overall is able to apply the Ramberg-Osgood model to evaluate the cyclic loading behavior of LSS, and dynamic parameters should be calibrated properly.

In summary, a number of new findings were presented regarding the mechanical behavior of reinforced, liquefied stabilized soils subjected to monotonic and cyclic loading.

TABLE OF CONTENTS

LIST OF TABLES

LIST OF FIGURES

CHAPTER 1
INTRODUCTION

1. Introduction

1.1. Problem Statement

Nowadays, environmental issues are arising from growing urbanization, especially in developing countries. Urban construction generates large amounts of construction waste soil that may not be appropriate for reuse in construction but may be harmful to the environment if not properly treated. Moreover, due to its small land area, the city confronts environmental issues, such as a lack of final disposal sites, and resource limitations, such as concerns about the potential exhaustion of mineral resources. The waste and recycling problem has become a societal issue. This problem has received considerable attention. Therefore, finding a suitable use for recycled materials is desirable.

In addition, in recent years, earthquakes have caused heavy damage to buildings and infrastructure. One of the causes of heavy damage due to earthquake motions is the effect of soil in amplifying bedrock ground motions. Improving the soil conditions of sites in order to mitigate earthquake damage can be one of the methods of enhancing site conditions and its effects on seismic site response. Therefore, many studies have been conducted to investigate the effect of various additives to improve the liquefaction resistance of the soil using experimental devices. For instance, Clough et al. (1989) investigated the effect of cementation on the liquefaction behavior of sand by performing a series of triaxial and cubical cyclic shear tests. To do so, they modified an originally monotonic cubical cyclic shear apparatus to a dynamic device model to model the seismic loadings. They focused their studies on unit weight and the level of cementation and indicated that cemented sand has a liquefaction resistance greater than un-cemented sand. It was also mentioned that increasing both unit weight and percentage of cementation increase the liquefaction resistance, however, when the cementation content reaches to a specific percentage, it reduces the effectiveness of the unit weight. They also investigated the relation of the unconfined compressive Strength (UCS) of the cemented sand with liquefaction and concluded that when the UCS value is greater than 10 t/m2, the soil does not liquefy. In a similar study on liquefaction resistance of an artificially cemented sand using cyclic triaxial resonant column tests by Saxena et al. (1988), the effect of cement content, curing time, relative density, and effective confining pressure was investigated. They indicated that the liquefaction resistance increased when a low percentage of cement was added to the specimens. It was also concluded that the liquefaction resistance of the cemented sand increased by increasing the curing period and relative density.

In another study, Maher et al. (1994) investigated the effect of grouting on the liquefaction resistance of the sand by performing a series of consolidation drained (CD) and consolidation undrained (CU) cyclic and monotonic triaxial tests. They investigated the effect of parameters such as grouting types (i.e., sodium silicate, acrylate polymer gel, and micro-fine cement), curing periods, void ratios, and cyclic stress ratios (CSR). It was indicated that the application of grouting gels is effective in improving the liquefaction resistance of the sand. It was also indicated that increasing the liquefaction resistance due to curing time relates to the type of grouting gel used. For instance, in the case of the sodium silicate or acrylate polymer, maximum resistance was recorded after the first 14 days of the curing period, and no remarkable increase in liquefaction resistance was recorded after 60 days curing period. However, for the case of micro-fine cement, the recoded maximum liquefaction resistance was up to 28 days curing period. The results showed that an increase in confining pressure caused a greater strength and, accordingly, a higher liquefaction resistance. They added that increasing the grouting

content improved the liquefaction resistance of the sand. However, it increased the brittleness and fragility of the specimens from the other side.

In another study, Liao et al. (2003) investigated the effect of colloid silica grouting on the liquefaction resistance of the sand by performing a series of cyclic triaxial tests. They indicated that despite of low strength of the used grouting gel, grouted sand has a greater resistance against liquefaction in comparison with the control specimen. It was also mentioned that a sudden axial stain was recorded immediately after liquefaction in the case of un-grouted sand. However, this deformation was gradual in the case of grouted sand.

Only some studies investigated innovative materials' effect on soil liquefaction behavior. For instance, Boominathan and Hari (2002) investigated the effect of reinforcement (i.e., randomly distributed fibers) on fly ash by performing a series of stress-controlled triaxial tests. They investigated the effect of relative density, effective confining pressure, the aspect ratio of the fiber, and cyclic stress ratio (CSR) on the liquefaction resistance of fly ash. They concluded that the reinforced specimens have greater resistance against liquefaction in lower confining pressure. They also indicated that increasing the reinforcement agent improved the liquefaction resistance when the specimens were prepared at a lower relative density. It is mentioned that 2% fiber is the most effective amount to reduce the effect of liquefaction (Boominathan & Hari, 2002).

In another study, Maher and Ho (2014) investigated the effect of fiber reinforcement on monotonic and cyclic loadings by performing a series of triaxial and splitting tension tests. Results showed that adding a reinforcement agent increases the cyclic strength and tensile strength of the specimens.

In another study on reinforcement additives, Noorzad and Fardad Amini (2014) investigated the effect of randomly distributed soil on the liquefaction strength of the sand. Similarly, they concluded that the presence of the reinforcement agent effectively improves the liquefaction resistance of the Babolsar sand.

In another similar study, Maheshwari et al. (2012) investigated the liquefaction resistance of the sand reinforced by geogrid and two types of fiber using shaking table tests. They recorded a reduction in the specimens' maximum pore water pressure ratio when the fibers or geogrid were added to the soil. More reduction was recorded when more additives were added to the soil.

Uchimura et al. (2007) investigated the effect of tire chips on the liquefaction resistance of sand as a backfill material in the case of a buried pipe by performing a series of cyclic triaxial and shaking table tests. They concluded that adding tire chips in sand effectively improves the liquefaction resistance of a buried pipe and reduces the uplifting problem. Similarly, it was mentioned that increasing the relative density in tire-treated specimens effectively improves the sand's liquefaction resistance.

The literature review on past studies on the improvement of the liquefaction resistance of soil shows that most of the investigations have been conducted on traditional agents such as cement. Also, the literature review shows that previous studies mainly applied reinforcement agents to improve the liquefaction resistance of the soil, and no study has considered the effect of other innovative materials on the cyclic resistance of the soil.

In Japan, “Liquefied-Stabilized Soil” (LSS), one of premixing cement treated-soil, has recently been increasing for backfilling processes owing to its advantages. The excavated soils discharged from construction projects can be recycled to become backfilling material. The application of LSS to improve ground has been successfully achieved in many construction projects. The technology involves adding cement stabilizer to slurry soil and create stability of the soil layer without compaction. In addition, the advantages of LSS have been shown

Table 1-1 Main studies conducted on improvement of the liquefaction resistance of soil using different agents

No.	Reference	Used by-product agent
1	Chegenizadeh et al. (2018a)	Bulk continuous filament (BCF)
2	Mashiri et al. (2016)	Tire chips
3	Hong et al. (2015)	Tire chips
4	Noorzad and Fardad Amini. (2014)	Randomly distributed fiber
5	Naeini and Gholampoor. (2014).	Geotextile
6	Hamidi and Hooresfand. (2013)	Reinforced cemented sand
7	Maheshwari et al. (2012)	Geogrid
8	Kaneko et al. (2012)	Rubber
9	Neaz Sheikh et al. (2012).	Tire chips
10	Maheshwari et al. (2012)	Geogrid
11	Ibraim et al. (2010)	Discrete flexible fiber (DFF)
12	Towhata (2008).	Tire chips
13	Uchimura et al. (2007)	Tire chips
14	Liao et al. (2003)	Colloid silica grouting
15	Boominathan and Hari (2002)	Fiber
16	Haeri et al. (2000)	Geotextile reinforcement.
17	Vercueil et al. (1997)	Woven and non-woven geosynthetics
18	Maher et al. (1994)	Grouting
19	Maher and Ho. (1993)	Fiber-reinforced cemented
20	Clough et al. (1989)	Cementation
21	Saxena et al. (1988)	Cement content

various types of excavated soils, which is not necessarily good quality material to have the appropriate fluidity by adjusting the density of soft soil with high moisture content can be effectively used. Different LSS can be created from the slurry-based premixed stabilized soil using high-quality soil materials. However, there is concern that the increased use of cement-based solidification material in LSS increases their strength and causes them to behave brittlely, reducing their seismic resistance. In order to improve brittle behavior, Professor Kohata of Muroran Institute of Technology (2002) used the method of mixing with shredded newspaper fiber materials; from the test results, after mixing the fiber materials, the brittleness after the peak improved. After that, there are many studies to investigate the strength and deformation of LSS, and some typical research is presented as follows.

The previous research in 2010 Giang NC (2010) was performed with both LSS using NSF-clay, which is fine powder clay bought in the Japanese market, and Vinh Phuc-Clay, which spread in the Hanoi area as an original material. A series of Consolidated–Undrained triaxial compression tests was conducted under confining pressure of 98 kPa of Vinh Phuc-Clay LSS, and NSF-Clay mixed by fibered material content of 0, 10, and 20 kg/m3 at 56 days, respectively. It concluded that the strength and deformation behaviors of both LSS tend to be similar. In this study, the ground vibration behaviors around the cut and cover tunnel in the case of using LSS have been evaluated by 2-D FEM in comparison with hill-cut soil material. These results indicated clearly that there are effects on controlling ground vibration induced by traffic load.

In 2015, Hung DQ., investigated the effect of time-dependency on strength and deformation characteristics of LSS mixed with fibered material was evaluated, and it was found that the effect of time-dependency is not seen in the stress-strain curve independent of curing time. The difference in triaxial shear property of LSS mixed with fiber material cured in the laboratory and field was also investigated to be carried out a series of CUB tests for both specimens of LSS mixed with fiber material amounts of 0 and 20 kg/m^3 prepared by trimming LSS

retrieved from a model ground by block sampling and cured in the laboratory at curing times of 28 and 56 days, respectively. In this research, a procedure for predicting train-induced vibration from railway tunnels in conformity with the condition of Vietnam has been established. The 2-D FEM analyzed the vibration propagation from the tunnel into the ground surface. Using the established procedure, mitigation of train-induced vibration by using LSS for backfill ground of cut and cover tunnel was evaluated as well. It is considered that LSS has an effective potential in the mitigation of train-induced vibration.

The 2019 study is to use LSS as backfill material in the construction project in Hanoi (Anh, 2019). The central part of this study carried out experiments and analytical work to study the advantages of LSS and LSS mixed with fiber materials. Research is divided into experimental research and simulation research. Experimental research is divided into indoor research and outdoor research. In the part of the experimental study, two kinds of mud are used, which are 1.280g / cm^3 ($D_{\rho f}$ = 100%) and 1.216g / cm^3 ($D_{\rho f}$ = 95%), and the LSS with 0,10kg / m^3 (Pc-0, 10) fiber materials are mixed and cured simultaneously indoors and outdoors (28 days, 56 days). The CUB test was performed at a constant strain rate of 0.054% / min and an effective confining pressure of 98 kPa. By adding fiber materials, the brittleness of the LSS outside the peak is increased. The density of the mud has a significant influence on the degree of shear damage. The damage degree tends to decrease after the fiber material is added. In this study, according to the numerical analysis results on mitigation of vehicle-induced vibration in the case using LSS as backfill material by the established analysis method, it is found that the application of LSS can significantly reduce ground vibration.

The research in 2020 Yujie Cui (2020) conducted a series of triaxial compression tests and unconfined compression tests with LSS specimens prepared in different slurry densities of 1.216, 1.280 g/cm^3, cement content of 80, 100 kg/m^3, and the fiber content of 0, 10 kg/m^3 to investigate the influence of slurry density on strength and deformation properties of LSS reinforced with fiber material. The results showed that a slight decrease in slurry density could decrease the peak stress of LSS remarkably. Meanwhile, the change in cement content can affect peak strength as well as the decreasing rate of E_{tan}/E_0 in the early loading stage. In addition, by adding fiber material, the local damage caused by shearing and the brittleness were improved.

In 2021, Vuong NQ., a series of triaxial compression tests on the specimens mixed with a material amount of 0 and 10 kg/m3 cured in the field at curing times of 28 and 56 days. Furthermore, the applicability of an evaluation of stiffness by the Portable Falling Weight Deflectometer (PFWD) test at a backfilling ground by LSS mixed with fiber material was investigated. Based on test results, the influence of curing temperature strength and deformation properties of LSS and the K-value by PFWD was discussed. In this research, the effect of backfilling material on the building and ground under the earthquake is analyzed by the finite element method (FEM). A 3-D model of ground and construction was simulated in ABAQUS software. It concluded that the LSS and LSS with fiber have an effective potential to reduce the seismic motion on the building and the surrounding soil environment.

As mentioned above, Table 1-1 shows a summary of the conducted studies on the improvement of the cyclic resistance of soil using different agents. As shown, past studies on the improvement of the liquefaction resistance of soil have been conducted to investigate the effect of traditional agents such as cement and geotextile, and numerous studies have investigated the strength and deformation properties of LSS with fiber. However, no comprehensive investigation of LSS with fiber under various combination conditions has been performed.

Especially the effect of various slurry densities and longer curing times on the strength and deformation properties of LSS-cured in-situ conditions needs to be clarified.

In addition, the previous research on applying LSS mixed fiber material as a backfilling to mitigate vehicle-induced vibration or seismic motion by the finite element method (FEM) was conducted from 2010. It is found that the application of reinforced LSS can significantly reduce seismic vibration. Nevertheless, there is no data or experiment on LSS mixed fiber material subjected to cyclic load. All dynamic input parameters of LSS calculated from static tests were found in these previous studies. Furthermore, in Geotechnical Earthquake Engineering, the behavior and dynamic parameter of soil under cyclic load play an important role in soil responses to seismic motion. A major consequence is linked to the fact that stiffness degrades, energy dissipation increase, and the shear velocity of the soil decay for increasing shear strains, leading to a fundamental frequency and amplitude for the vibration modes getting less significant. Therefore, research on LSS mixed fiber material subjected to cyclic load and the development of a constitutive mode to account for the cyclic behavior of LSS is essential and meaningful.

1.2. Research Objectives

Firstly, this study investigates the strength and deformation properties of LSS prepared by various conditions. Based on the result of 48 Consolidated-Undrained triaxial compression tests by a constant axial strain rate 0.054 %/min, with small unloading and reloading during the monotonic loading, the effect of curing times of 42, 56, 80, and 126 days and slurry densities, including $D_{\rho f}$ =1.216 g/cm^3, $D_{\rho f}$ =1.218 g/cm^3, and $D_{\rho f}$ =1.344 g/cm^3, respectively, on the strength and deformation properties of LSS cured laboratory and in-situ were discussed. Also, the comparison of LSS mixed with the pulverized newspaper in the amounts of 0 and 10 kg/cm^3 cured laboratory and in-situ is investigated.

Secondly, the behavior reinforced and unreinforced LSS subjected to cyclic loading with an emphasis on the samples cured in the laboratory and 28 days of curing time is investigated. A database with about 54 undrained monotonic and cyclic triaxial tests on LSS is presented. In the cyclic test, the effect of cyclic test variables, which including deviator stress amplitude, the initial stress, consolidation pressure, displacement rate, and the control (stress vs. strain cycles) and LSS material variables which include slurry density, fiber material, and cement on LSS is studied. Moreover, secant shear modulus, normalized equivalent Young's modulus, and damping ratio characteristic of LSS will be evaluated at various conditions. To achieve these research objectives, development and modifications will be made to the existing triaxial device at Muroran Institute Technology, and it will be enhanced to precisely measure and add more features to apply cyclic loading.

Finally, the implementation of a specific model to analyze the behavior of LSS mixed fiber material under cyclic loading, the Ramberg-Osgood model, in the Delphi code. The mathematical description of the model is thoroughly presented, as well as several issues concerning numerical implementation. Based on the results of cyclic tests on LSS, a set of dynamic parameters is proposed. Finally, several validation tests are presented.

1.3. Organization of Thesis

As seen in Figure 1-1, this dissertation contains eight chapters. The introduction (Chapter 1) describes the problem statements, the objectives of the research, and the organization of the dissertation.

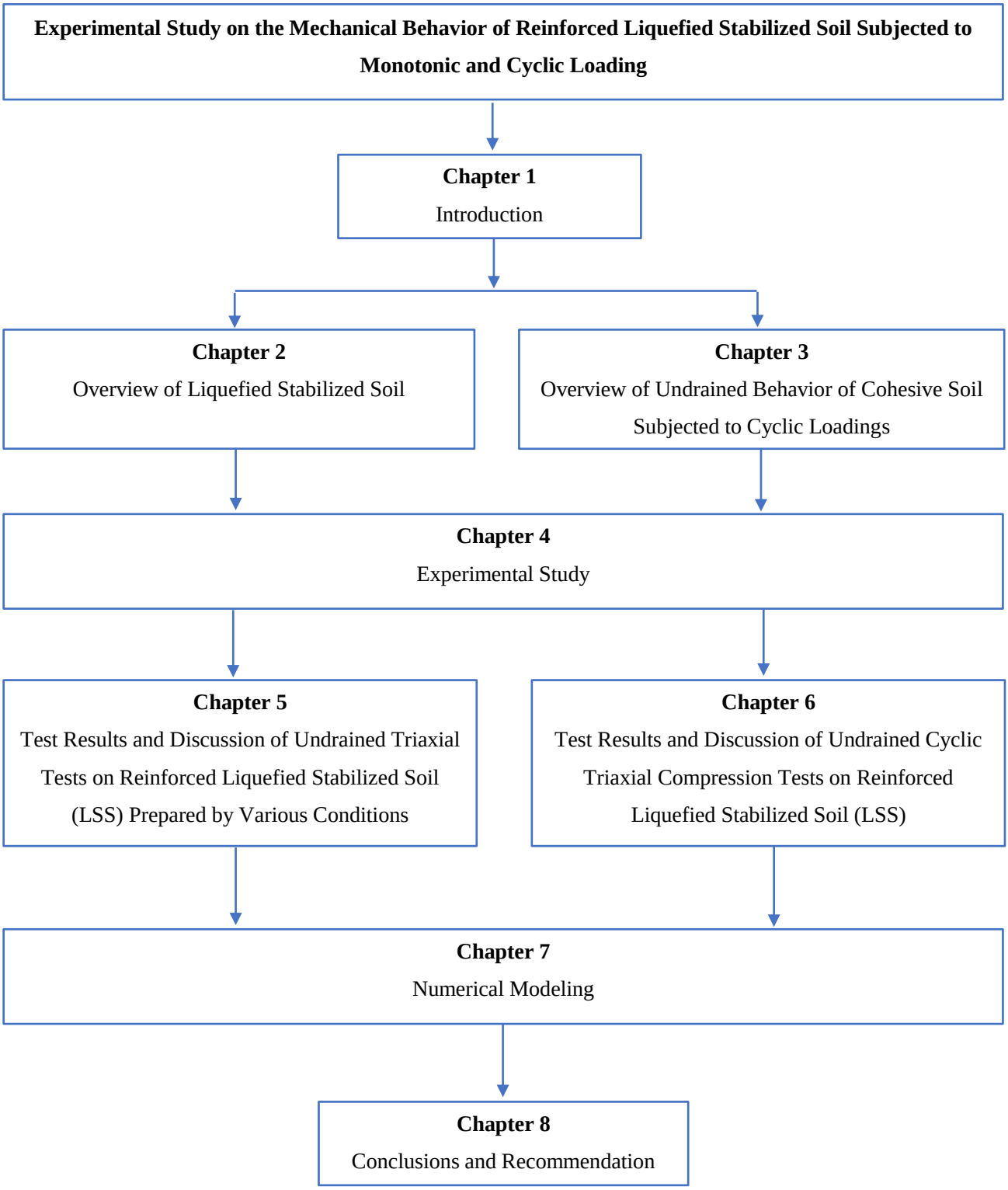

Figure 1-1 Flow chart of this dissertation

CHAPTER 2

OVERVIEW OF LIQUEFIED STABILIZED SOIL

2. Overview of Liquefied Stabilized Soil

2.1. Introduction

Liquefied soil stabilizing method (LSS) is a process of improving geotechnical properties to stratify engineering requirements. Until now, numerous kinds of stabilizers including cement, lime, fly ash, etc. were used as soil additives to improve their properties. The LSS manufacturing process utilizes soil that has been excavated in construction projects and which would otherwise be discharged to the natural environment as soil waste. LSS can be used for confined spaces or excavation areas and it can be easily placed without vibration and compaction. The characteristics, benefits, advantages, and applications of LSS has been shown such as:

Characteristics:

- Impermeability

Benefit:

- Reduce the cost of construction projects
- Reduce manpower
- Protect environment

Advantage:

- Excavated out easily
- Quick setting time
- Convenient compared to normal backfilling
- Faster than normal backfilling
- No soil stockpile is needed

Application:

- Backfill using a concrete pump
- Cavities and excavated trenches can be backfilled easily

2.2. Component of Liquefied Stabilized Soil

Liquefied stabilized soil involves the use of binder materials in soils to improve its geotechnical properties such as compressibility, strength, permeability, flexibility and durability. The components of liquefied stabilized soil include soils, binders (cementitious materials). (Figure 2-1)

Figure 2-1 The components of liquified stabilized soil

2.2.1. Base Materials

Most soils in liquefied stabilized soil method are soft soils. The stabilization has been performed to achieve desirable engineering properties. The main purpose of liquefied stabilized method is to recycle excavated soil for backfilling processes for construction projects. Therefore, almost types of excavated soils can be used for this method. However, fine-grained granular materials are the easiest to stabilize due to a large surface area in their contact diameter. The excavated soils can be modified to perform mainly with the purpose of improving their usability in construction. At present, excavated soils are stabilized by binders which are selected in relation to the type of soil. The stabilization has improved the strength of the soils and their resistance to softening.

In this study, NSF-CLAY was used as a homogenous base material, which was a commercially available cohesive soil with very clearly defined physical properties shown in Table 2-1.

Table 2-1 Physical parameters of NSF-Clay

Physical parameters	Values
Particle density ρ_s (g/cm^3)	2.762
Liquid limit W_L (%)	60.15
Plastic limit W_P (%)	35.69
Plasticity index I_P	24.46
$M (=q_f/p'_f)$	1.20

2.2.2. Cementitious Materials

In stabilizing a soil, these are hydraulic (primary binders) or non-hydraulic (secondary binders) materials that when in contact with water or in the presence of pozzolanic minerals reacts with water to form cementitious composite materials. The commonly used binders are cement, lime or fly ash. In order to decide which binder should be used, the analysis have been performed based on test results and in fact condition of projects.

Cement

Cement had been known as the binding agent since the invention of soil stabilization technology in the 1960's. It may be considered as primary stabilizing agent or hydraulic binder because it can be used alone to bring about the stabilizing action required. Cement reaction is not dependent on soil minerals, and the key role is its reaction with water that may be available in any soil. This can be the reason why cement is used to stabilize a wide range of soils. Numerous types of cement are available in the market; these are ordinary Portland cement, blast furnace cement, sulfate resistant cement and high alumina cement. Usually the choice of cement depends on type of soil to be treated and desired final strength. Hydration process is a process under which cement reaction takes place. The process starts when cement is mixed with water and other components for a desired application resulting into hardening phenomena. The hardening (setting) of cement will enclose soil as glue, but it will not change the structure of soil. The hydration reaction is slow proceeding from the surface of the cement grains and the Centre of the grains may remain unhydrated. Cement hydration is a complex process with a complex series of unknown chemical reactions. However, this process can be affected by presence of foreign matters or impurities, water-cement ratio, curing temperature, the presence of additives, and specific surface of the mixture.

Lime

Lime is the oldest traditional stabilizer used for soil stabilization. Lime-treated soil was studied extensively in the literature. Numerous field and laboratory studies were conducted to evaluate the improvement of geotechnical properties by lime. Several types of soils, lime contents and curing conditions and methodologies were used for this purpose. The mechanism of treatment comprised hydration, cation exchange, flocculation-sag glomeration of soil particles and pozzolanic reaction to form Calcium Silicate Hydrate (C-S-H) and Calcium Aluminate Hydrate (C-A-H) as cementitious materials. The factors affecting lime treated soil are lime content, curing time, curing temperature and soil mineralogy. Soil-lime mixtures have advantages and disadvantages. Its advantages comprise significantly increase soil strength, reduce plasticity (increase workability) and increases

soil durability. In addition, a considerable reduction in consolidation settlement and improve compressibility characteristics were observed. Unclear behavior was noted for the permeability of soil lime mixture when compared with the original soil. Carbonation, sulfate attack and environment impact are a number of the disadvantages of lime-treated soil. Some studies were conducted to provide some guidelines to reduce the deleterious effects of these cons. Magnesium oxide and hydroxide can be proposed as alternative for lime since they possess chemical characteristics make them eligible to overcome the mentioned cons. Moreover, the result of few conducted studies used magnesium-based additives to stabilize the soil was significant improvement achieved in soil strength, workability and durability. Therefore, it is needed to conduct extensive studies to determine the efficiency of this material in soil stabilization.

Fly ash

Fly ash has been used successfully in many projects to improve the strength characteristics of soils. Fly ash can be used to stabilize bases or subgrades, to stabilize backfill to reduce lateral earth pressures and to stabilize embankments to improve slope stability. Typical stabilized soil depths are 15 to 46 centimeters. The primary reason fly ash is used in soil stabilization applications is to improve the compressive and shearing strength of soils. The compressive strength of fly ash treated soils is dependent on:

- To enhance strength properties
- Stabilize embankments
- To control shrink swell properties of expansive soils
- Drying agent to reduce soil moisture contents to permit compaction

Class C fly ash can be used as a stand-alone material because of its self-cementitious properties. Class F fly ash can be used in soil stabilization applications with the addition of a cementitious agent (lime, lime kiln dust, CKD, and cement). The self-cementitious behavior of fly ashes is determined by ASTM D 5239. This test provides a standard method for determining the compressive strength of cubes made with fly ash and water (water/fly ash weight ratio is 0.35), tested at seven days with standard moist curing.

The self-cementitious characteristics are ranked as shown below:

- Very self-cementing > 500 psi (3,400 kPa)
- Moderately self-cementing 100 - 500 psi (700 - 3,400 kPa)
- No self-cementing < 100 psi (700 kPa)

It should be noted that the results obtained from ASTM D 5239 only characterizes the cementitious characteristics of the fly ash-water blends and does not alone provide a basis to evaluate the potential interactions between the fly ash and soil or aggregate.

The use of fly ash in soil stabilization and soil modification may be subject to local environmental requirements pertaining to leaching and potential interaction with ground water and adjacent water courses.

Soil Stabilization to Improve Soil Strength

Fly ash has been used successfully in many projects to improve the strength characteristics of soils. Fly ash can be used to stabilize bases or subgrades, to stabilize backfill to reduce lateral earth pressures and to stabilize embankments to improve slope stability. Typical stabilized soil depths are 15 to 46 centimeters (6 to 18 inches). The primary reason fly ash is used in soil stabilization applications is to improve the compressive and shearing strength of soils. The compressive strength of fly ash treated soils is dependent on:

- In-place soil properties
- Delay time
- Moisture content at time of compaction
- Fly ash addition ratio

In this study, Geoset 200 provided by Taiheiyo Cement Co. was used as cement stabilizer, which was a cement-based solidifying agent for soft clay and problematic soil.

2.2.3. Fiber Material

As shown in Figure 2-2, newspaper to be ground into like cotton wool by a food processor was used as fiber materials in this study

Figure 2-2 Fiber material made by newspaper

2.3. Historical Development

The original concept comes from the United States, soil mixing was first developed by Intrusion-Prepakt, Inc. of Cleveland Ohio (Liver et al. 1954) as “Intrusion Grout Mixed-in-Place Piles”.

In 1961, the mixed in place already used under license for more than 300 000 lineal meters of piles in Japan for excavated support and groundwater control. Continued until early 1970’s by Seiko Kogyo Company, to be suggested by diaphragm walls and deep mixing method (Soil-Mix Wall). In addition, Herrin and Mitchen (1961) suggested that there is no one of optimum lime content with which maximum strength of lime stabilized soils can be expected under all condition. That is, for a specific condition of curing tine and soil type an optimum lime content which caused a maximum strength exists.

The development and research on deep mixing started from laboratory model tests in 1967 by the Port and Harbour Research Institute of Japanese Ministry of Transportation. Research was continued by Okumura, Terashi et al. through 1970’s including 1- investigation of lime-marine reaction, and 2- develop appropriate mixing equipment. Unconfined compressive strength (UCS) of 0.1 to 1 MPa achieved. Early equipment (Mark I-IV) used the first marine trial near Hamada Airport (10 m below water surface). In addition, Swedish Lime column method for treating soft clays under embankment using unslaked lime was researched (Kjeld Paus, Linden- Alimak AB, in cooperation with Swedish Geotechnical Institute, Euroc AB, and BPA Byggproduction AB). And then, this follows observations by Paus on fluid lime column installation in the United State.

In the late 1960’s, China reported to be considering implementing Depp lime mixing concept form Japan.

Development of Soil Mixed wall method for retaining walls, using overlap multiple augers was started in Japan by Seiko Kogyo Co. of Osaka in 1972 to improve lateral treatment continuity and homogeneity/quality of treated soil.

The first Japanese full-scale Deep Mixing project was conducted in 1974. First applications in reclaimed soft clay at Chiba (June) with and Applications elsewhere in Southeast Asia follow the same year. In addition, intensive trials conducted with Lime Columns at Ska Edeby Airport, Sweden: basic tests and assessment of drainage action (columns 15 m long and 0.5 m in diameter). In 1974, first detailed description of Lime Column method by Arrason et al. (Linden Alimaik AB). And the first similar trial embankment using Swedish Lime Column method in soft clay in Finland (6 m high, 8 m long; using 500-mm-diameter lime cement columns, in soft clay) in 1974.

In 1975, deep mixing's first appearance in an international forum in Bangalore, India, a Swedish paper on Lime Colum by Broms and Boman. In addition, a Japanese paper on Deep Lime Mixing (DLM) by Okumura and Terashi were presented to the Swedish paper on lime columns (Broms and Boman), and Japanese paper on DLM (Okumura and Terashi) presented at same conference in Bangalore, India. Both countries had proceeded independently to this point. Limited technical exchanges occur thereafter. Following their research from 1973 to 1974, PHRI develops the forerunner of the Cement Deep Mixing (CDM) method using fluid cement grout and employing it for the first time in large-scale projects in soft marine soils offshore. (Originally similar methods include DCM, CMC (still in use from 1974), closely followed by DCCM, DECOM, DEMIC, etc., over the next five years). In addition, First commercial use of Lime Column method in Sweden for support of excavation, embankment stabilization, and shallow foundations near Stockholm (by Linden Alimak AB, as contractor and SGI as consultant/researcher) in 1975.

Public Works Institute Ministry of Construction, Japan, in conjunction with Japanese Construction Machine Research Institute began research on the Dry Jet Mixing (DJM) method using dry powdered cement (or less commonly, quick-lime) in 1976. It was also the same year that Soil Mixed Wall (SMW) method used commercially for first time in Japan by Seiko Kogyo Co.

In 1977, Cement Deep Mixing (CDM) method had been marked development. CMD method Association established in Japan to coordinate technological development via a collaboration of industrial and research institutes and the first practical use of CMD (marine and land uses). First design handbook on lime columns (Broms and Boman) published by Swedish Geotechnical Institute. China commences research into CDM, with first field application in Shanghai using its own land-based equipment in 1978.

The first commercial using in Japan of Dry Jet Mixing was marked in 1980, and then it quickly superseded Deep Lime Mixing (DLM) with land-use only. In addition, DJM Association established in Japan. After that, in 1983, Eggestad publishes state-of the-art report in Helsinki dealing with new stabilizing agents for Lime Column method.

In 1984, SWING method developed in Japan, followed by various related jet assisted (W-R-J) methods in 1986, 1988, and 1991. The Tenox Company reported more than 1000 projects completed with SCC method in Japan (1989), prior to major growth thereafter (9000 projects to end of 1997, with a $100 to 200 million/year revenue in Japan and elsewhere in Southeast Asia). And then, in 1990, Dr. Terashi, involved in development of DLM, CDM, and DJM since 1970 at Port and Harbor Research Institute, Japan, gives November lectures in

Finland. Introduces more than 30 binders commercially available in Japan, some of which contain slag and gypsum as well as cement. Possibly leads to development of "secret reagents" in Nordic Countries thereafter.

Low Displacement Jet Column Method (LDis) developed in Japan in 1991. In the same year, Bulgarian Academy of Sciences reports results of local soil-cement research and Geotechnical Department of City of Helsinki, Finland, and contractor YIT introduce block stabilization of very soft clays to depths of 5 m using a variety of different binders.

In early 1990s, first marine application of CDM at Tiajin Port, China: designed by Japanese consultants (OCDI) and constructed by Japanese contractor with his own equipment (Takenaka Doboku).

In 1991, Chinese Government (First Navigational Engineering Bureau of Ministry of Communications) builds first offshore CDM equipment "fleet", using Japanese technology used for first time (1993) at Yantai Port. (Reportedly the first wholly Chinese Design-Build DMM project.). And Jet and Churning System Management (JACSMAN) developed by Fudo Company and Chemical Grout Company in Japan.

DJM Association Research Institute publishes updated Design and Construction Manuals (in Japanese) in 1993. In the same year, CDM Association claims 23.6 million m^3 of soil treated since 1977. And SMW claims 4000 projects completed worldwide since 1976, comprising 12.5 million m^2 (7 million m3). According to report in Japan, from 1977 to 1995, more than 26 million m^3 of CDM treatment reported and about 15 million m^3 of DJM treatment.

In 1997, SMW method used for massive ground treatment project at Fort Point Channel, Boston, MA (largest DMM project to date in North America), and other adjacent projects. Input at design stage to U.S. consultants by Dr. Terashi (Japan).

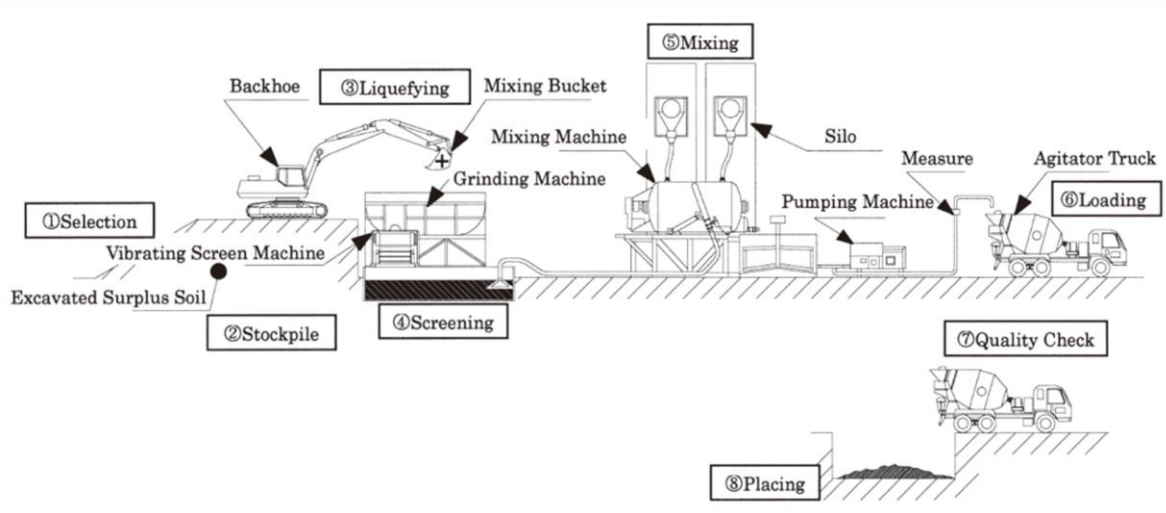

Figure 2-3 Flow of Liquefied soil stabilized method

From 1998 to around the year 2000, a variety of numerical modeling work has been performed on the interaction of soil cement columns in soft clays, for example Kerin and Karstunen (2009), Chai et al. (2010) and Abushara et al. (2009. There studies have focused on settlement reduction from “T” shaped columns, “cross” shaped columns and “multi columns” supported embankment loading.

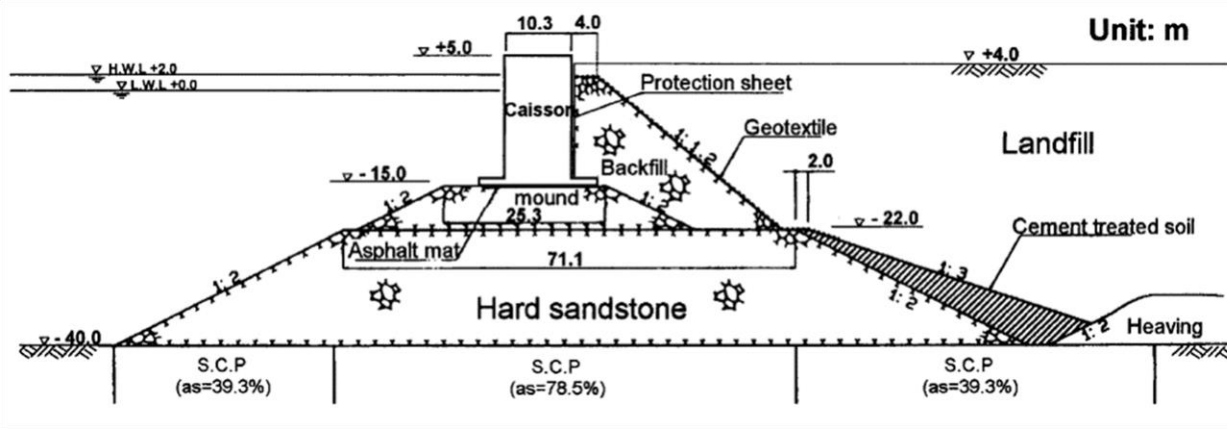

Figure 2-4 Cement treated soil using as slope protection Tang et al. (2001)

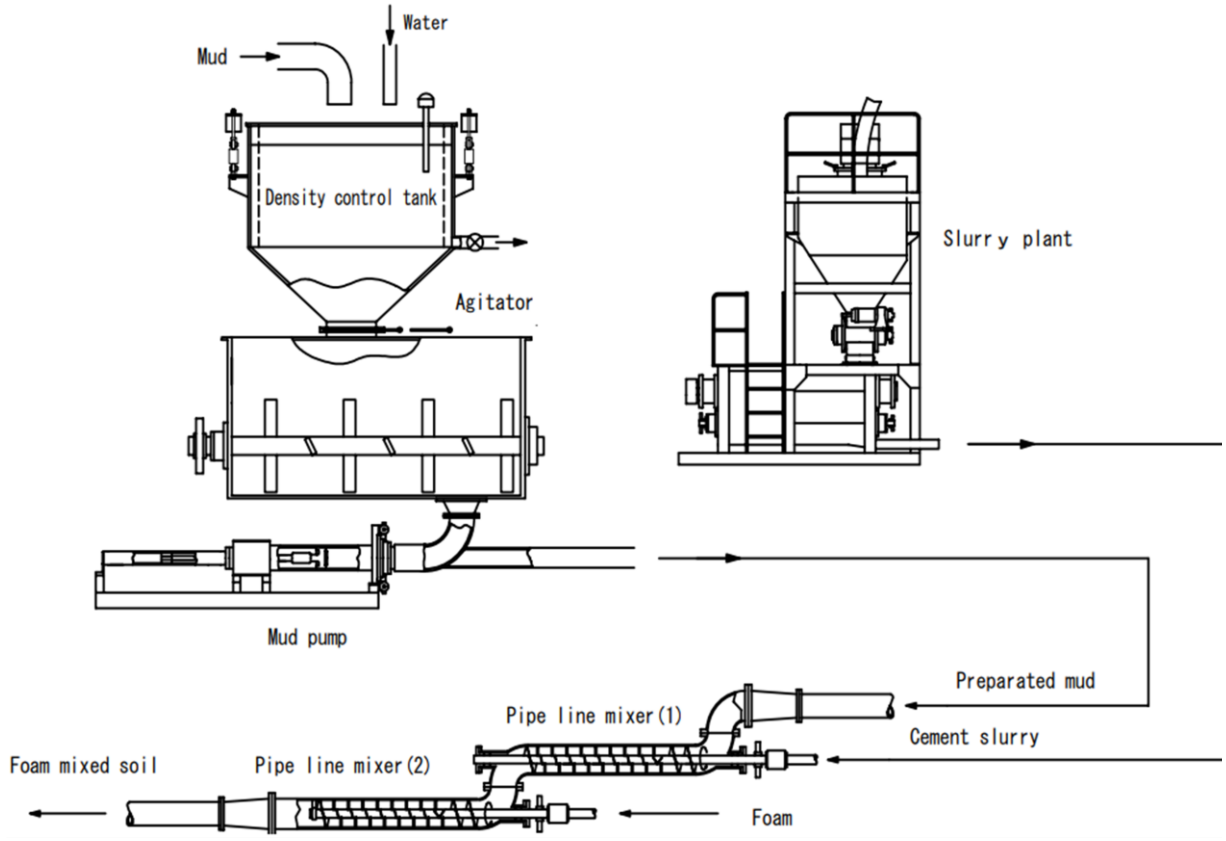

Figure 2-5 Production system for foam mixed lightweight soil

2.4. Applications of the LSS

In 1997, Kuno et al. presented one of several applications of LSS method: filling a cavity under pavement of urban road (Figure 2.8). The cavity is inferred mainly in the way that the submerged backfilled sand in the ground is washed out little by little to a nearby open space, for example sewage pipes, and thus, a cavity is created and grown.

This application is thought to be possible of decreasing time and cost comparing to a conventional method. Thus, two kinds of filed performance tests were conducted in order to verify capability and applicability of the method and acquire necessary field data for future maintenance works. The first field performance test used an on-site plant and a stabilized soil of low strength and relatively high flow condition while the second test use

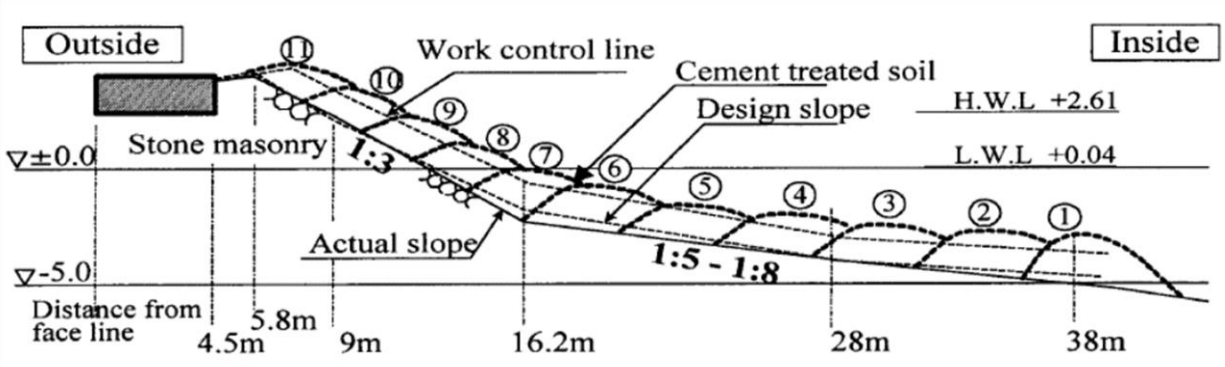

Figure 2-6 Placement of cement treated soil along slope Tang et al. (2001)

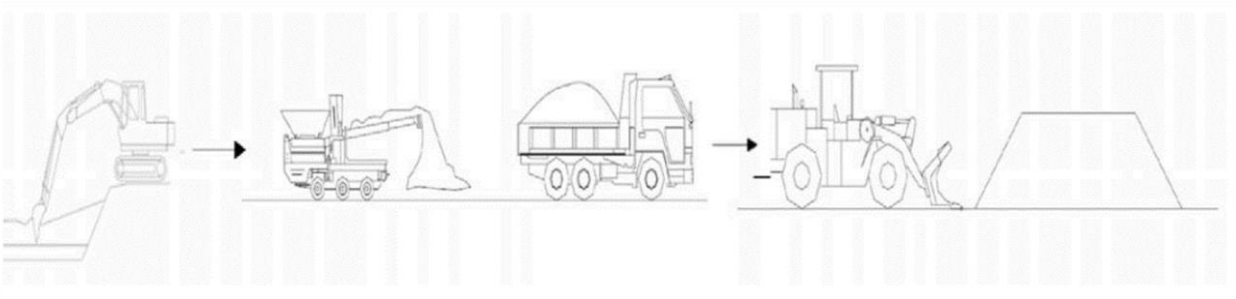

Figure 2-7 Two stages construction method using lightly lime/cement treated clayey soils Hino et al. (2008)

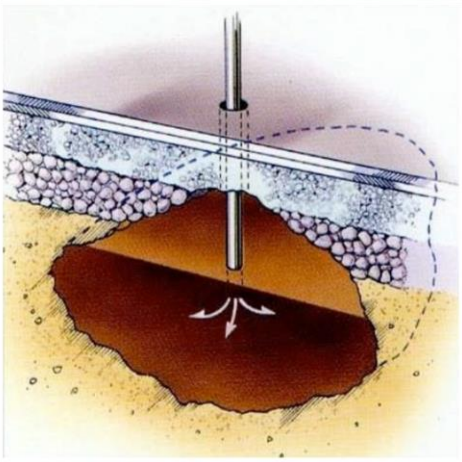

Figure 2-8 Use of LSS for filling cavity under road surface

remote plant and stabilized soils of high strength and low flow condition. The tests were evaluated in term of adequate mix proportion, working system, working time, filling outcome, occupation of road, result of quality control test, and so on. Through two sequential field performance tests, it is confirmed that the method possesses good capability of filling cavities under the pavement and make it possible to decrease time and cost.

Murata (2011) reported that LSS consists of slurry made of on-site soil, water, cement and sand of clay as appropriate LSS is used for backfill at upper part of a cut and cover tunnel and as an invert material of a shield tunnel (Figure 2.9). Pit sand is usually used for backfilling, but LSS is much better than the sand, because it is easy to use with on-site soil and LSS can be buried without compaction into a narrow space.

The lower part of shield tunnel is usually buried by low-strength concrete (unconfined compressive strength: about 10 MN/m^2). From the environmental point of view, however, LSS, which can reuse on-site soil, is now often use. Mixture of LSS was designed from the results of unconfined compressive tests and repeated loading tests. Then, it was designed the unconfined compressive strength of liquefied soil should be 6 MN/m^2 for safety purpose. To hold this strength level for some on-site soil, a very large amount of cement is needed (300 ~ 400 kg/m^3 of LSS). So, a method to mix wasted fiber materials into LSS has been studied in order to increase the

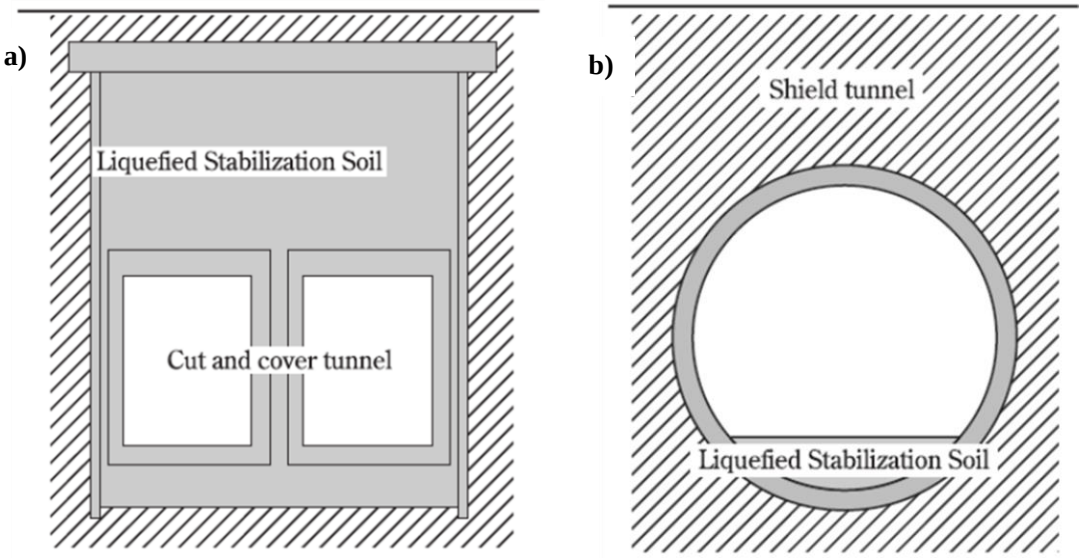

Figure 2-9 a) LSS used for backfill at upper part of cut and cover tunnel; b) LSS used for invert material of shield tunnel

strength and ductility and decrease the total material cost. Studied have been promoted on what types of wasted fiber material are available and what rigidity level of wasted fiber material is needed.

The design of strength and quality control method of LSS used as building foundation is proposed by Onishi et al. (2005). The results of the research pointed out that it is feasible for LSS to apply for the building foundation in future perspective. Another application of LSS is for constructing fences or retaining walls. Yoshihiro et al. (2006) reported that concrete block construction, which is common for these structures, tens to collapse under strong earthquakes, thus causing a threat to traffic, whereas liquefied stabilized soil block construction is capable of avoiding such damage due to the greater toughness of the material. Also, soil blocks are advantageous over concrete blocks in term of appearance. In their research, they have examined the effects of adding PVA fiber to LSS blocks under atmospheric condition. Tests were carried out on the drying shrinkage properties, resistance to atmospheric exposure, and uniaxial compressive strength. It found that PVA fiber reduces the drying

shrinkage, crack propagation, and compressive strength of LSS block. The following Figure 2-9 is more examples of using LSS for various backfilling works in Japan.

Recently, most underground pipelines have been backfilled by LSS. Figure 2-10 shows a construction site of the pipelines using LSS. Kawabata et al. (2008) conducted full scale field test for buried pipe using steel pipe of 3500 mm-diameter and 26 mm-thickness. Five cases of backfilling methods were applied. From the test results, it was found that the behavior of buried pipe was strongly influenced by the stiffness of backfilling method. In particular, the pipe which is backfilled with LSS showed stable behavior. Moreover, Kashiwaghi et al. (2009) and Kawabata et al. (2010) have proposed a method for thrust restraint using LSS. Mode l pit experiments using a model pipe having a diameter of 260 mm were carried out in order to examine the effectiveness of the LSS for the thrust restraint of buried bend. LSS was applied to the passive area of the model pipe and dry silica sand was used as backfill material. The model pipe was laterally loaded at a speed of 1 mm/min after backfilling to simulate the thrust force.

The lateral resistance and horizontal displacement of the model pipe were both measured. The earth pressure distributions of the passive ground were observed. The results showed that the lateral resistance of the bend in using LSS was increased. It is verified that LSS is an effective backfill material for thrust restraint. Also, other experimental research results showed that the bending stiffness in case using LSS with geosynthetics was increased Kawabata et al. (2009). In addition, the passive resistance was considerably increased in case using LSS with geogrid Kawabata et al. (2008).

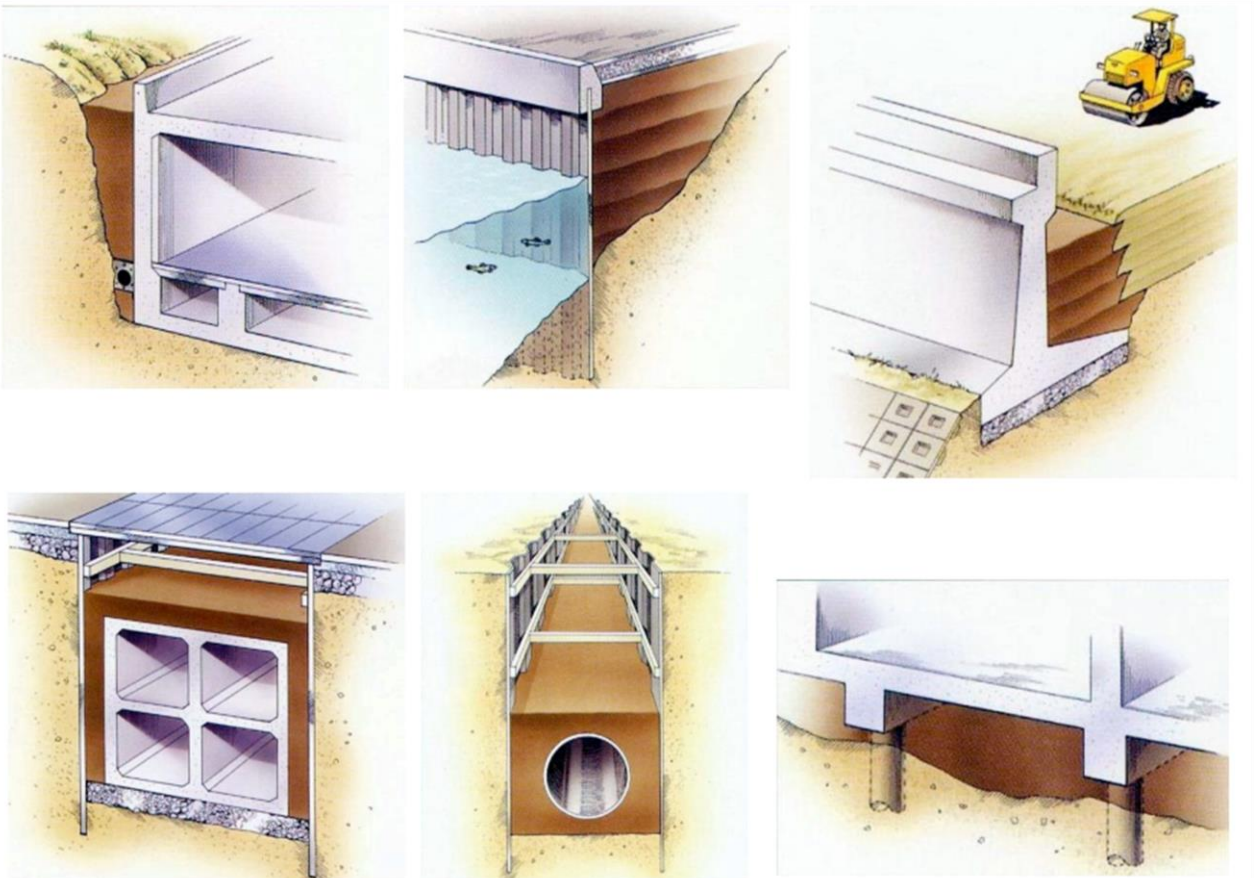

Figure 2-10 Using LSS for various backfilling works in Japan

In 2002, Kohata has proposed a reinforcement method for LSS by mixing crushed newspaper as a fibered material into LSS and carried out a series of unconfined compression tests and triaxial tests. The results indicated that by reinforcement effect, brittle property of LSS mixed with fibered material after the peak was improved.

2.5. Current Research of The Liquefied Stabilized Soil

Liquefied Stabilized Soil materials can be divided into two types: traditional solidified materials and new solidified materials. Initially, the research object of traditional solidified materials was limited to cement and quicklime.

Yuji Maeno (1996) considered that the slag passed the compaction test, unconfined compression test, CBR value test, consolidation compression test under the conditions of different, single solidified materials (such as cement, quick lime) and their dosage. He Comparatively systematically analyzed and studied the reasons that influenced the unconfined compressive strength, optimal water content, CBR value, and change trend of the treated soil, which provided a basis for future research and engineering practice.

Researchers have developed different slag solidification materials for different soil qualities, such as Medina reinforced red clay with phosphoric acid. Tomohisa (1997) believes that the use of fine recycled powder, pulp slag, fly ash, and volcanic ash soil for high moisture content and high organic matter content Slag soil. Bobrowski (1997) developed an ionic curing agent to strengthen soft foundation soil. Zalihe (1998) used fly ash and lime to solidify expansive calcareous clay.

When scholars study the slag solidifying agent, the research objects and ideas are broader, including not only the research on the various additives of cement and lime, and the recycling of waste, but also the in-depth study of fungus reinforcement and insect reinforcement technology.

Shirazi (1998) believes that the mixture of lime and fly ash can avoid cracking caused by the shrinkage of cement soil. Bell (1999) added PFA (an additive) to cement and lime to strengthen the effect of clay reinforcement Research. Miller (2000) studied the performance of cement pit dust (CKD) reinforcement treatment of slag. Kohata (2001) had considered a method of adding crushed old newspapers as a fibrous material to add Liquefied Stabilized Soil Reinforcement methods. Robert (2001) studied a highly concentrated liquid slag solidification material (CLS). Saboundjian (2002) reported on the application of an organic slag solidification material (EMC2) in roadbed reinforcement. Attom (2002) It has been reported that burned olive waste can be used as a new material for the solidification of dregs. Thecan (2003) studied basidiomycetes in the decomposition of lignin by saprophytic organisms. He believed that it has an essential role in the solidification of dregs Function. Nene (2004) studied the method of natural termites using clay to solidify and build nests and proposed the concept of geotechnical entomology.

Now muck-solidified materials have been widely used in water conservancy projects, high-speed railways, highways, airport runways, the benefits are very obvious. It was named as one of the great inventions of the 20th century by the United States "engineering news." In Japan, it was also called the new materials of the 21st century.

In many countries, slag solidified specialized companies produce materials as a branded product, such as Parma curing enzymes, Soilrock, EN-1 slag solid materials produced in the United States. Roadbond Roadpacker was developed in Australia. Moreover, the UKC company in Japan Produced various brands of slag solidification materials.

Mechanism of solidified soil

The research on the solidification mechanism of treated soil is mainly carried out from theory and experiment, and its research methods are various. In the experiments, chemical analysis, scanning electron microscope (SEM), differential thermal analysis, or X-diffraction (XIM) methods are generally used to study the solidified matter generated in the solidified soil. The mechanism is to perform ion adsorption and exchange of the curing agent and the components of the slag. It is to reduce the surface electricity of the slag micelle and the thickness of the electric double layer of the slag micelle. It can make the slag particles tend to agglomerate. The chemical reaction generates new substances to strengthen the links between the muck particles. The volume expansion of the product improves and fills the pores between the muck particles. The distance between the muck particles is shortened under the action of external squeezing force, and the muck structure is compact, making the solidified soil easy to compact Become one, to obtain excellent macro mechanical properties.

Supabj Nontananalldhn (1996) used X-rays to irradiate the treated soil, studied the reasons that affected the strength change of the reinforced soil at different ages, and observed the changes in the microstructure and morphology of the reinforced soil through an electron microscope. From a micro perspective, they are more scientific and reasonable.

Linda Hills and Vagn C. Johansen (1996) proposed the formation model of the structure of solidified soil according to the actual solidification process of solidified soil. The structure of solidified soil is composed of the solidification agent hydrates fully surrounding the soil particles and filling the pores between the soil particles.

Experiments and theoretical calculations with cement-solidified soil show that the amount of cementing agent corresponding to the cemented soil particles and the pore filling is quite consistent. The model reflects the relationship between the structure of the compacted soil filled with the cement-filled pores and the strength growth of the solidified soil.

Masashi Kaman (1996) studied the role of liquid curing agent in cement-based composite consolidated soil. He determined that the consolidation of cement-based composite consolidated soil is the interaction of curing agent, cement, and clay, which promote each other to form dense, stable, Higher strength structure. The chemical bonding of the hydration of the curing agent and the cementation of the cementing material can form the early strength of the solidified soil. In contrast, the performance of the solidified soil of the slag curing agent continues to improve for a long time. It depends on the interaction of the composite slag cement and the slag.

Mechanical properties of solidified soil

At present, the commonly used curing agents are cement and quicklime, which are evenly distributed in the sludge by manual or mechanical stirring. Therefore, the mechanical properties of the solidified soil of the sludge are similar to the cement soil. Many scholars have used the method of the indoor geotechnical experiment to study the characteristics and influencing factors of reinforced soil more systematically.

MA Khan, A. Usmani, SS Shah, and H. Abbas et al. (1996) conducted indoor geotechnical tests on solidified soil and found that the unconfined compressive strength increases with the increase of cement content. The dry density increases with the cement content Under the same conditions, the compressive strength of the mixed curing agent is increased by a maximum of 10 to 138 % compared with the non-mixed, and the dry density is increased by 0.01 to 0.07 g / cm^3. Good anti-seepage performance. Permeability coefficient can reach the order of 10-8 cm / s. The slow freezing method was used to conduct the anti-freeze test. After 50 freeze-thaw cycles,

the strength loss was 13.5-21.07 %. For the slag soil, the curing effect is remarkable; first, the curing agent and the soil are mixed and placed, and then the cement or lime is added to obtain a better curing effect. First, after mixing the curing agent with the soil for a while, the optimal moisture content of the soil will decrease, and the soil will feel wet and viscous, and the cohesion of the soil will increase. At this time, adding cement or lime can obtain a higher degree of compaction and dry density.

Kohata (2000) conducted a series of unconfined and triaxial compression tests after it was discovered that crushed old newspapers were incorporated as a fibrous material. The results show that the peak value of the brittle characteristic curve of the slag is higher than that of the ordinary curing agent after the fiber material is mixed by this method.

CHAPTER 3
OVERVIEW OF UNDRAINED BEHAVIOR OF COHESIVE SOIL SUBJECTED TO CYCLIC LOADING

3. Overview of Undrained Behavior of Cohesive Soil Subjected to Cyclic Loadings

3.1. Introduction

Strength decrease may occur in saturated soil subjected to cyclic loading of waves, wind, etc. The amplitude of the cyclic load on the foundation soil can be only dozens or hundreds of kilopascals, which does not lead to destabilization or a large displacement of the foundation. There are many situations in which the duration of the series of loading cycles is such that little or no drainage of the pore water can take place during the period of the repeated loading, which will make the pore pressure increase and, as a result, the bearing capacity of the foundation can become significantly lower. It is, therefore, useful to study the effects of repeated loading under undrained conditions in the laboratory.

The undrained cyclic loading condition in the soil is prevalent during earthquakes. Depending on several geological factors and the earthquake magnitude, such loading can be expressed in terms of the magnitude, frequency content, loading duration, etc. Similarly, the response of the soil depends on its properties and can vary from site to site. Detailed laboratory and experimental studies have been presented in the literature by various researchers to understand the cyclic behavior of different types of soil during an earthquake loading (e.g., Sangrey et al. (1969); Andersen et al. (1988); Ansal & Erken (1989); Zergoun & Vaid (1994); Boulanger & Idriss (2004). Typically, rapid cyclic loading in undrained soil continuously increases the porewater pressure and simultaneously decreases the effective stress of soil. The shear deformation increases with the number of loading cycles and may trigger liquefaction in the soil. Zergoun and Vaid (1994) pointed out that the cyclic stress magnitude above a certain threshold value progressively generates pore water pressure and simultaneously reduces the effective stress. This conclusion was drawn while conducting undrained cyclic triaxial tests on normally consolidated Cloverdale clay. Also, they observed that during cyclic loading, the stress path migrates towards the origin, and the clay fails when it touches its monotonic failure effective stress path (Figure 3-1). Furthermore, a significant reduction in the shear modulus and consciously enlarged stress-strain hysteresis loop was also observed with increasing cycles. The undrained cyclic behavior of soil depends upon many factors, and some crucial factors are discussed below.

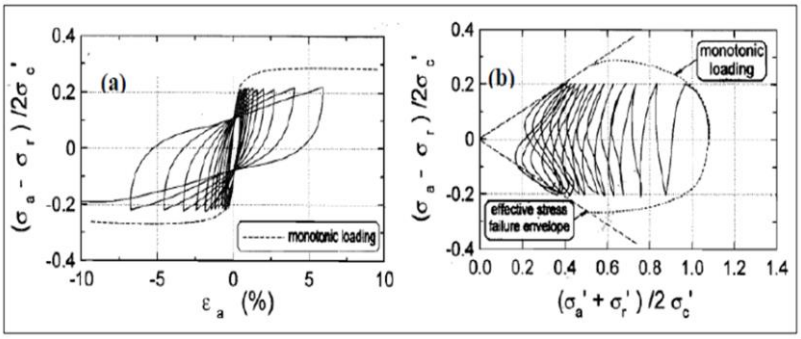

(After Zergoun and Vaid 1994)

Figure 3-1 Stress-Strain and Effective stress path plots of undrained cyclic test of saturated clay

3.2. Stress State In-situ and Laboratory

Soil elements can be subject to different stress conditions depending on in-situ or laboratory circumstances. The state of shear and normal stresses acting on a soil element, prior to and during cycling, controls the cyclic behavior. The elemental stress state depends on the static stress history experienced by the soil and the cyclic loading path induced by an earthquake or other sources in the in-situ or laboratory.

3.2.1. In-situ static stress states

Two different in-situ stress conditions can be distinguished: the conditions under free-field flat ground and under slopes or structures. Figure 3-2 shows the stresses acting on a typical element in both situations. In Figure 3.1a, the soil is expected to have experienced anisotropic consolidation under k_0 path. Being level at the surface and not subjected to any surcharge, the ground does not impose any static shear stress on the horizontal planes ($\tau_{vh,stc} = 0$) which are considered most critical within such an element during an earthquake Seed (1968). $\sigma_{v,stc}$ and $\sigma_{h,stc}$ are the static normal stresses in vertical and horizontal directions, respectively, and act as the principal stresses, σ_1 and σ_3, before induction of the shear stresses ($\sigma_{hs} = k_0\sigma_{vs}$).

In the case shown in Figure 3-2 b), the soil elements undergo anisotropic consolidation and the horizontal planes are subjected to static driving shear stresses ($\tau_{vh,stc} \neq 0$) resulting from a sloping surface or the weight of a structure. At zones far enough away from an existing structure, the surcharge may bring an element to extension by causing a higher horizontal normal stress than the vertical Yang & Pan (2017). The initial static shear stress is also referred to as sustained shear stress.

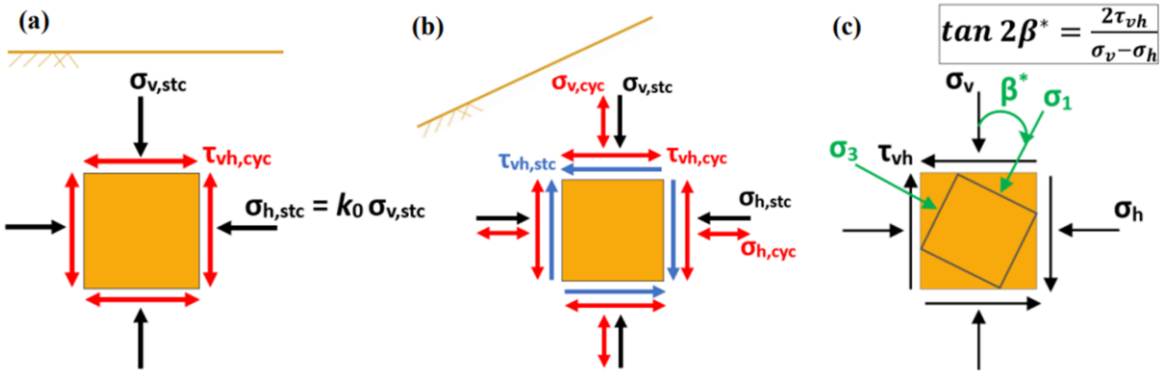

Figure 3-2 Static and seismic-induced cyclic stress components acting on a soil element under; a) Free-field flat ground, b) Slopes or structures, c) General condition

3.2.2. In-situ cyclic stress paths

Cyclic stresses acting on structures can originate from earthquake, traffic loads, wind, and waves. During an earthquake, body waves propagate vertically and consist of shear and longitudinal waves. Two types of stresses are then exerted on the soil element: cyclic horizontal shear stresses, $\tau_{vh,cyc}$, from the shear waves and cyclic normal stresses, $\sigma_{v,cyc}$ and $\sigma_{h,cyc}$, from the longitudinal waves, as illustrated in Figure 3-2 a) and b). The cyclic stress path is usually plotted in a shear stress space (Figure 3-3) with one axis being assigned to the $\tau_{vh,cyc}$ and the other to the maximum inclined shear stress within the element generated by the cyclic normal deviator stress, $(\sigma_{v,cyc} - \sigma_{h,cyc})/2$. It has been shown that in one-dimensional stability analysis of level ground, the cyclic normal

stresses are negligible Ishihara (1996). In this situation, $\tau_{vh,cyc}$ is the main component of cyclic stress acting on the element (Figure 3-3 a) and Figure 3-3 b). However, if two-dimensional deformation is the case (like in Figure 3-3 b), both components of cyclic stress, i.e. horizontal shear and normal deviator, will be considerable and their combination will create a coupled stress path according to Figure 3-3 c). It should be emphasized here that under seismic excitation, $\tau_{vh,cyc}$ is applied in multiple directions in the horizontal plane Pyke et al. (1975); Ishihara & Yamazaki (1980).

Cyclic stress paths originating from sea waves and traffic loads are also displayed in Figure 3-3 d) and e), respectively. These are often called rotational paths and incorporate a continuous smooth rotation of principal stresses, signified by change in β* angle. β* is defined in Figure 3-2 c) showing the stress components acting on a soil element in general conditions. Note that also in some linear paths, β* will be subject to a limited smooth rotation if the initial deviator stress, $\sigma_{v,stc} - \sigma_{h,stc}$, and/or initial horizontal static shear stress, $\tau_{vh,stc}$, are non-zero.

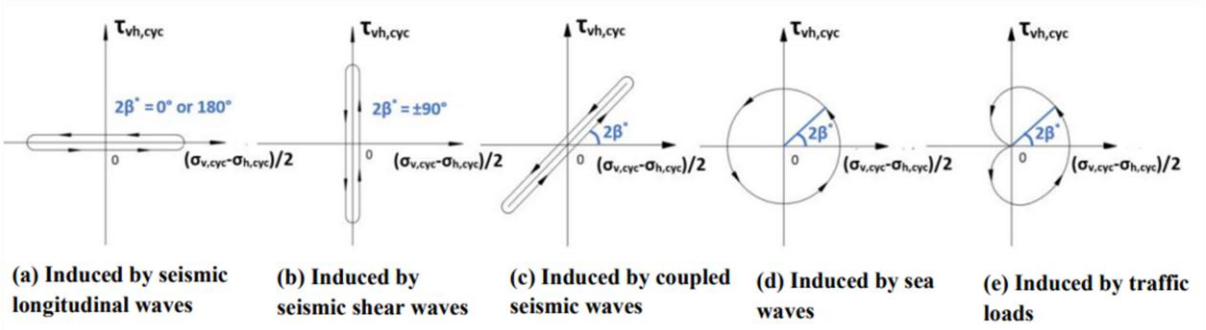

Figure 3-3 Cyclic stress paths encountered in different phenomena after Ishihara (1996); a) Imitable in triaxial shear, b) Imitable in direct simple shear and torsional shear, c-e) Imitable in combined axial-torsional shear

3.2.3. Laboratory simulations

Attempts have been made for several decades to imitate the in-situ stress conditions in the laboratory. Current approaches and how they are related to, and deviate from, the field conditions are briefly explained hereunder. The results from these test paths will be discussed throughout the chapter.

Isotropic triaxial shear

The most conventional approach to simulating cyclic behavior is to carry out an isotropic consolidation ($\sigma_v = \sigma_h$) followed by uniform cycles of loading in a triaxial apparatus. As shown in Figure 3-4 a), equal σ_v and σ_h at the consolidation stage apply only a normal stress without any shear stress component to any plane within the element including the critical one (inclined at 45°). The succeeding inclined cyclic shear stress, τ_{cyc}, induced by periodic increase and decrease of vertical deviator stress, will oscillate symmetrically around zero (Figure 3-5 a). This has been considered as an approximation of the stress state on horizontal planes in free-field level ground (Figure 3-2a) after the pioneering work of Seed & Lee (1966). Nonetheless, this simulation requires an isotropic consolidation which differs from that experienced in the field, which is constrained to follow one dimensional loading and unloading and, as a result, the principal stress ratio ($k = \sigma_3/\sigma_1$) can be far from unity.

Anisotropic triaxial shear

Anisotropic triaxial consolidation ($\sigma_v \neq \sigma_h$) produces a different elemental stress state by generating static shear stresses on inclined planes, τ_{cyc}, as illustrated in Figure 3-4 b). It is also possible to effect extension by applying a horizontal stress greater than the vertical. A nonsymmetrical cyclic loading is then applicable in both

compression and extension which can be reversal (two-way), one-way non-reversal, or one-way intermediate (Figure 3-5 b-d). Thus, anisotropic triaxial tests provide a fair simulation of the conditions under slopes and structures (Figure 3-2 b) in terms of both the consolidation path, i.e. the principal stress ratio, and the stresses acting on the critical plane. This approach was first suggested by Lee & Seed (1967a) and has been widely used in laboratory studies.

Triaxial testing comes with a number of limitations that prevent it from accurately reproducing the behavior

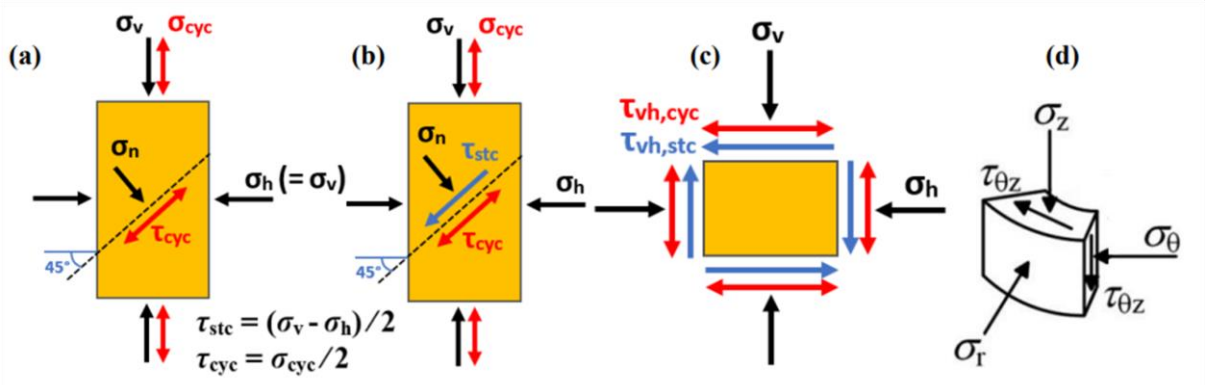

Figure 3-4 Elemental stress state; a) Isotropic triaxial shear, b) Anisotropic triaxial shear, c) Direct simple shear, d) Torsional shear

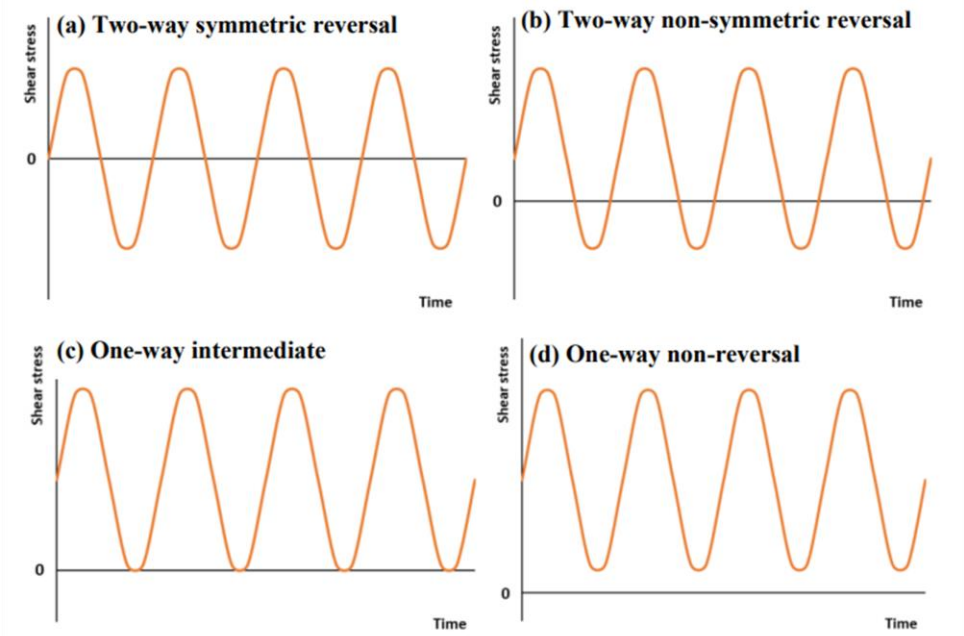

Figure 3-5 Different shape of cyclic loading

in the ground. For example, it is unable to mimic the free-field level ground with principal stress ratios other than unity. Triaxial shear also diverges from reality by applying to the sample cycles of vertical deviator stress, which represent seismic longitudinal body waves, rather than horizontal shear, representing the shear body waves which are perceived to be more crucial (Figure 3-3 a) as opposed to Figure 3-3 b) and c). Another discrepancy is that the direction of principal stresses on a triaxial sample is fixed or can only have a jump re-orientation of 90° when deviator stress passes through zero. Furthermore, the axial-symmetry of triaxial samples does not correspond with many practical cases in which plane strain situations are more common.

3.3. Qualitative Cyclic Behavior

Several concepts are often used to qualitatively describe the behavior of soil under cyclic loading, particularly when considering relatively large numbers of cycles. These concepts are illustrated in Figure 3-6 and based on the definitions given by Rascol (2009):

+ Adaptation: The cyclic stress-strain hysteresis loop converges to a new elastic state, so further cycling involves no energy dissipation. This state is never reached practically in soils, as a small amount of energy dissipation always occurs during cyclic loading.
+ Accommodation: The cyclic stress-strain hysteresis loop evolves and accumulates permanent strains before eventually stabilizing and forming a closed hysteresis loop. Energy continues dissipating with each cycle; however, no further plastic strains are accumulated.
+ Ratcheting: Plastic strain continuously accumulates with each new load cycle. Soil failure is eventually reached if loading continues.
+ Cyclic softening: the secant stiffness of the soil decreases with the number of cycles.
+ Cyclic hardening: the secant stiffness of the soil increases with the number of cycles.

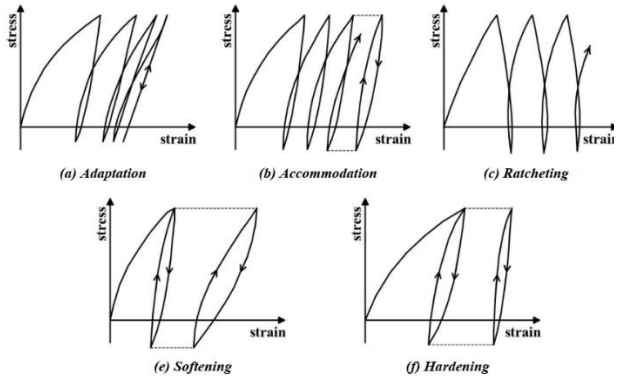

Figure 3-6 Summary of qualitative descriptions of soil behavior under cyclic loading Rascol (2009)

3.4. Failure Criteria under Cyclic Stress Conditions

The problem of defining failure in a cyclic loading test has not been specifically solved, and the proposed definitions have not been universally accepted. Some early publications are vague about the failure criteria used, while others use several criteria. On some occasions, when pore pressures have been measured, the critical factor appears to be whether or not the repeated loads lead to a pore pressure buildup which brings the soil to the effective stress failure envelope. If the stress level is below a certain amplitude of cyclic stress magnitude, this value of cyclic stress amplitude has been called the threshold stress; nonfailure equilibrium is reached and closed stress-strain hysteresis loops are measured. The final soil behavior is essentially elastic. On the contrary, if above the threshold value, the effective stress failure envelope is reached Sangrey et al. (1969). For sand soils, pore pressures are usually measured, enabling an effective stress failure criterion to be defined, such as zero effective transient stress Seed & Lee (1966). However, clay behavior under undrained cyclic loading is more complex than sand behavior because of its dependency on such factors as time-dependent creep and pre-consolidation periods which can be overlooked for the cyclic behavior of sand. Therefore, to avoid difficulties in defining failure in terms of effective stress, failure criteria for cyclic tests have been defined in terms of a cyclic strain amplitude for both sands and clays. Various criteria have been used in different studies ranging from about

±2.5 % single amplitude cyclic strain to 20 % double amplitude cyclic strain in the cyclic stress-controlled laboratory test.

Nielsen et al. (2012) suggest that failure modes may be separated into two main groups when analyzing cyclic tests. Tests in which permanent, or residual shear strains, γ_p, dominate, were subjected to one-way loading and failed by incremental collapse. While the other group of tests, subjected to two-way loading, were dominated by cyclic strains, γ_{cyc}, and failed due to liquefaction. Nielsen et al. (2012) defined failure as either the point at which γ_p = 15 % or γ_{cyc} = 15 %. This is similar to the failure criterion adopted by the Norwegian Geotechnical Institute (NGI), which defines failure as the point where either the average strain, γ_{Av}, or γ_{cyc} reaches 15 % (Andersen, 2015).

For symmetrical cyclic loading tests, the variation of the cyclic shear strain with the number of cycles is the main aspect to study. Each curve with a certain value of the cyclic shear strain as a function of the number of cycles is shown in Figure 3-7. The failure envelope indicates that, at a given number of cycles, the sample would fail if the value of the stress level q_{cyc}/q_{max} is above the failure envelope. Otherwise, the sample will not fail. Thus, this diagram can also be used to estimate the equilibrium state.

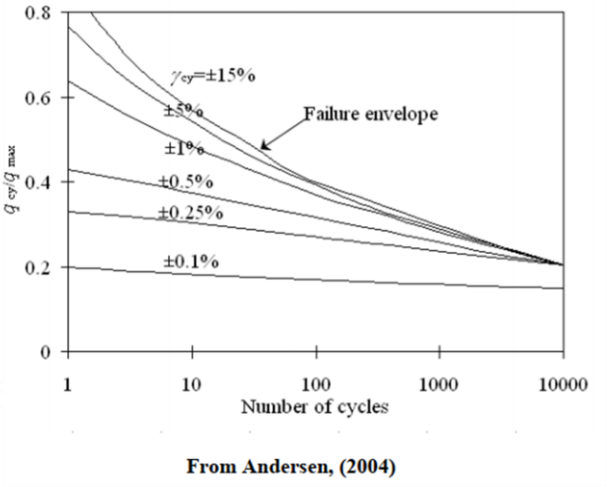

Figure 3-7 cyclic shear strain as a function of the number of cycles

3.5. Effect of Cyclic Test Variables

3.5.1. Effect of Confining Pressure

It has been observed that soils subjected to high confining pressure tend to contract and generate higher pore water pressure Vaid and Chern (1985); Vaid and Thomas (1994). Therefore, increasing the confining stress reduces the cyclic resistance of soils. Mitchell and King (1976) conducted undrained cyclic loading tests on Champlain sea clay at different confining stresses. They observed that the pore water pressure increased with effective confining stress and that the number of cycles required to cause failure reduced with the increasing confining stress. During the 1999 Kocaeli earthquake, Turkey, Bray, and Sancio (2006) witnessed a severe reduction in soil strength at locations near buildings compared to open sites. They also conducted undrained cyclic triaxial tests on undisturbed samples from Adapazari, Turkey, at different confining stress levels (Figure 3-8). These studies concluded that soils at high effective confining pressure are less resistant to cyclic shear failure (liquefaction).

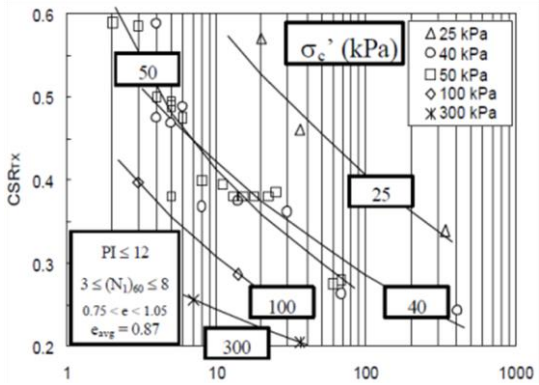

Figure 3-8 Influence of effective confining stress on cyclic failure after Bray and Sancio (2006)

3.5.2. Effect of Loading Condition

Excess pore pressure and inelastic strain exhibit manifest more quickly under two-way (reversal) cyclic loading than under one-way (non-reversal) loading, in terms of loading conditions. The cyclic strength under two-way loading is rather lower than for one-way loading, as seen in Figures 3-9. Furthermore, in the condition of two-way loading, the level of stiffness degradation is higher.

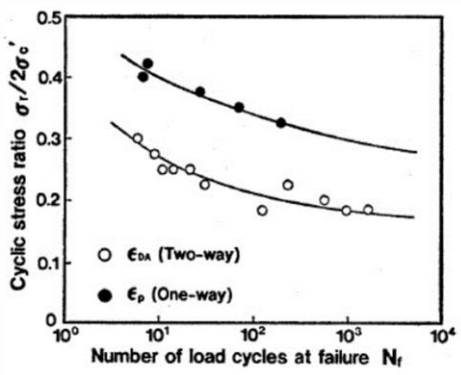

Figure 3-9 Cyclic response under different loading conditions and consolidation states, Effect of loading type.

The influence of the amplitude of the initial deviator stress on the cyclic response has received considerable. The increased the initial deviator stress (i.e., the greater the initial level of anisotropy), the fewer cycles required to achieve failure, and the higher the cyclic strength (Figure 3-9). Because the reversal condition disappears in

certain conditions for high levels of initial deviator stress, the rate of stiffness degradation in anisotropically consolidated soils is lower than in isotropically consolidated soils. In the latter situation, any cyclic deviator stress magnitude will result in reversed loading, increasing the rate of stiffness degradation.

Hyodo et al. (1993) conducted cyclic triaxial experiments on anisotropically consolidated soil under various initial deviator stress values to determine the effect of initial deviator stress (q_0). As seen in Figures 3-10, the cyclic shear strength diminishes as the initial static deviator stress increases. Hyodo et al. investigated the behavior of Itsukaichi clay and Toyoura sand during cyclic loading and observed that the clay is more unstable when subjected to initial static shear stress than the sand.

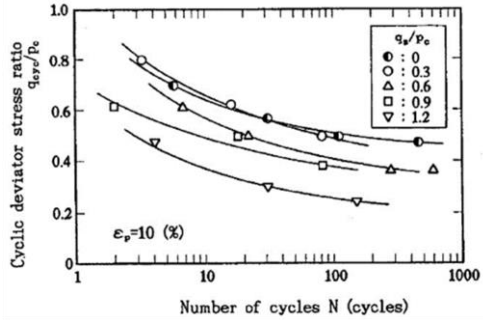

Figure 3-10 Cyclic response under different loading conditions and consolidation states: Effect of magnitude of initial deviator stress

Finally, as shown in Figures 3-11, isotropically consolidated samples tend to develop higher excess pore pressures than consolidated anisotropically.

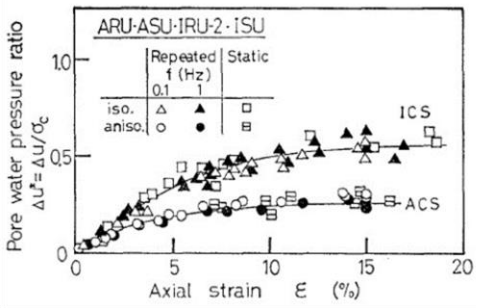

Figure 3-11 Cyclic response under different loading conditions and consolidation states: Effect of initial consolidation state

3.5.3. Effect of Loading Frequency

In general, the influences of loading frequency tend to be mitigated as the cycle number and the amplitude of the cyclic deviator stress decrease. But if a few cycles are accounted for, the frequency seems to have a substantial impact. Cohesive soils show increased cyclic shear strength under high-frequency loading than under low-frequency loading. In general, for a given number of cycles, lower frequencies cause higher shear strain and excess pore pressures.

Ansal and Erken observed that the frequency effect in normally consolidated clay diminishes with an increasing number of cycles and with decreasing shear stress amplitude. Similarly, Zhou and Gong (2001) evaluated the effect of loading frequency on normally consolidated and overconsolidated samples. Matsui et al. found that the level of stiffness degradation is high for low loading frequencies; for higher frequencies, the level of degradation will be lower. When the loading frequency is less than 0.1 Hz, the sample will quickly degrade even for a few cycles (Figure 3-12).

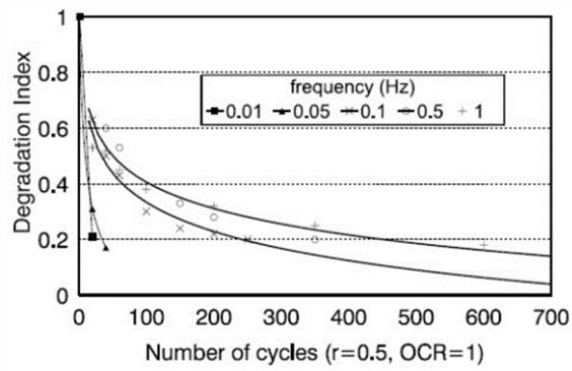

Figure 3-12 Effect of frequency on the degradation index

3.6. Dynamic Properties of Soil

Analyzing the response of soil to dynamic loadings, such as earthquakes, is a very challenging and important task for successful geotechnical design. Soil often amplifies the bedrock excitation to the ground surface; therefore, most of the damage during earthquakes is induced by the dynamic response of soil deposits. In this regard, a reliable ground response analysis is critical to evaluate the liquefaction potential of soil and the stability of other structures on the surface. The equivalent linear model is the simplest and most widely used model to estimate the ground response of soils Kramer (1996). Accurate soil properties are required for the successful modeling of soil.

A typical soil (free from structural loads) when experiencing a uniform cyclic loading is expected to show a hysteresis loop as shown in Figure 3-13a). The characteristics of this loop can be described using two parameters, i.e., the inclination and the breadth of the loop. The inclination of the loop is related to the stiffness of the soil. The average stiffness of soil (secant shear modulus, G_{sec}) for a loop can be estimated by finding the slope of the line connecting two extreme points of the loop

$$G_{sec} = \frac{\tau_c}{\gamma_c}$$

Here G_{sec} represents the general inclination of the loop, τ_c and γ_c are cyclic shear stress and cyclic shear strain amplitude respectively.

The breadth of the loop is associated with its area which can be related to the dissipated energy. It is commonly represented by the viscous damping ratio ξ through the following equation (Jacobsen, 1930; Kramer, 1996).

$$\zeta = \frac{W_D}{4\pi W_s} = \frac{A_{loop}}{2\pi G_{sec}\gamma_c^2}$$

Where W_D is the dissipated energy, W_S is the maximum strain energy, and A loop is the area of the hysteresis loop.

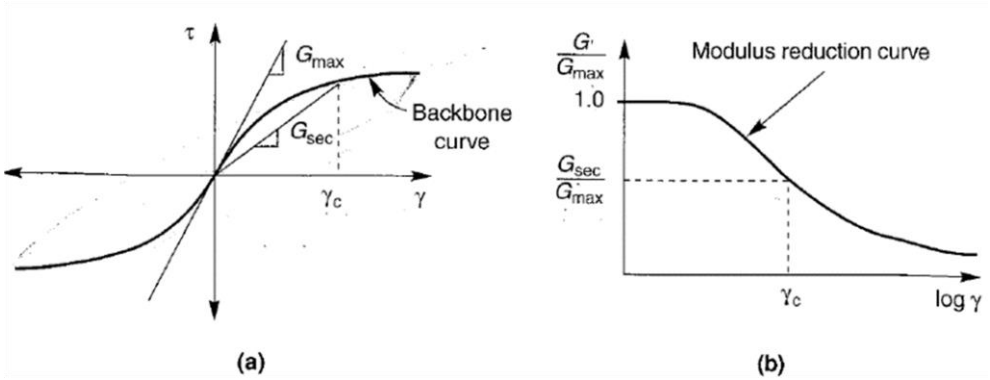

Figure 3-13 Backbone curve and typical modulus reduction curve of soil after Kramer (1996)

The secant shear modulus (G_{sec}) and the damping ratio (ξ) are two important input parameters when modeling soil using the equivalent linear model. Even though the equivalent linear model is approximation of the actual nonlinear behavior of soil, using reasonable measurements of G_{sec} and ξ give reliable results for ground response analysis with efficient computational models. These parameters can be estimated by using laboratory tests with reasonable accuracy. The resonant column test and the bender element test is preferred to measure $Gsec$ and ξ at lower strain levels, while the cyclic triaxial test, simple shear test, and cyclic torsional shear test are recommended for larger strain amplitudes (Kim and Novak (1981); Vucetic and Dobry (1988, 1991); Woods (1994)).

The modulus reduction and damping curves have been given separately for sands and clays in the literature. Seed and Idriss (1970) proposed Gs_{ec}/G_{max} and ξ curves for sands with three different boundaries (Figures 3-14). Sets of modulus reduction and damping curves for cohesive soils were proposed by Vucetic and Dobry (1991) based on the soil plasticity index (Figure 3-15).

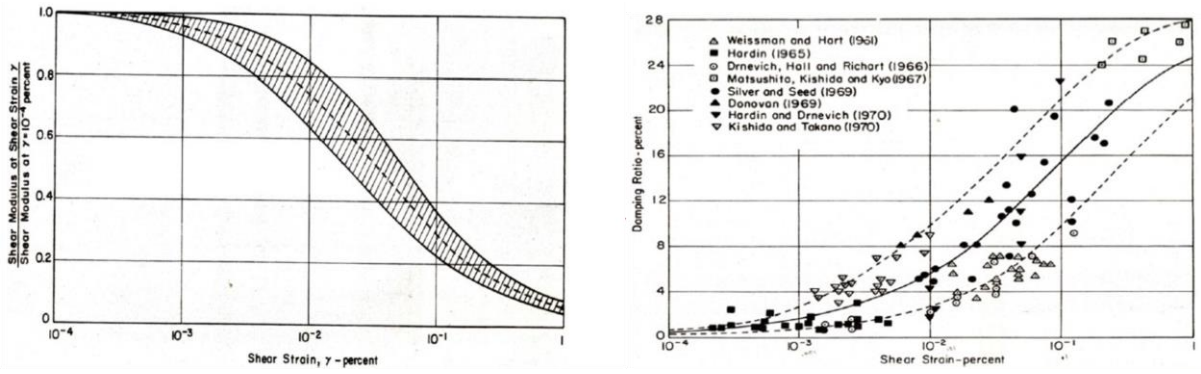

Figure 3-14 Modulus reduction and damping ratio curve of sand (after Seed and Idriss, 1970)

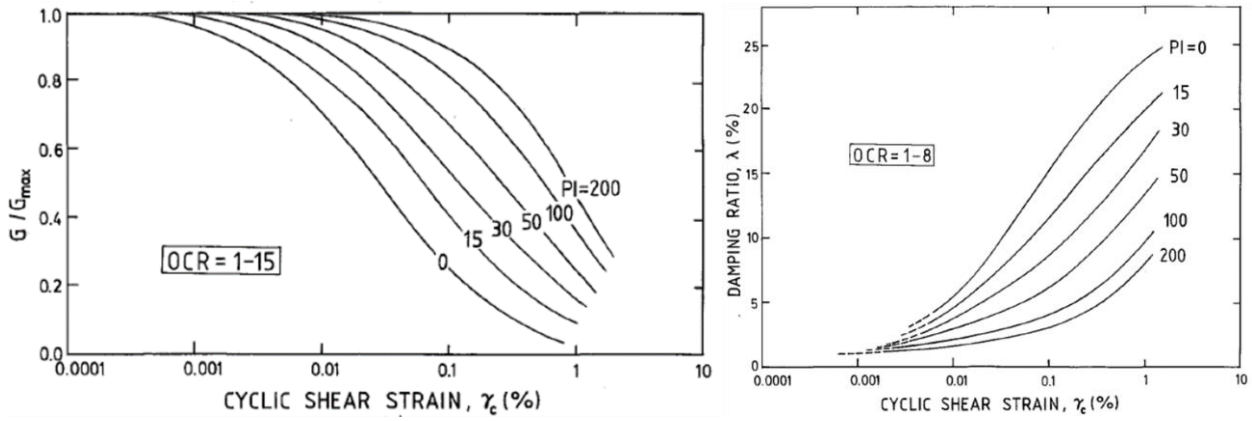

Figure 3-15 Modulus reduction and damping ratio curve of clay after Seed and Idriss (1970)

3.7. Summary

The dynamic response of cohesive soils has been rather widely studied using different experimental techniques.

The response of cohesive soils subjected to cyclic loading is known to be affected by different factors. The most important of these factors are the soil type, the stress or consolidation history, and the specific test conditions.

Two-way or reversed loading, consisting of positive (compression) and negative (extension) stresses, is applied to the sample. Two-way loading is typically applied more quickly than and tends to disturb a sample more than one-way loading

There is a critical cyclic stress or strain that is sometimes referred to as the "cyclic threshold". This threshold clearly delineates two district types of response. For cyclic stresses/strains amplitudes below the threshold, a sample reaches an equilibrium state. If, on the other hand, the cyclic stress/strain amplitude exceeds the threshold, a sample will accumulate inelastic strains, will generate excess pore pressure, and may fail.

In anisotropically normally consolidated samples, excess pore pressures increase with cyclic loading. The effective stress state thus moves toward a failure state. The higher the cyclic deviator stress, the fewer the number of cycles required to reach failure.

Cyclic strength decreases at higher levels of initial drained shear stress.

Soil degradation is strongly dependent on the cyclic strain level applied to a sample.

Low frequencies lead to the lowest cyclic strength and more degradation effects than higher frequencies.

Cyclic stress reversal or two-way cyclic loading has a more damaging effect on clay behavior than non-reversal (one-way) cyclic loading.

CHAPTER 4
EXPERIMENTAL STUDY

4. Experimental Study

4.1. Introduction

A detailed experimental study was carried out to achieve the objectives mentioned in chapter one. Monotonic, cyclic, and multi-stage cyclic tests were conducted on unreinforced and reinforced LSS samples using the Muroran Institute of Technology Triaxial device. This chapter is first to describe the test material, the sample preparation technique, and test methodologies. Secondly, the testing apparatus (including ancillary equipment) and instrumentation used in this study, together with details of the adopted calibration factor and undrained test procedures, are described. Finally, the modification and development of the current computer-controlled cyclic triaxial test to enhance its performance are presented.

4.2. Materials and Preparation Method of Specimen

4.2.1. Test Material

In this study, the New Snow Fine Clay (NSF-Clay), which is a commercially cohesive soil, was used as the homogenous base material. The physical property of NFS-Clay is shown in Table 4-1. The Geoset 200 provided by Taiheiyo Cement Co., Ltd. was used as the cement-based solidification material. Newspapers were used as a fibrous material, which was cut out to a suitable size with the office shredder. A cut newspaper was crushed with water by using a food processor. After drying it in a drying oven, untied it by hand, and it was pulverized again into smaller pieces like cotton wool. In other words, most contents of the fiber are composed of cellulose.

Table 4-1 Physical parameters of NSF-Clay

Physical parameters	Values
Particle density ρ_s (g/cm^3)	2.762
Liquid limit W_L (%)	60.15
Plastic limit W_P (%)	35.69
Plasticity index I_P	24.46
$M (=q_f/p'_f)$ [3]	1.20

4.2.2. Mixing Method

There are two types of mixing methods for LSS, that is, the “slurry method” and the “adjusted slurry method”. In this study, LSS was prepared by the “slurry method” because it is easier for preparation, in which NSF-Clay is mixed with an appropriate amount of water to produce a density-controlled slurry, which is then mixed with solidification material and fiber material. Pulverized newspaper and LSS slurry shown in Figure 4-1.

a) b)

Figure 4-1 a) Pulverized newspaper, b) LSS slurry

Based on the results of the flow test, breathing test, and unconfined compression test after 28 days of curing, an available range of slurry density was drawn with the flow value and unconfined compressive strength, as shown in Figure 4-2. This range was carried out using a cement content of 100 kg/m3 and the unconfined compressive strength after 28 days of curing, as shown in the figure. With an available range of unconfined compressive strength of 200 ~ 500 kPa and a flow value of 160 ~ 300 mm, the basic slurry density in this study was chosen to be 1.280 g/cm^3, and a changing rate of slurry density $D_{\rho f}$ was defined as (Actual slurry density)/ (Basic slurry density) × 100.

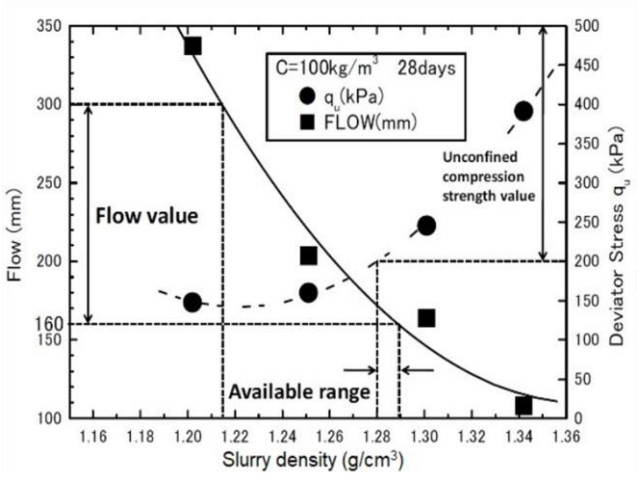

Figure 4-2 Available range of slurry density

4.2.3. Specimen Preparation

In order to investigate the effect of various slurry densities on the strength and deformation of LSS reinforced fiber material subjected to monotonic and cyclic loading, the basic slurry density was decided to be 1.280 g/cm^3, that is based on the standard mix proportion design figure, Kohata et al. (2011), and the slurry density changing

rate $D_{\rho f}$ (actual slurry density) / (basic slurry density) x 100 % was defined as, $D_{\rho f}$ = 100 % (ρ_f = 1.280 g/cm^3), $D_{\rho f}$ = 105 % (ρ_f = 1.344 g/cm^3) and $D_{\rho f}$ = 95 % (ρ_f = 1.216 g/cm^3), respectively. To achieve the desired slurry density, the density test was performed by measuring the mass of slurry poured into stainless steel container (AE mortar container) of 400 cm^3 in volume and the excess portion was cut off with a glass plate. After adjusting the slurry several times to obtain the required density, solidification material in the amount of 100 kg/m^3 was added to the slurry. The amount of fiber material added was referred to as being 10 kg/m^3 based on a previous study (1.963 g/specimen). After adding the fiber material, LSS was mixed with a handy type mixer. Before filling the mold, the laboratory-cured specimens were deaired by the negative pressure of about -90 kPa for 30 minutes and put in a 50 x 100 mm commercial plastic mold with fabric tape on top for extra filling. After filling the container with treated soil, a plastic film was attached to the top edge. The excess portion of fill was trimmed off after 3 hours of curing. The top surface was flattened, re-covered with a polymer film, covered with a wet towel, and cured in moist air at 20±3 °C.

For the in-situ cured specimens, they were poured into isolated pits excavated in the campus grounds and allowed to cure for the prescribed days (42, 56, 80, and 126 days). Figure 4-3 illustrates a schematic diagram of the pits. After placement, the surface of LSS was covered with a polymer sheet and cured in-situ. Using a trimmer and straight edge, the LSS blocks were excavated and formed into cylindrical specimens in the laboratory.

For the cyclic triaxial tests, the specimens prepared at a laboratory with changing slurry density, fiber material, the amount of solidification material, and curing time at 28 days.

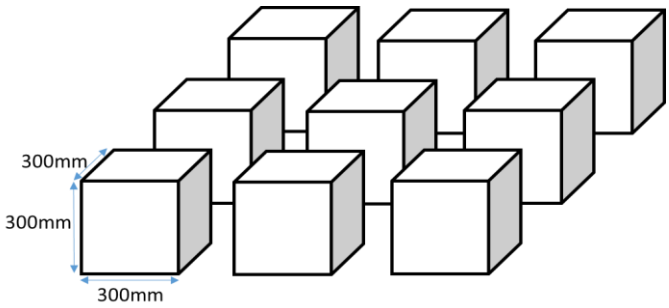

Figure 4-3 Schematic diagram of pits

Figure 4-4 The specimens prepared in-situ

4.2.4. Detailed Preparation Steps

(1) Put the bucket on the scale, weigh the bucket, write down the value, and then return to zero. Then enter the value into the calculation form. (Figure 4-5)

a) b)

Figure 4-5 a) Bucket, b) Electronic scale

(2) Input water into the bucket, weigh it, and write down the value. Then enter the value into the calculation form.

(3) According to the calculation form, adding clay into the water. When adding clay, do not put them on the wall of the bucket.

(4) After fully mixing with the hand mixer, put the slurry into a metal container to check its density. If there is too much difference from the target value, add clay or water again to adjust the density until it reached the target value of density. (Figure 4-6 a))

(5) After the density of the slurry reached the target value, using the calculation form shows the amount of cement that needs to be added. Then add cement and mix them fully with the hand mixer.

(6) After adding the cement, put the mixture into a sealed container for degassing. (Figure 4-6 b))

(7) Open the main switch of negative pressure, link to the container, and open the valves. (Figure 4-6 c))

(8) Turn the negative pressure to -98 kPa and set the time to one hour.

(9) After one hour of degassing, reduce the pressure, close the valve, and weigh the bucket (the bucket must be washed at this moment and weighed).

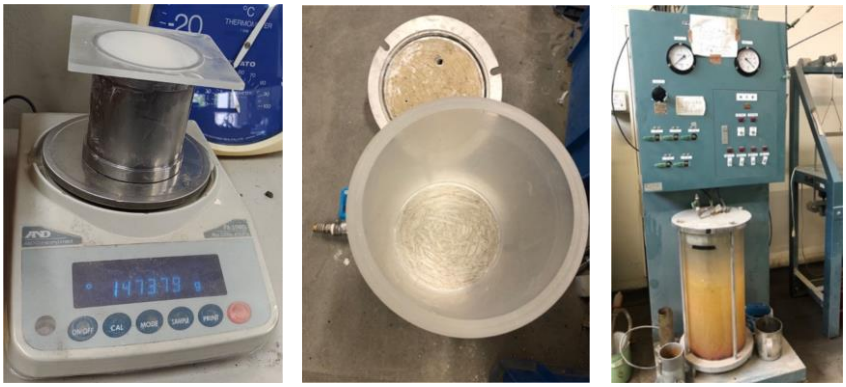

a) b) c)

Figure 4-6 a) Metal container, b) Deair container c) Negative pressure generator

a) b)

Figure 4-7 a) Plastic mold, b) Curing sample

(10) If the fiber material is added, the degassed sample material is then measured for density and weighed again.

(11) Pour the measured sample material back into the bucket and weigh them together.

(12) Enter the calculation form to get the fiber material to be added.

(13) After the addition, mix fully with the hand mixer.

(14) Prepare the small sample boxes in advance and fill the sample materials separately. When filling half the bottles, shake them slightly to shake out the air bubbles in the bottles. Continue adding to the full bottle. (Figure 4-7 a))

(15) Cover the sample bottle with plastic wrap and tie it with rubber bands.

(16) At last, put the sample into a box with constant temperature and humidity for the prescribed days of curing. (Figure 4-7 b))

4.3. Triaxial Apparatus

The triaxial device has been the most widely used apparatus in geotechnical engineering for several decades. It is capable of simulating axisymmetric in-situ soils conditions and is the preferred choice of engineers for evaluating soil strength and stiffness parameters owing to its advantages over the other laboratory devices. In

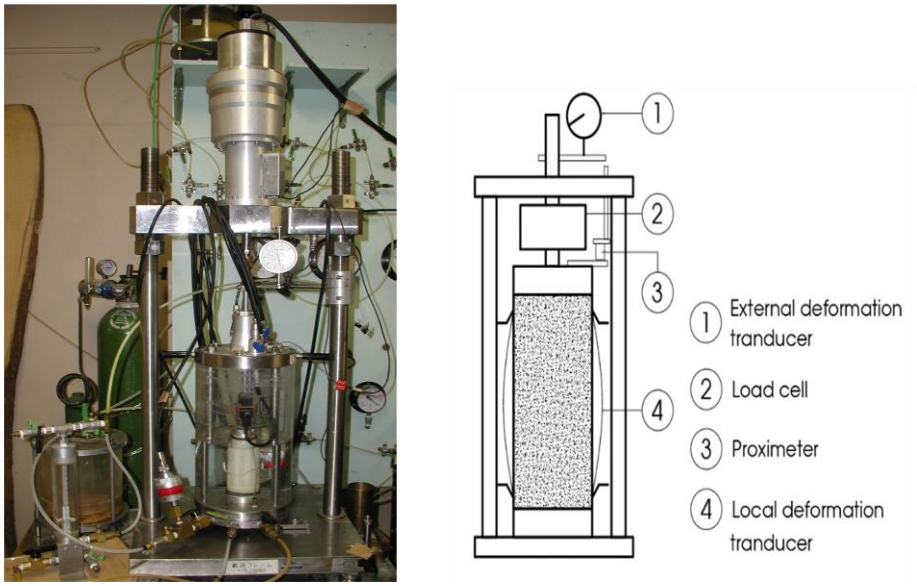

Figure 4-8 Triaxial apparatus and its schematic diagram

this study, monotonic and cyclic undrained tests were conducted on LSS using the Muroran Institute of Technology Triaxial device as shown in Figure 4-8.

The test typically uses a cylindrical specimen of soil with a diameter of 50mm, and a height diameter of 100 mm, this ratio of approximately 2:1 to reduce the end restraint and improve stress-strain uniformity in the sample. (Taylor, 1948; Bishop and Green, 1965; Lade, 1982). The specimen is sealed with a rubber membrane and placed into a cell that can be pressurized. The test commonly includes three main stages known as saturation, consolidation, and shearing. Table 4-2 explains the functions of primary triaxial components. Some primary triaxial components as shown in Figure 4-9.

Table 4-2 Primary components of a typical triaxial system and its function

Component	Function
Top and bottom pedestal	Supporting the specimen at the correct position and providing drainage ports
Rubber membrane and O-rings	Seal the specimen from cell fluid and maintain different pressure (cell pressure and pore pressure)
Porous discs	Allowing drainage through the sample
Back pressure / volume controller	Apply back or pore pressure to the specimen and measure volume changes
Cell pressure	Apply all-around confining pressure to the specimen
Load cell	Measure the change in axial load
Axial displacement transducer	Measure the change in specimen height
Cell and pore Pressure transducers	Measure the change in pressure in cell and pore pressures

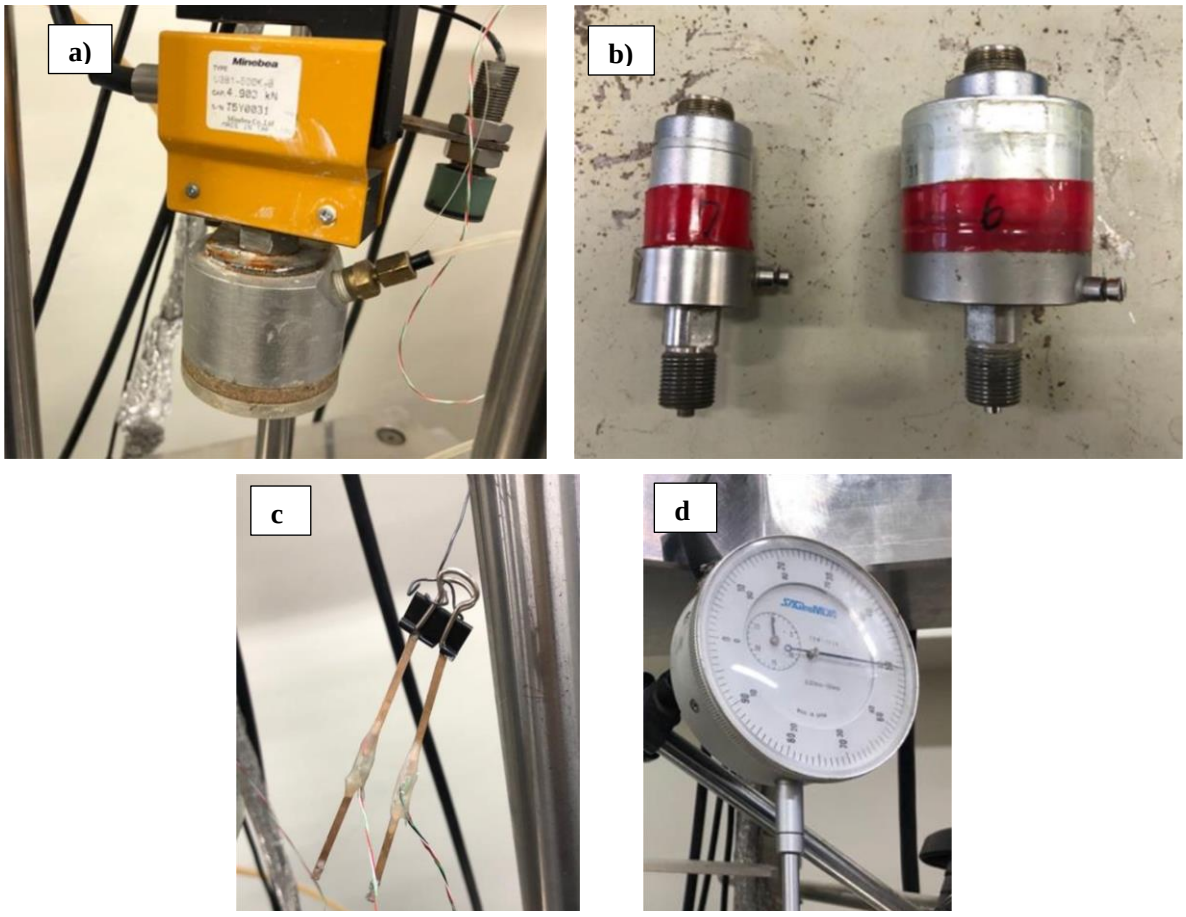

Figure 4-9 a) Load cell, b) Cell pressure and Pore water pressure transducer, c) Local displacement transducer,

4.4. Test Procedure

All the LDTs, Dial gauge, load cells, pressure transducers were calibrated before starting the test programme. Unreinforced and reinforced LSS samples were carefully prepared and tested in the triaxial device.

4.4.1. Calibration Factor

LDTs

1) Make a graph with software (origin, etc) and take displacement [mm] on a vertical axis, and voltage value [mV] on a horizontal axis.
2) Set up the formula of the quadric curve ($y = ax^2 + bx + c$) and a, b, c are the calibration factors.

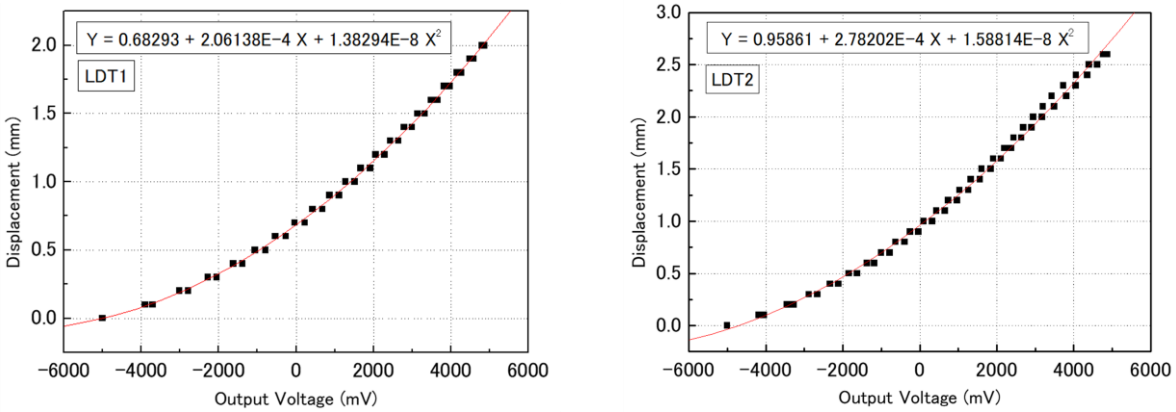

Figure 4-10 Calibration factor of LDTs

Dial gauge

1) Make a graph with software (origin, etc) and take displacement [mm] on a vertical axis, and voltage value [mV] on a horizontal axis.
2) Set up the formula of the straight line ($y = ax + b$), and a, b are the calibration factors as shown in Figure 4-11.

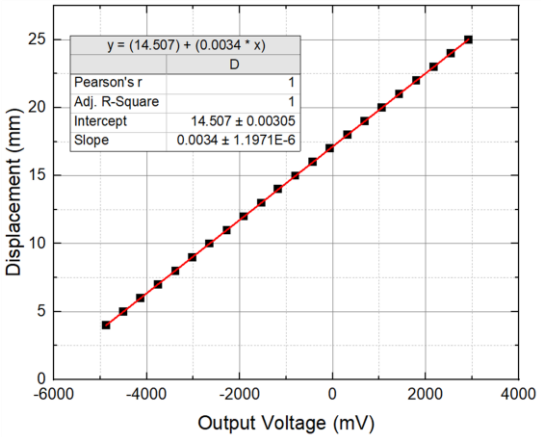

Figure 4-11 Calibration factor of Dial gauge

Load cell

1) Make a graph with software (origin, etc) and take loading [N] on a vertical axis, and voltage value [mV] on a horizontal axis.

2) Set up the formula of the straight line (y = ax + b), and a, b are the calibration factors as shown in Figure 4-12.

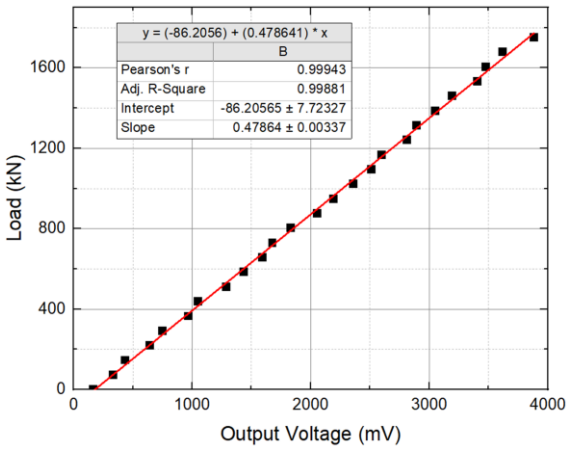

Figure 4-12 Calibration factor of Load cell

Pressure transducers

1) Make a graph with software (origin, etc) and take output voltage [mv] on a vertical axis, and pore water pressure or confining pressure [kPa] on a horizontal axis.
2) Set up the formula of the straight line (y = ax + b), and a, b are the calibration factors as shown in Figure 4-13.

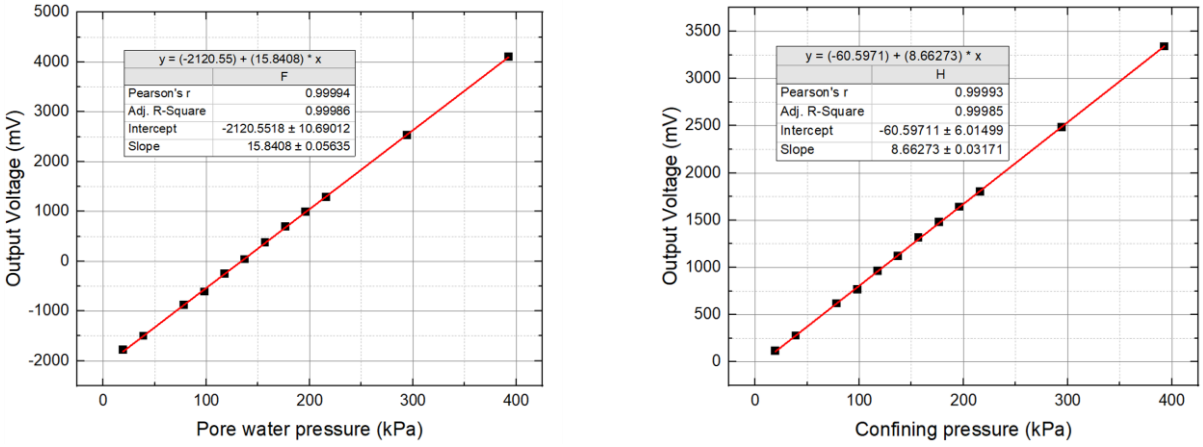

Figure 4-13 Calibration factor of pore water pressure and confining pressure

4.4.2. Prepare of Test Equipment

1. Open positive pressure, negative pressure switch (front door, backroom), and magnet.

2. When the positive pressure is turned on, make sure the gas inside is opened a little bit, the oil is still there, and if there is too much water, pour it out.

Loadcell can only be initialized once when there is no pressure. Figure 4-14）

Turn on the power of the PC, Mega torque motor drive box, and amplifier.

ATT amplifier is from the right 1/50, 1/10, 1/10, 1/10, 1/20, 1/10（Figure 4-15）

Figure 4-14 Driver box of mega torque motor

Figure 4-15 ATT amplifier

1. Start the test recording program (Be careful when opening the program because of the difference in the case with and without the creeping loading test mode).

2. Install in the apparatus the porous stone and pedestal which have been soaked in water.

3. To carry out the water supply until no air is out from the porous stone (flushing), open the water supply valve (black valve) while holding a finger on the installation part of the pore water pressure gauge by mounting the water supply coupler (water supply, red valve).

4. As being sure that the water comes out from the upper drainage route to connect the bifurcation hose that opened the drain valve, ask someone to lift up the degassed water-making machine by opening the degassed water supply valve, and fixing it firmly, such as monkey nuts, and tightening the drain valve.

5. Open the valve without attaching the upper pipe and lower valve of the drainage layer.

6. After fixing by attaching the gum (rubber) and covering the inside of the mold the membrane (divided in half if long), glue to the mold which is removing air (connect green pipe on left).

7. Drop neatly the membrane attached to the hinge (Since deformation and fatigue in the hinges as taking and pulling the membrane at this time, take to thin down the membrane with a cutter).

4.4.3. Saturation and Isotropic Consolidation

In these tests, nearly full saturation could be achieved by applying the double negative pressure method in which the de-aired water flowed through the specimens under high back pressure to the LSS specimen (about 196 kPa). The saturation of the sample for the triaxial test was checked by measuring Skempton's B-value. For a fully saturated specimen at undrained conditions, the change in pore water pressure (Δu) should be equal to the change in the cell pressure ($\Delta\sigma_3$) Skempton (1954). The B-value can then be defined as $B = \Delta u/\Delta\sigma_3$. A minimum value of 0.95 for LSS samples and 0.99 for sand samples were confirmed in all tests.

After confirming a high B-value, the samples were consolidated into predetermined stress states. LSS samples were consolidated for 15 hours. For monotonic tests to study the behavior of LSS under various conditions, the effective confining pressure remains constant at 98 kPa. Three different effective confining pressures of 58.8, 98 kPa, and 196 kPa were applied to research the effect of confining pressure on LSS under cyclic load.

4.4.4. Shearing Phase

All monotonic, cyclic, and multi-stage small strain tests were conducted under undrained conditions. All monotonic tests were conducted at an axial strain rate of 0.054 %/min which ensures pore-water pressure equalization within the sample during shearing, it is also identical to the previous study. To investigate the small strain deformation property, small unloading/reloading loops were applied on the pre-failure region of the stress-strain curve in monotonic tests.

In order to research the effect of cyclic test variables on LSS such as the stress amplitude, the initial stress ratio, and the control (stress vs. strain cycles). The software to control the triaxial apparatus system was modified and improved to enhance its performance. All cyclic tests were conducted at an axial strain rate of 5.04 %/min.

4.5. Modification and Development of the Computer-controlled Cyclic Triaxial Test

A digital servo motor in the triaxial apparatus is used to move the loading platen upwards or downwards and can ignore backlash when reversing the loading direction. Having the loading mechanism by a servo motor gives the ability to precisely control the loading rate of the device. The positive point about the servosystem is that it sends the actual speed to the data acquisition system, which gives the ability and flexibility for the feedback algorithm to perform perfectly under any circumstance. The whole operation of the apparatus during the test was automatically controlled by PC software. However, the fully automated function of controlled software is limited. The absence of cyclic features and the difficulties in performing the cyclic test with the currently existing software is the main reason for this part of study.

This part of the study focuses on modifying and developing an automated computer-controlled cyclic triaxial test. Improving stress-controlled features and adding strain-controlled, multi-stage features were conducted. All important test results, such as strain, stress, pore water pressure, number of cycles, and frequency, are calculated and exported automatically. Especially the stress failure criterion where the strength of the sample reduces and

does not reach the target stress amplitude is recognized automatically. This feature is essential to prevent forced damage of the sample in extension or compression mode when subjected to symmetrically cyclic loading.

The cyclic triaxial control software is programmed using Visual Basic 6.0 language, which is an integrated development environment (IDE) from Microsoft. It is used to program, develop and debug computer software using different programming languages.

Development cyclic loading interface shown in Figure 4-16.

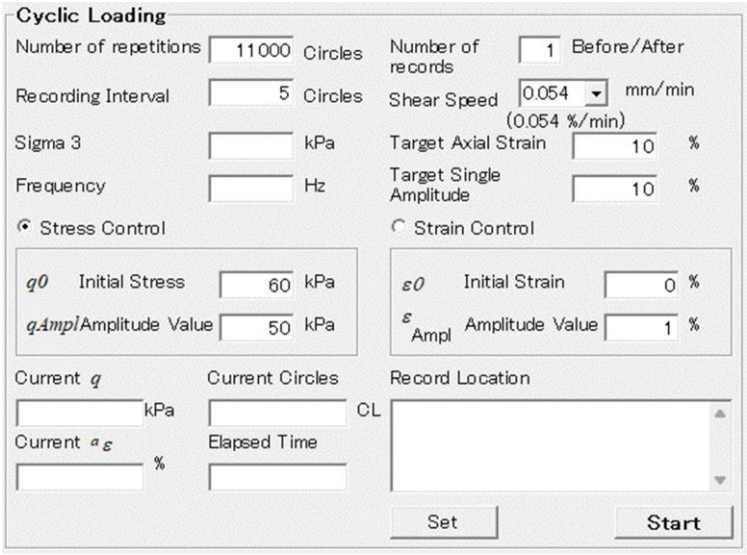

Figure 4-16 Development cyclic loading interface

Calibration factor form to update regularly calibration factor shown in Figure 4-17.

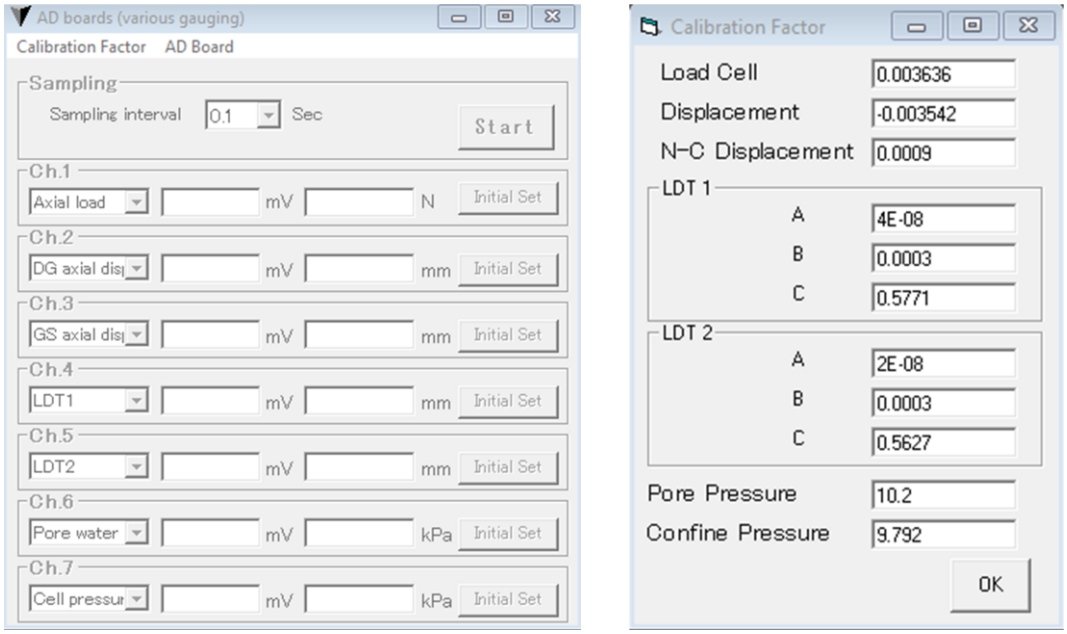

Figure 4-17 Calibration factor form

Software able to calculate and export automatically test result such as total stress (sigma 3, sigma 1), effective stress (sigma' 3, sigma' 1), Maximum and minimum LDT strain, Maximum and minimum Dial Gauge strain, Deviatoric stress q, Mean Effective stress p', Number of cycles, Frequency f (Hz), Maximum and minimum pore water pressure, Excess pore water pressure ratio as shown in Figure 4-18.

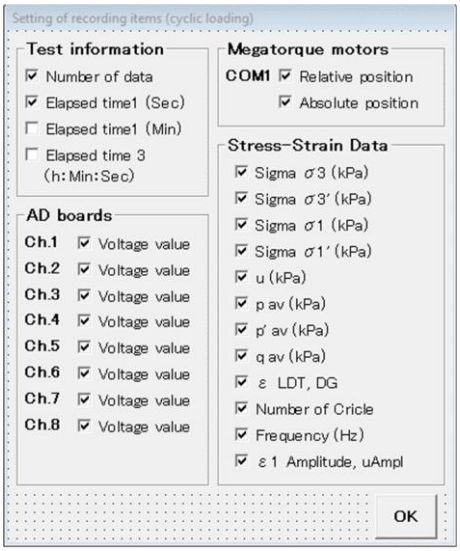

Figure 4-18 Output test result option

Multi-stage stress-controlled quasi-cyclic testing method was added and adopted in this research program to study the modulus and damping behavior of LSS. The deviatoric stresses were chosen to produce a range of cyclic strains in the specimen (targeted between 0.01 % to 2 %). To avoid significant disturbance in the sample, the maximum axial strain was limited to 1% at each stage, and the number of loading cycles at each deviatoric stress level was limited to five cycles. Then the specimen was consolidated to a higher stress level and quasi-cyclic loading was repeated.

Figure 4-19 shown the the test result of developed cyclic triaxial test with symmetrical, nonsymmetrical loading and strain-controlled test.

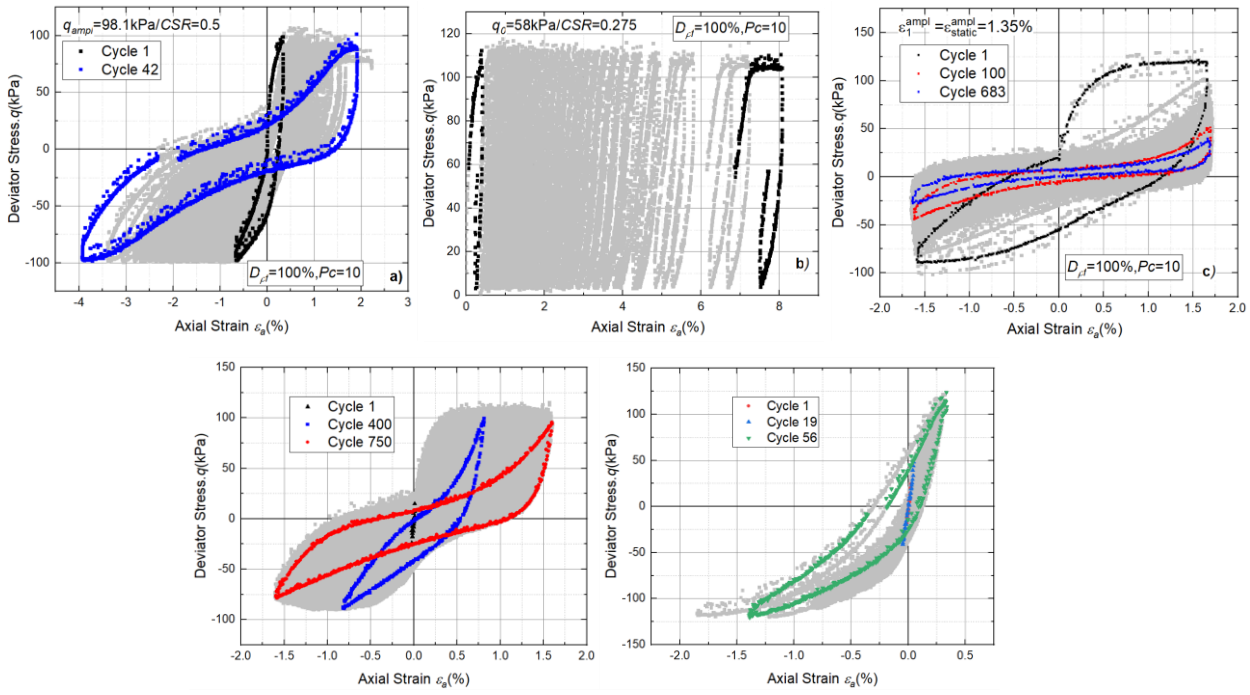

Figure 4-19 The test result of developed cyclic triaxial test with symmetrical, nonsymmetrical loading and strain-controlled test.

CHAPTER 5

TEST RESULTS AND DISCUSSION OF UNDRAINED TRIAXIAL COMPRESSION TESTS ON REIFORCED LIQUEFIED STABILIZED SOIL PREPARED BY VARIOUS CONDITIONS

5. Test results and Discussion of Undrained Triaxial Compression Tests on Reinforced Liquefied Stabilized Soil (LSS) Prepared by Various Conditions

5.1. Introduction

Liquefied Stabilized Soil (LSS), Kuno et al. (1997), is one of a cement-treated soil, which improves the soil properties by the effect of cementation arising in an excavated soil mixed with cement-based solidification material and water, and has been extensively used in Japan. However, there is concern that the increased use of cement-based solidification material in LSS increases their strength and causes them to behave brittlely, reducing their seismic resistance. In order to improve brittle behavior, Kohata, Ito and Koyama in 2011 proposed using pulverized newspaper as a fibered material to reinforce LSS, and conducted a series of unconfined and triaxial compression tests. The study found that after the peak of the stress-strain curve, LSS mixed with a fibrous material had improved brittle behavior.

After that, numerous studies have investigated the strength and deformation properties of LSS with fiber. Nevertheless, no comprehensive investigation of LSS with fiber under various combination conditions has been performed. Especially the effect of various slurry densities and longer curing times on the strength and deformation properties of LSS cured in-situ conditions is not clear. This study aims to investigate the strength and deformation properties of LSS prepared by various conditions. The effect of curing time and slurry density on the strength and deformation properties of LSS cured laboratory and in-situ were discussed based on the undrained triaxial compression test results for 48 cases. The programme of the undrained triaxial compression test is summarized in Table 5-1.

Table 5-1 Programme of undrained triaxial compression test

Test	Case ID	Specimen ID	Curing Time (days)	Slurry Density (g/cm^3)	Fiber Content (kg/ cm^3)	Cement content (kg/cm^3)	Curing condition
1(25)	S-42-1-In (out)	①	42	$D_{\rho f}$ =1.216	*Pc*=0	100	Cured laboratory and In-situ
2(26)	S-56-1-In (out)		56				
3(27)	S-80-1-In (out)		80				
4(28)	S-126-1-In(out)		126				
5(29)	S-42-2-In (out)	②	42		*Pc*=10		
6(30)	S-56-2-In (out)		56				
7(31)	S-80-2-In (out)		80				
8(32)	S-126-2-In(out)		126				
9(33)	S-42-3-In (out)	③	42	$D_{\rho f}$ =1.344	*Pc*= 0		
10(34)	S-56-3-In (out)		56				
11(35)	S-80-3-In (out)		80				
12(36)	S-126-3-In(out)		126				
13(37)	S-42-4-In (out)	④	42		*Pc*=10		
14(38)	S-56-4-In (out)		56				
15(39)	S-80-4-In (out)		80				
16(40)	S-126-4-In (out)		126				
17(41)	S-42-5-In (out)	⑤	42	$D_{\rho f}$ =1.28	*Pc*=0		
18(42)	S-56-5-In (out)		56				
19(43)	S-80-5-In (out)		80				
20(44)	S-126-5-In (out)		126				
21(45)	S-42-6-In (out)	⑥	42		*Pc*=10		
22(46)	S-56-6-In (out)		56				
23(47)	S-80-6-In (out)		80				
24(48)	S-126-6-In (out)		126				

5.2. Stress-strain Relationships

5.2.1. Effect of Slurry Density

In order to investigate the effect of slurry density on the strength and deformation properties of LSS, the relationships between deviator stress q and axial strain ε_a based on a locally measured axial strain by LDTs with various slurry densities at 42 days of laboratory and in-situ curing are shown in Figure 5-1 and Figure 5-2. Figure 5-1 a) and Figure 5-2 a) show the q~ε_a relation up to ε_a =3.5 %. Also, Figure 5-1 b) and Figure 5-2 b) show the small strain level up to 0.01 % for evaluating small strain stiffness.

It is found that the change of slurry density influences significantly the strength of LSS both laboratory and in-situ at 42 days of curing. Figure 5-3 shows the relationship between maximum deviator stress q_{max} and the changing rate of slurry density at 42 days of laboratory and in-situ curing. By defining the average decreasing or increasing of q_{max} as (the value that decreased or increased in q_{max}) / (q_{max} with basic slurry density)×100 % Cui Y., and Kohata Y. (2020) the average increasing rate in the laboratory and in-situ curing is shown to be about 40 % in case of the specimen with larger slurry densities, whereas the average decreasing rate in the laboratory and in-situ curing are shown to be 30 % and 14 % in case of that with lower slurry densities, respectively. This result shows that the strength of LSS cured in-situ decreased significantly compared to that of LSS cured laboratory. Therefore, it is considered that the quality of LSS reduces construction site when using LSS prepared by a lower slurry density to reduce the overburden pressure, then it should be careful. Moreover, the q_{max} of in-situ specimens substantially tends to be higher than that of laboratory specimens, and it is independent of slurry density. However, in Figure 5-2 b), the gradient of the q~ε_a relation at small strains for in-situ specimens are less than that of laboratory specimens as shown in Figure 5-1 b), whereas in Figure 5-2 a), the q_{max} of in-situ specimens for large slurry density is large than that of laboratory specimens. This indicates

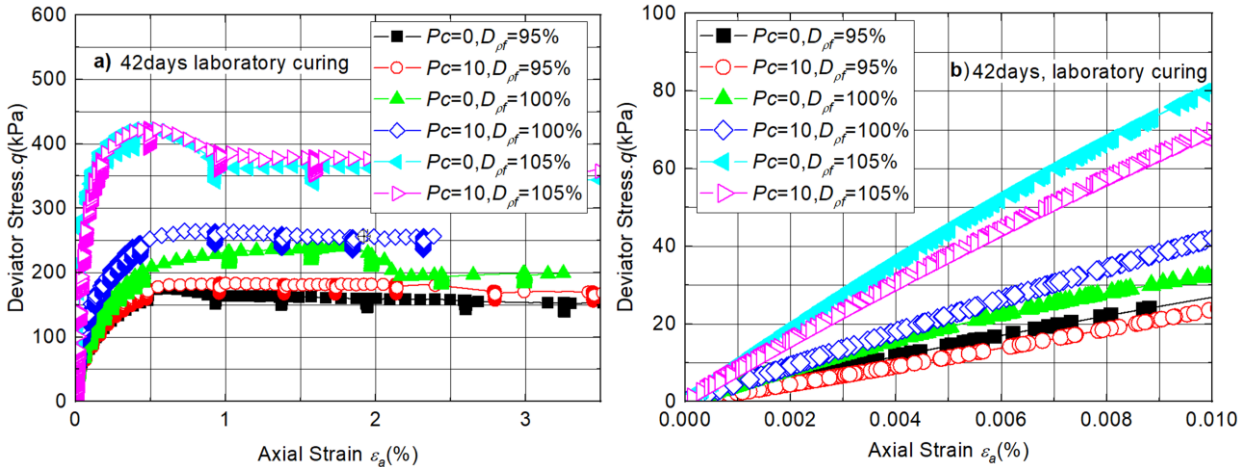

Figure 5-1 q vs ε_a relation of 42 days curing laboratory specimens; a) The relation up to 3.5 %, b) The relation up to 0.01 %

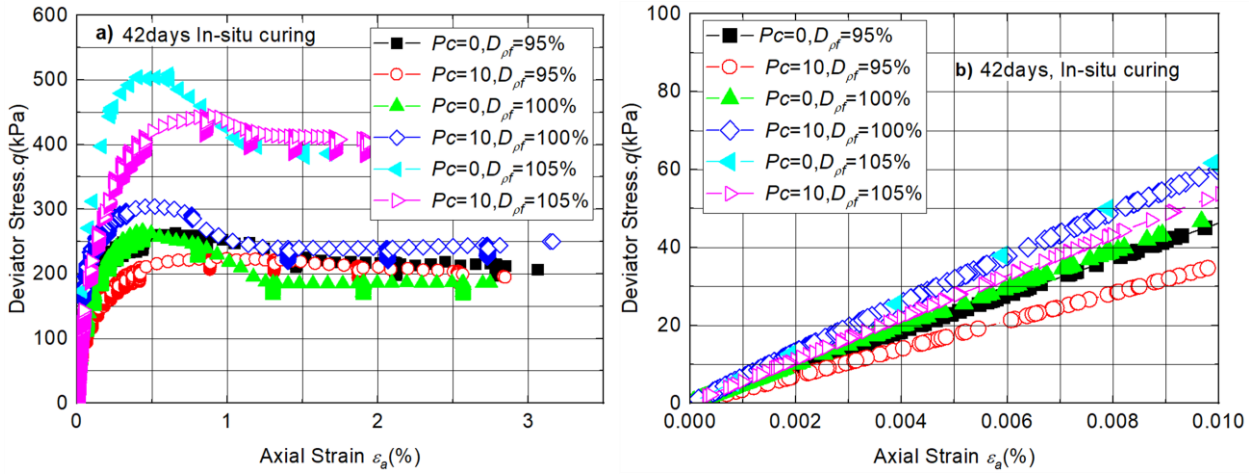

Figure 5-2 q vs ε_a relation of 42 days curing in-situ specimens; a) The relation up to 3.5 %, b) The relation up to 0.01 %

that when increasing slurry density at the laboratory, the stiffness at small strain increases compared to the other specimens that tend to only slightly increase at in-situ conditions. It is considered that the magnitude of viscous resistance appears to decrease with an increase in plasticity and water content at in-situ, Tatsuoka et al. (2007). As a result, increases or decreases in slurry density have a greater influence on the stiffness of the LSS cured laboratory than when it is cured in-situ.

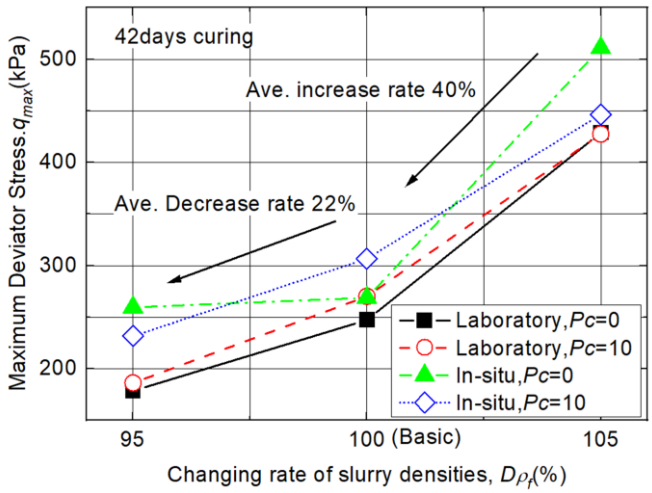

Figure 5-3 Relationship between q and changing rate of slurry densities

As the cement-based solidification material of LSS increases, the property of LSS becomes more brittle. However, when adding fiber material, in the q~ε_a curve after the peak, the value of q becomes nearly constant or slightly decreases in the majority of the cases. This indicates that by mixing fiber material, the brittleness property, ductile performance, and residual strength of LSS were significantly improved after the peak. This is verified by many previous studies. From the test results in this study, it is found that the q_{max} of basic slurry density increases in LSS with fiber material (Pc=10) cured at both laboratory and in-situ. On the other hand, it is found that the q_{max} of high slurry density decreases in LSS with fiber material (Pc=10) cured in-situ compared to LSS without fiber material (Pc=0). It is considered that when adding fiber material and increasing slurry density, the cement-hydration process was delayed during the early curing stage due to decreasing water content and fluidity at in-situ.

In order to estimate the brittleness property after the peak, the brittleness index (I_B), Consoli NC et al. (2002) was defined in this study as shown in Figure 5-4.

$$I_B = (q_{max}/q_{res}) - 1 \quad (5.1)$$

Where q_{max} is the maximum deviator stress and q_{res} is the residual deviator stress. As the value of the brittleness index I_B decreases and approaches zero, the failure behavior becomes increasingly ductile and the brittleness property is improved.

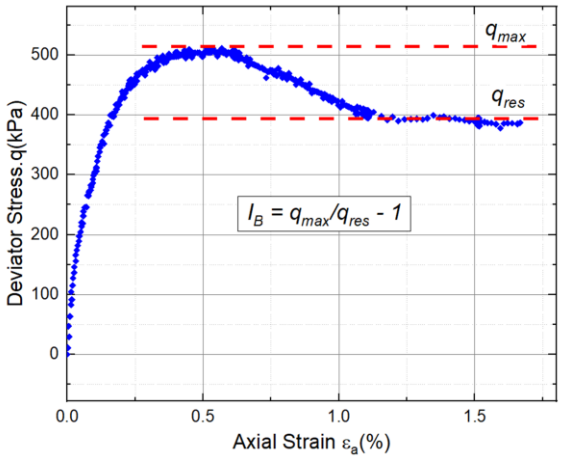

Figure 5-4 The definition of I_B value

Figure 5-5 a) shows the comparison of the value of I_B for LSS without fiber material (Pc=0) and LSS with fiber (Pc=10). The I_B value of LSS with fiber (Pc=10) becomes roughly one-half of the value of I_B of LSS without fiber (Pc=0). In comparison to the basic slurry density ($D_{\rho f}$=100 %), the improvement effect of brittleness decreased with increasing slurry density in LSS of Pc=10 cured laboratory, but it improved significantly in LSS of Pc=10 cured in-situ as shown in Figure 5-5 b). This result can be seen as the most effective method to mix fiber into LSS with changing slurry density to improve the brittleness property, to increase ductile performance, and seismic resistance at the construction site, although there was a slight decrease in q_{max} value.

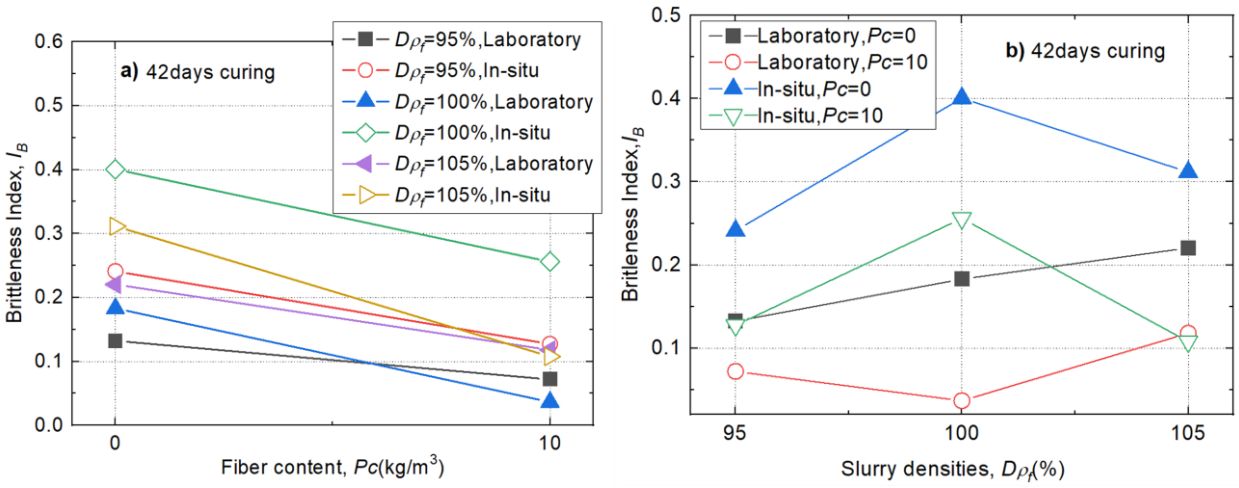

Figure 5-5 Relationships between I_B and a) fiber content, b) changing rate of slurry densities

5.2.2. Effect of Curing Time

The effect of curing time on strength and post- peak brittleness property of LSS in various conditions (amount of fiber material *Pc*, curing condition) was investigated. The relationship between q and ε_a up to ε_a=3.5 % based on LDTs measurement with the basic slurry density $D_{\rho f}$=100 % at prescribed curing time at the laboratory and in-situ is shown in Figure 5-6 and Figure 5-7. The figures show that the maximum deviator stress q_{max} increased with increasing curing time in most cases.

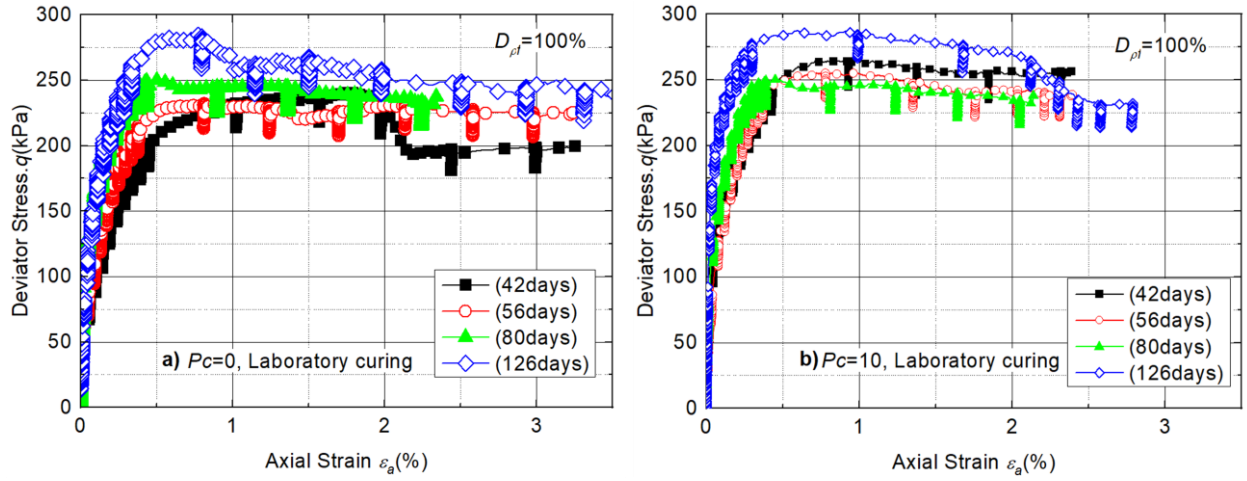

Figure 5-6 q vs ε_a relation with $D_{\rho f}$=100%, *Pc*=0; a) *Pc*=0, Laboratory curing, b) *Pc*=10, Laboratory curing.

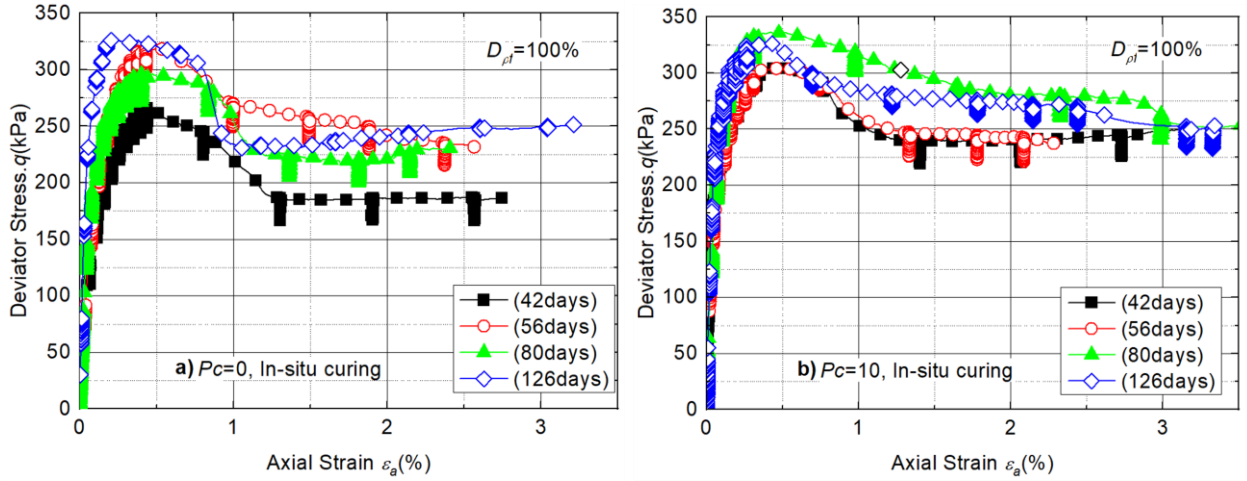

Figure 5-7 q vs ε_a relation with $D_{\rho f}$=100%, *Pc*=10; a) *Pc*=0, In-situ curing, b) *Pc*=10, In-situ curing

Figure 5-8 shows the relationship between q_{max} and curing time, t by both logarithms. The $q_{max} \sim t$ relation is linear as $q_{max}=a\times(t)^n$, Kohata Y et al. (2004). In both logarithm plots, the value of "n" represents the slope of the line obtained by a linear fit. The value of n becomes smaller than in cases of added fiber material (*Pc*=10) and cured in-situ. It means that the effect of aging on the increasing rate of the strength of LSS becomes small due to the addition of fiber material and curing at in-situ.

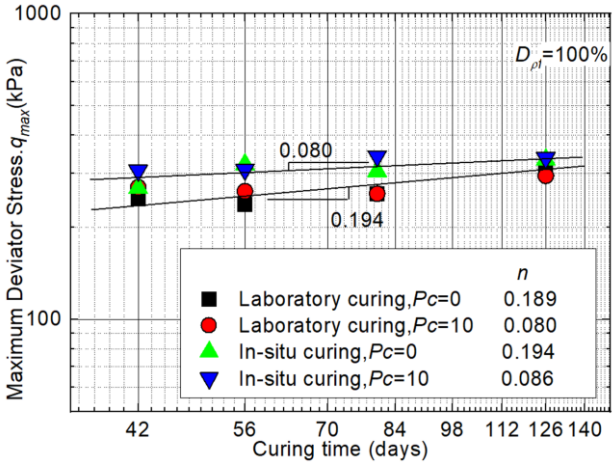

Figure 5-8 q_{max} *vs. t* relations

Figure 5-9 shows the relationship between I_B and curing time. It is found that in the case of specimens cured laboratory, there was an increasing tendency of I_B with increasing curing time. The value of I_B for LSS with fiber material cured in-situ increases slightly and indicates nearly constant value at a long period of time. On the other hand, the decreasing tendency of I_B was found for LSS without fiber material cured in-situ. It is considered that the post-peak brittleness property decreases due to the increasing cementation effect with increasing of curing time. It is found that by adding fiber material into in-situ samples, the effect of aging on post-peak brittleness improvement is negligible when compared to other conditions.

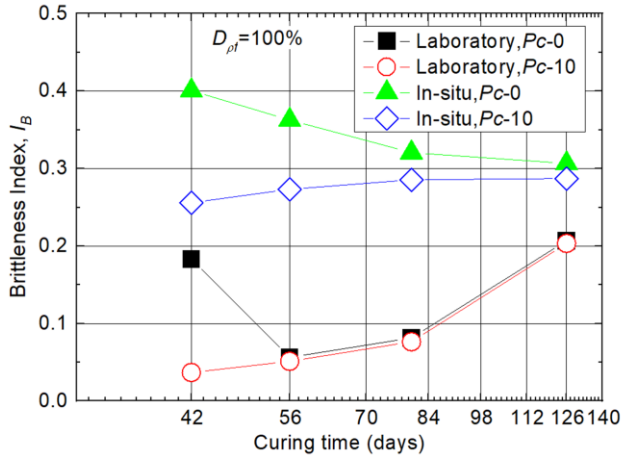

Figure 5-9 Brittleness index I_B vs. Curing time (days)

5.3. Pre-failure Deformation Property

Various Young's moduli are defined as shown in Figure 5-10 in this study. The initial Young's modulus E_0 is defined as an initial stiffness at ε_a less than about 0.002 % measured with LDTs. It is different from the undamaged elastic Young's modulus. The E_{tan} is defined as a tangential gradient in q~ε_a curve. This value indicates the non-linearity of the deformation property in q~ε_a curve. The value of peak-to-peak secant modulus from an unload/reload cycle is defined as the equivalent Young's modulus, E_{eq}, Tatsuoka et al. (1995), as shown

in Figure 5-10. The E_{50} value is obtained from the secant gradient between the coordinate origin and the point of $q_{max}/2$ on the $q \sim \varepsilon_a$ curve.

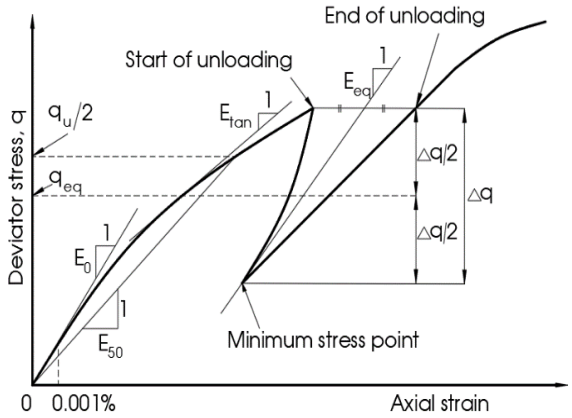

Figure 5-10 Definitions of E_0, E_{tan}, E_{eq}, E_{50}

5.3.1. Relationships between Young's Moduli E_0, E_{50}, and Maximum Deviator Stress q_{max}

It is convenient to estimate the E_0 value from the q_{max}, because the accurate calculation of E_0 is so often much more difficult than that of q_{max}. Figure 5-11 shows E_0 and $E_{50} \sim q_{max}$ relations. The figure shows that the relationship between E_0 and q_{max}, E_{50} and q_{max} are $E_0 \cong 1000 \sim 3000 \times q_{max}$ and $E_{50} \cong 600 \sim 1100 \times q_{max}$, irrespective of slurry density and curing time in most cases. However, the E_{50} value of LSS cured in-situ with low slurry density is large in compared with LSS cured laboratory, while the E_{50} value of LSS cured in-situ with high slurry density is smaller than laboratory ones. This result can be seen that the pre-failure $q \sim \varepsilon_a$ curve seemed to be more non-linear in LSS cured laboratory with low slurry density and in LSS cured in-situ with high slurry density than in others.

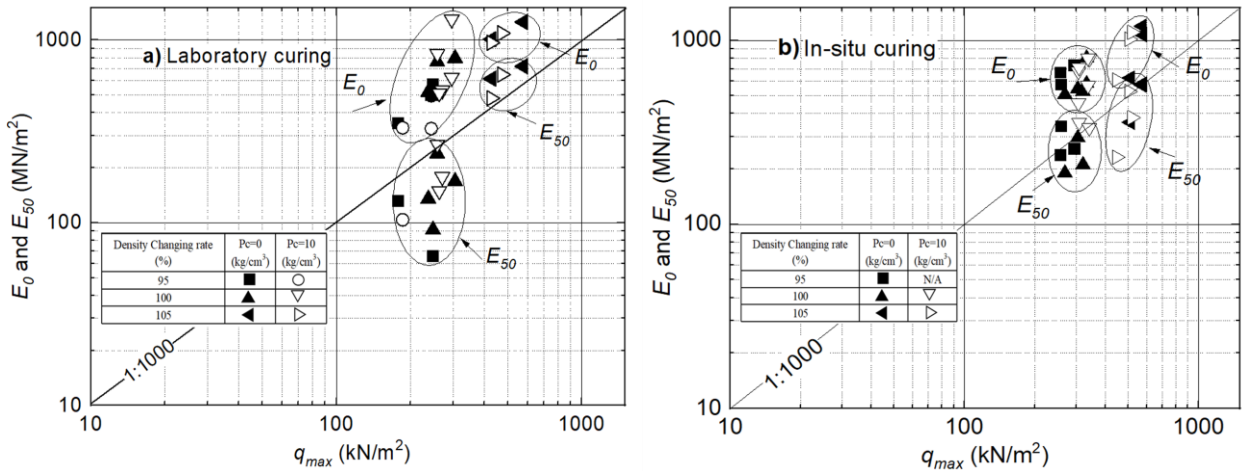

Figure 5-11 E_0, E_{50} *vs.* q_{max} relations; a) Laboratory curing, b) In-situ curing.

Figure 5-12 shows the effect of curing time on E_0. The increasing trend of E_0 for in-situ curing is observed at a relatively small curing period compared to E_0 for laboratory curing. That is, it is considered that the appearance of initial stiffness for in-situ curing becomes to delay compared to that for laboratory curing due to factors of curing temperature, humidity etc. at in-situ.

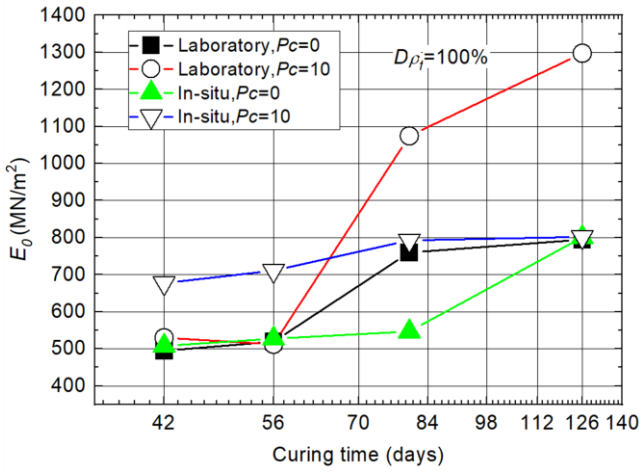

Figure 5-12 E_0 vs. Curing time (days)

5.3.2. Effect of Slurry Density

The relationship between the tangent Young's modulus normalized by the initial Young's modulus (E_{tan}/E_0) and the deviator stress normalized by the maximum deviator stress (q/q_{max}) in different cases is shown in Figure 5-13. These relations indicate the non-linearity of pre-failure deformation property and the degree of non-linearity can be compared normalizing the tangent Young's modulus and the deviator stress. Also, the relationship between the equivalent Young's modulus normalized by the initial Young's modulus (E_{eq}/E_0) and the deviator stress normalized by the maximum deviator stress (q/q_{max}) in different cases is shown in Figure 5-14. These relations indicate the degree of damage with shear in pre-failure deformation property.

In the case of in-situ curing as shown in Figures 5-13 c) and d), for Pc=0, the rate of decrease of E_{tan}/E_0 with shear is similar regardless of the slurry density up to q/q_{max}=0.4. The decreasing trend of E_{tan}/E_0 is largest when $D_{\rho f}$ = 100 %. On the other hand, for Pc=10, no effect of slurry density on the E_{tan}/E_0 to q/q_{max} relations is seen, and the curves are nearly identical. In the case of laboratory curing as shown in Figures 5-13 a) and b), the rate of decrease of E_{tan}/E_0 with shear is significantly greater for $D_{\rho f}$ = 105 % than for $D_{\rho f}$ = 95 % and 100 %, regardless of whether the fiber material is mixed or not. It was also observed that the decreasing trend of E_{tan}/E_0 for $D_{\rho f}$ = 95 % at ranges greater than q/q_{max}= 0.4 is increasing. In in-situ curing, the appearance of strength is slower than in laboratory curing due to factors such as curing temperature and humidity. Then, it is assumed that the effects of mixing a fiber material and the changing of slurry density were not appeared noticeably in the curing time at 42 days. On the other hand, it is considered that the effect of slurry density on the E_{tan}/E_0~q/q_{max} relations was appeared more significantly for $D_{\rho f}$ = 105 % in the curing time at 42 days, because the curing environment is controlled in laboratory curing.

As the shear deformation increases due to the damage to the micro-structure and the increase in viscous-plastic effect as well, the unload/reload stress-strain curves become more open when evaluated at shear stress

levels closer to the peak stress state. That is, if E_{eq}/E_0 is less than 1.0, the E_{eq} value may become less than the corresponding E_0 value Tatsuoka et al. (1995).

In the laboratory curing as shown in Figures 5-14 a) and b), there is the effect of slurry density on the E_{eq}/E_0~q/q_{max} relations, regardless of the amount of fiber material. Especially, the degree of damage for $D_{\rho f}$ = 105 % is the smallest. On the other hand, in the in-situ curing as shown in Figures 5-14 c) and d), it is not seen that the effect of slurry density and amount of fiber material on the degree of damage with shear is not seen significantly.

As a result, it is found that the effect of the slurry density on the LSS with fiber material cured in-situ is much more non-linear in the pre-failure deformation, and more ductile in the post-peak deformation. It is proposed to use LSS with varying slurry densities to increase seismic resistance and reduce overburden loads on construction sites.

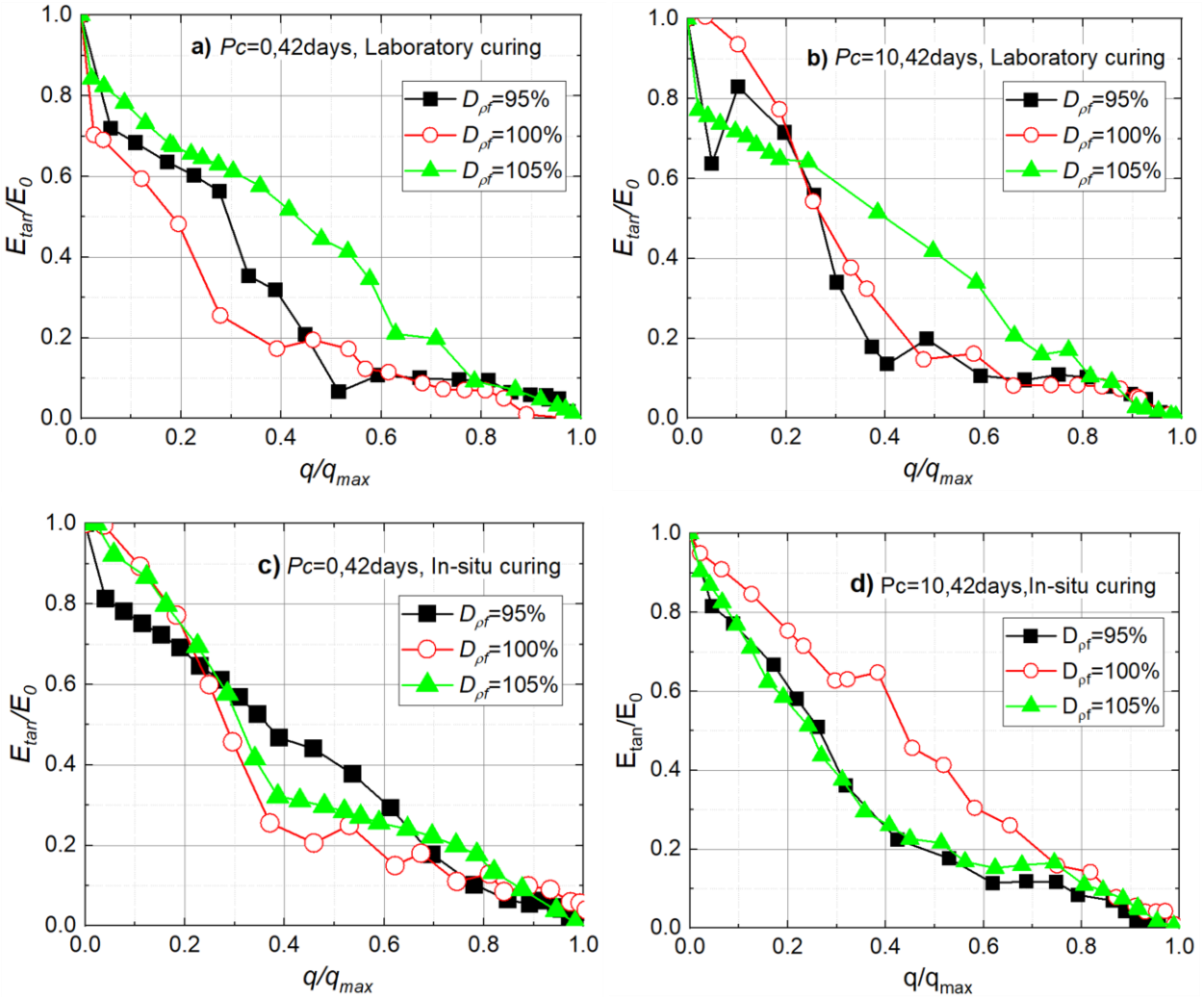

Figure 5-13 Effect of slurry density on E_{tan}/E_0 vs. q/q_{max} relations; a) Pc = 0, 42 days, Laboratory curing, b) Pc = 10, 42 days, Laboratory curing , c) Pc = 0, 42 days, In-situ curing, d) Pc = 10, 42 days, In-situ curing.

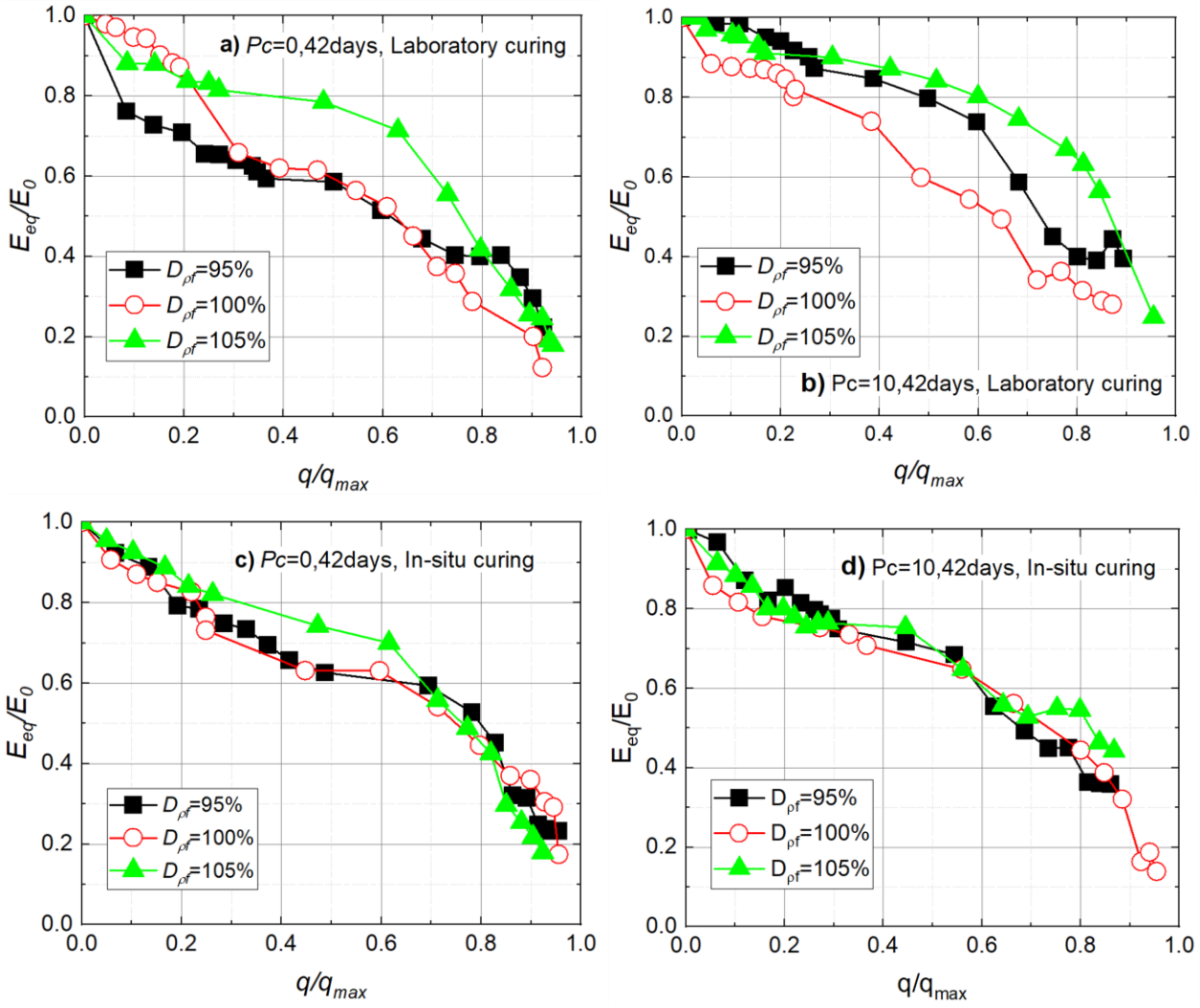

Figure 5-14 Effect of slurry density on E_{eq}/E_0 vs. q/q_{max} relations; a) Pc = 0, 42 days, Laboratory curing, b) Pc = 10, 42 days, Laboratory curing , c) Pc = 0, 42 days, In-situ curing, d) Pc = 10, 42 days, In-situ curing.

5.3.3. Effect of Curing Time

The influence of curing time on the non-linearity of the stress-strain relationship in the pre-failure region and the effect of the shear stress during aging on the non-linearity are analyzed as shown in Figure 5-15 and Figure 5-16. In the E_{tan}/E_0 ~q/q_{max} relations in Figures 5-15 a) and c), the value of E_{tan}/E_0 is not decreased up to around q/q_{max} = 0.2 with increasing curing time for LSS in both the laboratory and in-situ cases. The decreasing tendency of E_{tan}/E_0 with increasing of q/q_{max} in more than q/q_{max} = 0.4 is large at a long time of curing (126 days) in both cases. However, by adding fiber material into specimens cured in-situ, the non-linearity of the pre-failure q~ε_a curve seems to become rather independent of curing time in Figures 5-15 b) and d). Moreover, it can be seen that it is difficult to predict the influence of curing time on the non-linearity of the pre-failure q~ε_a curve due to uncontrolled environmental conditions. For this result, it is considered necessary to conduct further work that controls more factors influencing specimens in the coming time.

Figures 5-16 a) and b) show that the degree of damage with shear for laboratory curing in both cases of LSS without fiber material and with ones seems to become independent of curing time. Meanwhile, the E_{eq}/E_0 for in-situ curing as shown in Figures 5-16 c) and d) is larger than when compared with laboratory curing. In particular, by mixing fiber material at in-situ, the remarkable effect of curing time on the E_{eq}/E_0~q/q_{max} relations is large, as shown in Figure 5-16 d). The value of E_{eq}/E_0 increases remarkably as the curing time increases. It is considered that this is due to a decrease of the viscous component of deformation during unload / reload cycle with shear as the curing time increases and an increase of the elastic component of strain by increasing of curing time in in-situ curing. This property is similar to that of cement-treated gravelly soil Tatsuoka et al. (2007).

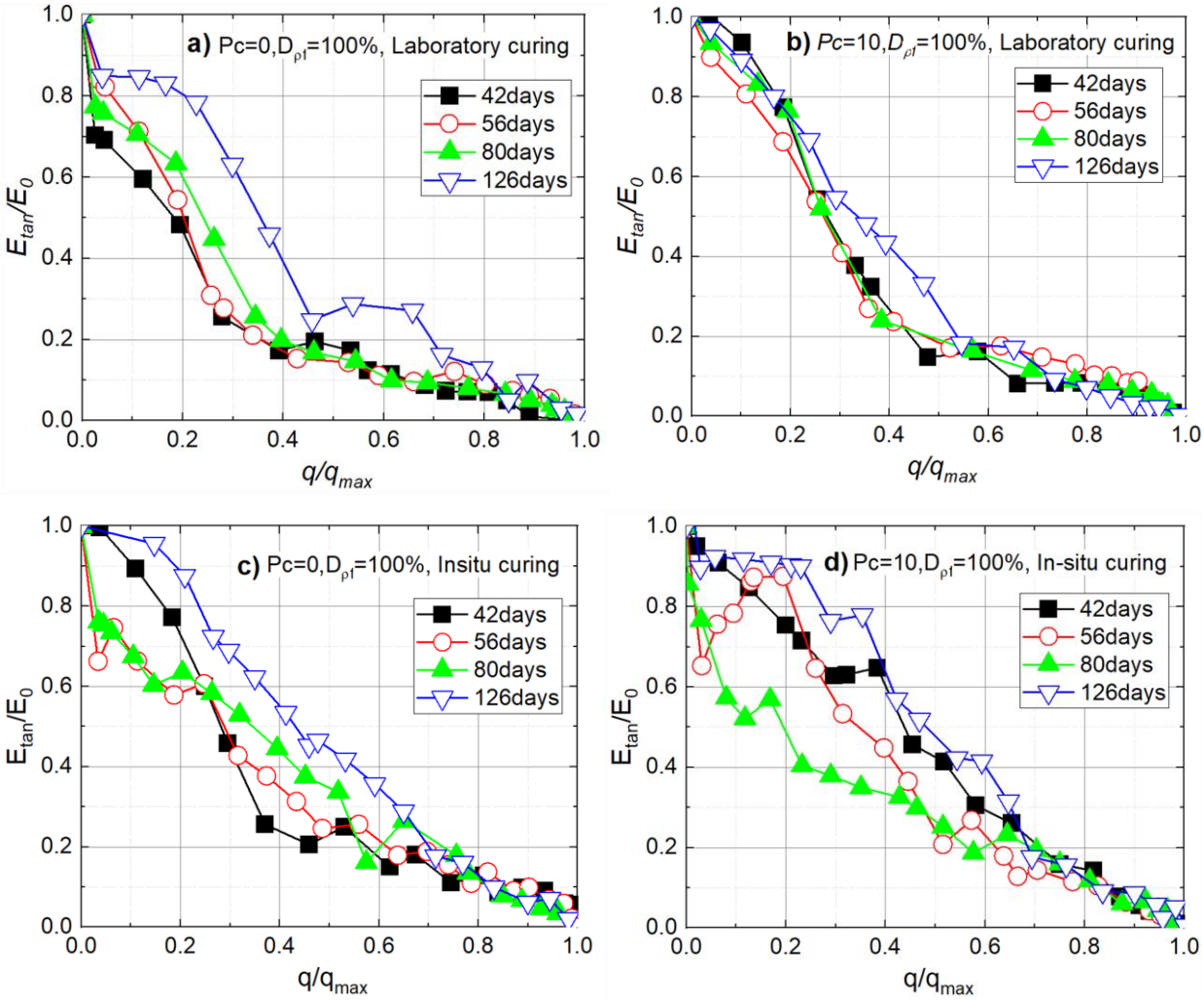

Figure 5- 15 Effect of curing time on E_{tan}/E_0 vs. q/q_{max} relations; a) Pc = 0, 42 days, Laboratory curing, b) Pc = 10, 42 days, Laboratory curing , c) Pc = 0, 42 days, In-situ curing, d) Pc = 10, 42 days, In-situ curing.

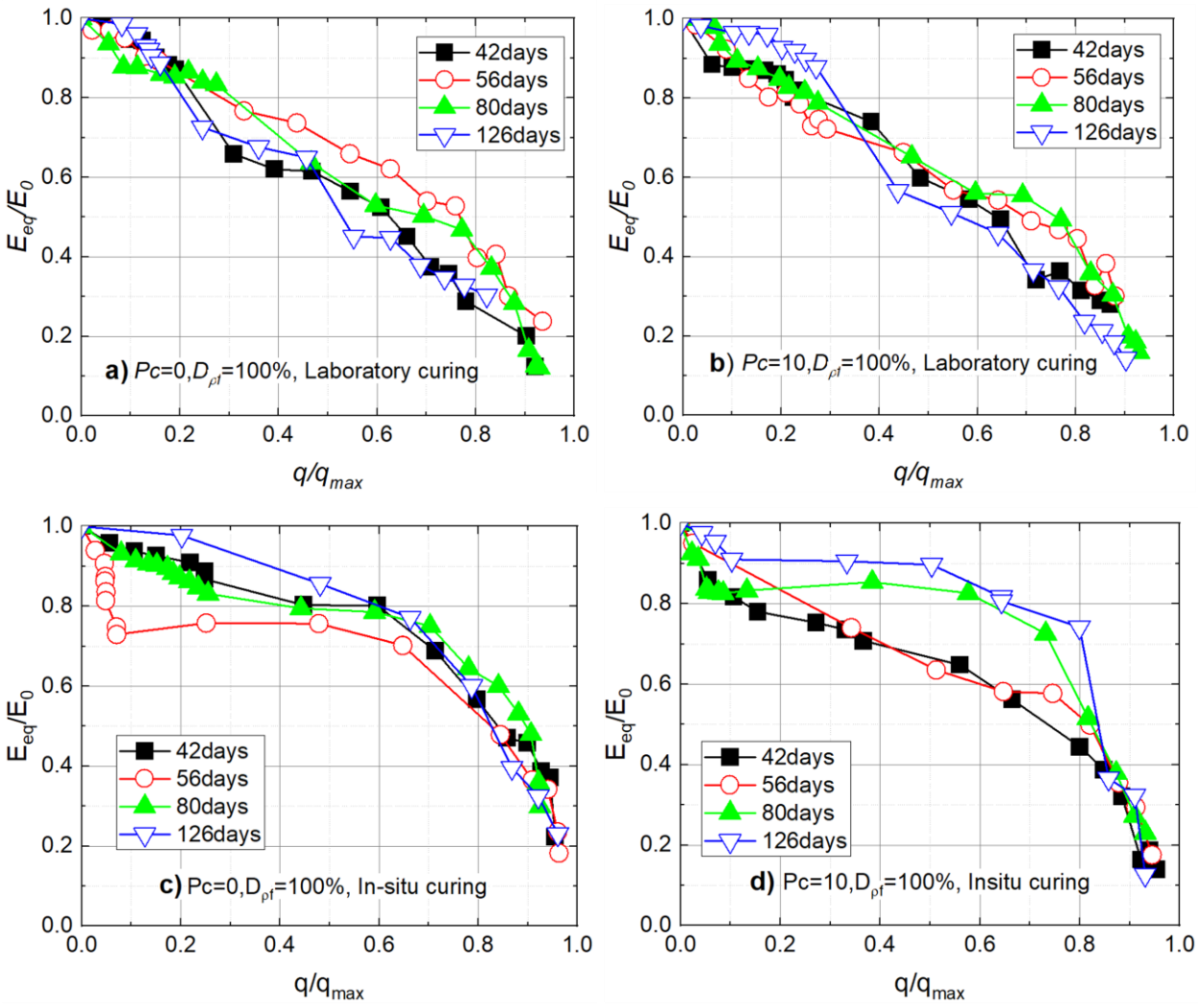

Figure 5-16 Effect of curing time on E_{eq}/E_0 vs. q/q_{max} relations; a) *Pc* = 0, 42 days, Laboratory curing, b) *Pc* = 10, 42 days, Laboratory curing , c) *Pc* = 0, 42 days, In-situ curing, d) *Pc* = 10, 42 days, In-situ curing.

5.4. Summary

Based on the results of a series of undrained triaxial compression tests on LSS mixed with and without fiber material, the following conclusions were obtained.

1) The slurry density had a considerable effect on the strength of LSS, with increasing density resulting in a 40 % rise in value of q_{max} and lowering density resulting in a 20 % drop in value of q_{max} when the density was changed at the same rate.

2) According to the brittleness index, the brittle properties of LSS were improved significantly about twice by adding fiber material.

3) The relationship between the $\log(q_{max})$ and $\log(t)$ is linear. It seems that $q_{max}=a\times(t)^n$ is approved to the relation between q_{max} and curing time, t of cement-treated soil including LSS.

4) In case of in-situ curing, the effect of curing time on the increasing rate of strength is small when compared to LSS without fiber material cured laboratory. The appearance of cementation was considered to be delayed due to adding fiber material and increasing water content at in-situ.

5) The relationship of $E_0\cong1000\sim3000\times q_{max}$ and $E_{50}\cong600\sim1100\times q_{max}$ irrespective of slurry density and curing time in almost cases is approved to the relationship between E_0 and q_{max} of cement-treated soil including LSS.

6) The effect of curing time on the initial Young's modulus, E_0, is smaller than the effect of slurry density with LSS cured in-situ. In particular, the E_0 value is more sensitively changed by the slurry density with LSS cured laboratory.

7) The slurry density has a substantial influence on the stress-strain relationships of LSS with fiber material cured in-situ**.** With increasing slurry density, the pre-failure stress-strain relation becomes more non-linar and the post-peak stress-strain relation becomes more ductile, while q_{max} decreases slightly. Furthermore, the influence of shear stress level on the degree of damage appears to be independent of slurry density.

8) By adding fiber material into LSS cured in-situ, the non-linearity of pre-failure $q\sim\varepsilon_a$ curve seems to become rather independent of curing time, the effect of curing time on the post-peak deformation is negligible, while the effect of curing time on the degree of damage is found to be largely due to a decrease in the viscous component of deformation and an increase of the elastic component of strain.

9) Since uncontrolled environmental factors make it much more difficult to predict the strength and deformation behavior of LSS cured in-situ. It is considered necessary to conduct further work that controls more factors influencing specimens

CHAPTER 6

TEST RESULTS AND DISCUSSION OF UNDRAINED CYCLIC TRIAXIAL TESTS ON REINFORCED LIQUEFIZED STABILIZED SOIL

6. Test Results and Discussion of Undrained Cyclic Triaxial Tests on Reinforced Liquefied Stabilized Soil

6.1. Introduction

In the previous chapter, the main mechanical characteristics of reinforced Liquefied Stabilized Soil (LSS) have been obtained from a series of monotonic tests. The effect of curing time, laboratory and in-situ curing, slurry density, and amount of fiber material on LSS were investigated by undrained triaxial tests. This chapter investigates how LSS behaves when subjected to cyclic loading with an emphasis on the samples cured in the laboratory and 28 days of curing time. In the cyclic test, the influences of cyclic test variables such as consolidation pressure, displacement rate, stress amplitude, the initial stress ratio, and the control (stress vs. strain cycles) and LSS material variables such as slurry density, fiber material, and cement on LSS have been studied.

This chapter is arranged in the following order: Firstly, an overview of the cyclic definitions and framework adopted in this investigation are described. The utilized cyclic loading characteristics and test schedule summaries are then presented, followed by an interpretation and discussion of the experimental results. The chapter finishes with an examination of the stiffness and damping characteristics.

6.2. Cyclic Definitions

6.2.1. Cyclic Loading Shape

In this thesis, the stress-controlled cyclic tests include symmetrical and non-symmetrical loading tests with a triangular wave pulse. As shown in Figure 6-1, when initial static stress σ_s equals 0, the cyclic tests are subjected to symmetrical loading, on the other hand, when σ_s does not equal 0, the cyclic tests are subjected to non-symmetrical loading. In the case of two-way cyclic loading, on the other hand, the applied cyclic load alternates in either direction around a certain mean value, which means that σ_s is less than σ_d. When the σ_s value is 0, it is termed symmetrical two-way cyclic loading, otherwise unsymmetrical.

In the following sections, this chapter will present the results and interpretation of a series of symmetrical and unsymmetrical cyclic loading tests on unreinforced and reinforced LSS.

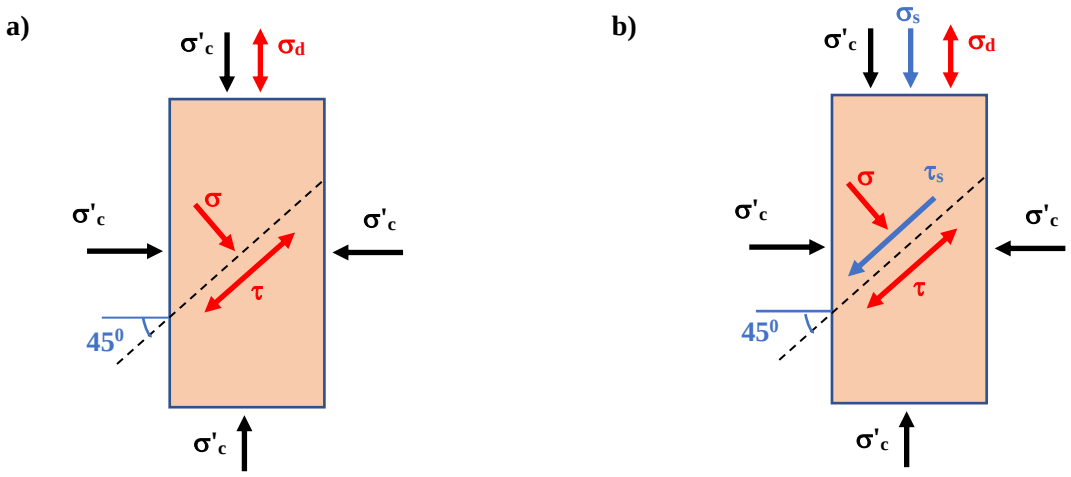

Figure 6-1 Elemental stress state; a) Isotropic triaxial shear, b) Anisotropic triaxial shear

σ_c': Effective confining stress, σ_d: Cyclic stress amplitude, σ_s: Initial static stress

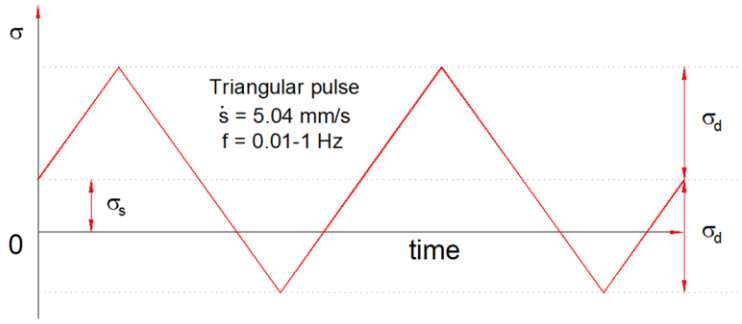

Figure 6-1-A Cyclic load shape

6.2.2. Loading Frequency

In Peralta (2010) a definition of cyclic loading is given as a load frequency between 0 and 1 Hz, as shown in Table 6-1. Furthermore, inertia forces can be neglected due to the low frequency, and the accumulated strain is predominantly plastic.

Table 6-1 Approximate classification of repeated loading of soils. Peralta (2010)

Repeated Loading of Soils	Cyclic	Cyclic - Dynamic	Dynamic
Frequency	0 to 1 Hz	1 to 10 Hz	10 to 100 Hz
Inertia	No (negligible)	Yes (relevant)	Yes (relevant)
Strain accumulation	Predominantly	Plastic and elastic	Predominantly elastic

As discussed in section 3.5.3, cohesive soils show increased cyclic shear strength under high-frequency loading than under low-frequency loading. In general, for a given number of cycles, lower frequencies cause higher shear strain and excess pore pressures.

In this study, the magnitude of the deviatoric stress was determined from the output of a load cell, located inside the triaxial chamber. In the repeated load tests, the deviatoric stress was applied in the manner shown in Figure 6-1. In almost tests, the axial displacement rate keeps at a constant value equal to 5.04 %/min, providing optimum value when considering the trade-off between test duration and control, precision, and data acquisition and enough slow for the distribution of pore water pressure throughout the sample. Due to the progressive decrease in stiffness and the constant displacement rate, the period T of the individual cycles gets larger with the increasing duration of a test and the range of frequency from 0.01 Hz to 1 Hz was used.

6.2.3. Cyclic Stress Ratio

The cyclic resistance of soil is often described as the maximum number of loading cycles (N_f) that the soil can withstand for a certain value of cyclic stress ratio; Cyclic stress ratio (*CSR*) is defined as the ratio of cyclic shear stress to the effective confining pressure. For an undrained cyclic triaxial loading, the *CSR* value reduces hyperbolically with the increasing number of loading cycles and is defined as

$$CSR = \frac{\sigma_d}{2\sigma_c'}$$

Where σ_d is effective cyclic deviatoric stress and σ_c' is effective confining pressure.

Larew and Leonards (1962) noted the existence of limiting cyclic stress levels for compacted soil samples in one of the early experimental studies of the cyclic response of cohesive soils. For stress levels below such a limit, no excess pore pressure is accumulated, nor does it suffer any degradation in stiffness. In short, the sample exhibits an essentially elastic response. If the cyclic stress amplitude exceeds the limiting mentioned above value,

the sample exhibits an inelastic response, possibly leading to failure. Several investigators subsequently confirmed the existence of limiting cyclic stresses, which were typically referred to as "threshold cyclic stresses" or "Critical cyclic stresses".

This thesis performed cyclic tests with different stress amplitudes in the range of 40 kPa ≤ σ_d ≤ 120 kPa (0.204 ≤ *CSR* ≤ 0.6) at 98.1 kPa of isotropic consolidation stress. At the end of the tests, the graphs of cyclic stress ratio versus several cycles for a particular double amplitude axial strain are plotted for different cyclic stress ratios to compare the results. The threshold stress level was found and interpreted in detail.

6.2.4. Porewater Pressure Ratio

Excess pore pressures tend to increase when soils are subjected to undrained cyclic loading in cyclic triaxial tests, eventually approaching a value equal to the initial effective cell pressure, σ_c'. Excess pore pressures are therefore typically expressed as the pore water pressure ratio, $\Delta u'$, where:

$$\Delta u' = \frac{\Delta u}{\sigma_c'}$$

Where:

$\Delta u = u(N) - u\ (N=0)$: excess pore water pressure

σ_c' = effective confining stress

For loose sands, the first instance of $\Delta u'$ = 1.0, termed 'initial liquefaction' by Lee & Seed (1967), is immediately followed by significant deformation and a sudden and complete loss of strength. Medium-dense to dense sands also undergoes a state of softening on achieving 100 % porewater pressure build-up. Still, subsequent deformations do not grow indefinitely large, and complete loss of strength does not occur Ishihara (1996). However, significant cyclic strains are mobilized following this condition, which is why the state of 100 % excess pore pressure build-up (i.e., $\Delta u'$= 1.0) is often used as a measure of cyclic instability. For cohesive undrained soils, true liquefaction does not occur in cohesive soils because 100 % excess pore water pressure during cyclic loading does not generally occur. Even, if it does occur and the effective stress reaches zero, the clay could exhibit strength on account of cohesion. In this regard, liquefaction in clay is defined as the unacceptable deformation of soil.

Dobry et al. (1982) investigated the build-up of pore pressures and liquefaction susceptibility of sands. They found that there is a predictable correlation between the cyclic shear strain amplitude and the excess pore water pressures developed. They also suggested that no excess pore pressures will develop if cyclic shear strains remain lower than the threshold strain due to no inter-particle sliding occurring at the particle contacts.

6.2.5. Number of Loading Cycles

Every loading cycle contributes to the pore water pressure build-up for a given cyclic stress amplitude above the threshold value. It causes the stress-strain behavior of soil to migrate towards the failure line observed in the cyclic loading pattern. In reality, earthquakes generate very irregular cyclic loading pulses. Still, it is often simplified to a certain number of uniform sinusoidal or triangular loading cycles (*N*) with some cyclic stress amplitude (σ_d) value based on the intensity of the earthquake Seed and Idriss (1982). The number of uniform sinusoidal or triangular loading cycles (*N*) required to represent an earthquake of magnitude Mw has been proposed by many researchers. The relationship presented by Boulanger and Idriss (2004) is commonly accepted (Figure 6-2). Typically, earthquake loads can trigger 1 to 40 uniform sinusoidal loading cycles. Therefore, the

cyclic deviatoric stresses were chosen carefully in each test with the target of failing the sample from a few to a few hundred cycles. The first cyclic deviatoric stress level was estimated from the monotonic shear strength value of the identical tested samples. After that, the consequent cyclic stress levels were determined using the outcome of the first cyclic test to obtain the number of cycles close to the targeted values. However, to investigate the influence of various initial conditions, the number of loading cycles in cyclic tests in the thesis might be reached more than 10000 cycles.

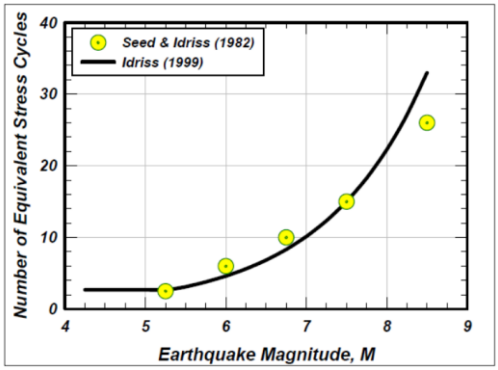

Figure 6-2 Relationship between earthquake magnitude and number of loading cycles after Boulanger and Idriss (2004)

In this research, the number of loading cycles N_c when a specific double amplitude axial strain DA is produced shall be calculated from the Japanese Geotechnical Society Standard (JGS 0541-2020).

$$N_c = \frac{DA - DA(N_i)}{DA(N_i + 0.5) - DA(N_i)} \times 0.5 + N_i$$

Where, the specific double amplitude strain DA (N_i), DA (N_i+0.5) when DA is 1, 2, 5, or 10%, etc., is the value of DA at N_i, (N_i+0.5) cycles respectively, and Nc is the number of cycles corresponding to DA (see Figure 6-3).

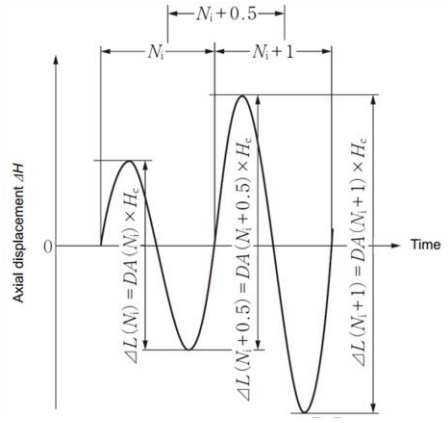

Figure 6-3 Explanation of the definition of the number of loading cycles N_c for a specific DA

6.2.6. Failure Criterion

The semantic problem of defining failure in a cyclic loading test has not been specifically solved, and the proposed definitions have not been universally accepted. True liquefaction does not occur in cohesive soils because 100 % excess porewater pressure during cyclic loading does not generally occur in clay. Even, if it does occur and the effective stress reaches zero, the clay could exhibit strength on account of cohesion. In this regard, liquefaction in clay is defined as the unacceptable deformation of soil, and therefore in this study, the cyclic loading was continued until the sample reached a double axial strain of 2.5 % (which is equal to a shear strain of 3.75 %) for symmetrical loading and permanent axial strain of 10% for nonsymmetrical loading. This value might seem closely relative to the monotonic axial strain taken from the static triaxial test.

Furthermore, as mentioned in chapter 4, the magnitude of the cyclic stress amplitude in the triangle wave is estimated from the load cell. This value is determined by the strength of the LSS reduced by each cycle. At certain cycles, the strength of the LSS will be less than the amplitude of the target wave, which means the load cell not found the target stress amplitude and cyclic loading will stop to prevent sample forced failure in extension or compression mode. This situation is also considered a failure criterion in this study. In the most cases, the axial strain when the triaxial apparatus stops coincides with the strain failure criterion at 2.5 %.

The experiments on cyclic loading of LSS have used the axisymmetric triaxial test wherein the cell pressure is held constant and the deviatoric stress pulsed. Under these conditions, the measured vertical deformation consists of two components as illustrated in Figure 6-4, the cyclic double axial strain ε_{DA} and the permanent axial strain ε_p.

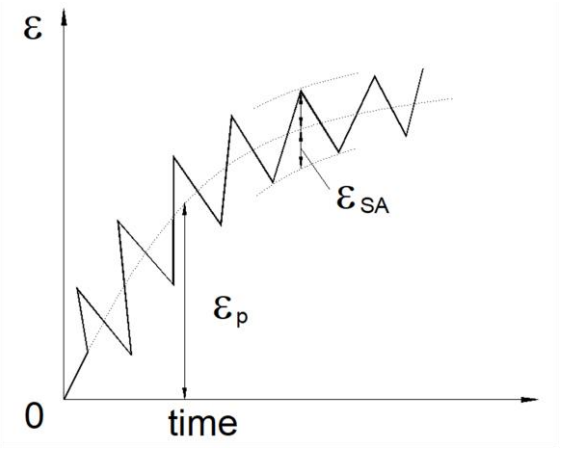

Figure 6-4 Variation of deformation during a cyclic load test (illustrative)

6.2.7. Stiffness and Energy Loss Factor

In this thesis, the equivalent Young's modulus E_{eq} (MN/ m^2) and the hysteresis factor h (%) shall be calculated from the Japanese Geotechnical Society Standard (JGS 0541-2020).

$$E_{eq} = \frac{\sigma_d}{(\varepsilon_a)_{SA}} \times \frac{1}{10}$$

$$(\varepsilon_a)_{SA} = \frac{\Delta L}{2H_n} \times 100$$

$$h = \frac{1}{2\pi} \cdot \frac{\Delta W}{W} \times 100$$

Where

σ_d : The single amplitude cyclic deviator stress (kN/m^2)

$(\varepsilon_a)_{SA}$: The single amplitude axial strain (%)

ΔL: Double amplitude axial displacement of the specimen ΔH in that cycle (mm)

H_n: Specimen height at the start of that cyclic loading stage (mm)

ΔW: The damping energy in that cycle, and is the area of the hysteresis curve prepared from the axial load difference P and the axial displacement ΔH (N·mm)

W: Equivalent elastic energy in that loading cycle, calculated from the following equation

$$W = \frac{(P_C + P_E)\Delta L}{4}$$

P_C, P_E: The single amplitude cyclic axial load on the compression side and the extension side in that cycle (N) (both positive values)

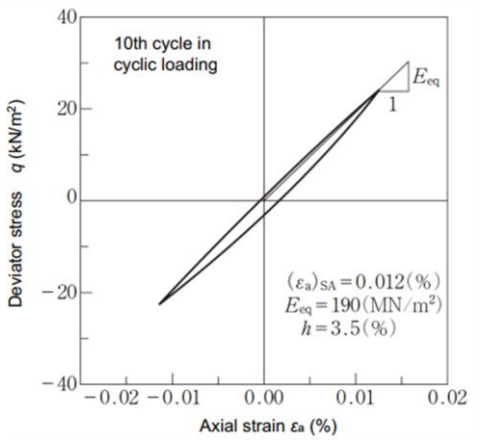

Figure 6-5 Example of the typical hysteresis curve

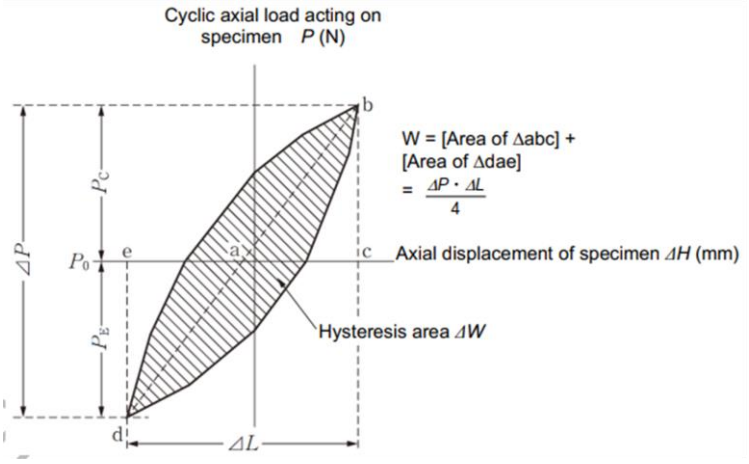

Figure 6-6 Explanatory diagram for hysteresis damping factor h

6.3. Cyclic Test Program

Table 6-2 The program of undrained cyclic triaxial tests

Test Series	Variation of	Specimen ID	Curing Time (days)	Slurry Density (g/cm^3)	Fiber Content (g/cm^3)	$\eta_0=\sigma_s/\sigma_c'$	σ_c' (kPa)	σ_s (kPa)	σ_d (kPa)	CSR=$\sigma_d/2\sigma_c'$	q_{max}	$\sigma_{d/}q_{max}$	Rate (%)	$\gamma^{failure}_{Static}$	N_f
Stress - control test															
C1	Slurry density and fiber	①	28	95	0	0	98.1	0	80	0.41			5.04	-	5
C2									67.5	0.344	124	0.54	5.04		22
C3									60	0.306	124	0.48	2.5		57
C4									60	0.306	124	0.48	1.02		28
C5		②						0	67.5	0.344	134	0.50	5.04		60
C6									67.5	0.344	134	0.50	1.02		45
C7									54	0.275	134	0.40	5.04		2024
C8		⑤		100	0				60	0.306	96	0.63			2000
C9									80	0.408	96	0.83	5.04		10
C10									67.5	0.344	96	0.70			456
C11									40	0.204	96	0.42			>11000
C12									54	0.275	96	0.56			>10000
C13		⑥			10			0	67.5	0.344	112	0.60			3405
C14									80	0.408	112	0.71			1075
C15		③		105	0			0	118	0.601	166	0.71			47
C16									67.5	0.344	166	0.41			>15000
C17		④			10			0	118	0.601	180	0.66			42
C18									67.5	0.344	180	0.38			>15000
C19	σ_d (σ_s=0)	⑥	28	100	10	0	98.1	0	39.24	0.200	112	0.35	5.04	1.35	>11000
C20									54	0.275	112	0.48			>11000
C21									67.5	0.344	112	0.60			3405
C22									80	0.408	112	0.71			1075
C23									98.1	0.500	112	0.88			42
C24	σ_c'	⑥	28	100	10	0	58.8	0	80	0.680	103	0.78	5.04	1.35	311
C25							196		80	0.204	131	0.61			3800
C26							58.8		32.34	0.275	103	0.31			>14000
C27							196		107.8	0.275	131	0.82			43
C28							58.8		73	0.621	103	0.71			810
C29							196		93	0.237	131	0.71			311
C30	σ_s	⑥	28			0.65	98.1	63.765	54	0.275	112	1.05			5
C31						0.59		58	54	0.275	112	1.00			80
C32						0.34		33.75	54	0.275	112	0.78			>7500
C33						0.55		54	54	0.275	112	0.96			505
C34						0.28		27	54	0.275	112	0.72			>6780
C35	Frequency	⑥	28	100	10	0	98.1	0	80	0.408	112	0.71	2.04	1.35	398
C36											112	0.60	5.04		1075
C37	Cement = 80%	⑥	28	100	10	0	98.1	0	54	0.275	-	-	5.04		>1100
C38									80	0.408	-	-	5.04		4
C39									67.5	0.344	-	-	5.04		73
Strain-control test															
C40	Stain-controlled	⑥	28	100	10	0	98.1	-	-	-	112		5.04	1.35	-
C41											112			2.7	-

6.4. Monotonic Test Results of LSS Cured at 28 days

Cyclic loading generally leads to a breakdown of the soil structure. For fully saturated, undrained conditions, volumetric changes due to dynamic loading are prevented due to the relative incompressibility of water, and instead manifest themselves as changes in the pore water pressure. The tendency for loose soils to contract results in an increase in pore pressure, and the effective stress in the soil decreases accordingly. Each additional stress cycle yields additional incremental pore pressure changes, until the stress path eventually reaches some failure envelope.

In addition, the number of equivalent loading cycles for an earthquake loading is primarily related to the intensity of earthquake. As discussed in the literature, a typical earthquake could trigger between 1 to 40 equivalent sinusoidal loading cycles. Therefore, the cyclic deviatoric stresses were chosen carefully in each test with the target of failing the sample from a few to a few hundred cycles. The first cyclic deviatoric stress level was estimated from the monotonic shear strength value of identical tested sample. Thereafter, the consequent cyclic stress levels were determined using the outcome of the first cyclic test to obtain the number of cycles close to the targeted values.

For above reasons, the monotonic behavior of unreinforced and reinforced LSS cured at 28 days was presented in this part of study. Especially the failure envelope (Critical State Line) was determined from the tests result data.

The program of the compression and tension triaxial tests with monotonic loading is summarized in Table 6-3. The LSS samples were isotropically consolidated to three different effective mean pressures σ_c' = 58.8, 98.1, and 196 kPa. The undrained monotonic shearing was applied with a displacement rate $\dot{s} = 0.054$ %/min. The measured development of deviatoric stress $q = \sigma_d' - \sigma_c'$ with axial strain ε_1 and the effective stress paths in the $p' - q$ plane with $p' = (\sigma_d' + 2\sigma_c')/3$ are given in Figure 6-7 b). With the exception of the final phase of the tests, the material response is contractive. The Critical State Line (CSL) of failure envelop for compression and tension

Table 6-3 The program of undrained compression and tension monotonic triaxial tests

Test Series	Variation of	Specimen ID	Curing Time (days)	Slurry Density (g/cm^3)	Fiber Content g/cm^3)	σ_c' (kPa)	Testing Condition
S1-C	Slurry density and fiber	①	28	95	0	98.1	**Laboratory**
S2-C		②			10		
S3-C		⑤		100	0		
S4-C		⑥			10		
S5-C		③		105	0		
S6-C		④			10		
S7-C	Confining	⑤	28	100	0	58.8	
S8-C		⑥			10		
S9-C		⑤			0	196	
S10-C		⑥			10		
S11-T	Tension	⑥	28	100	10	58.8	
S12-T						98.1	
S13-T						196	

modes shown as the dashed black lines in the p' – q plane in Figure 6-7 b) is further used in the analysis of the cyclic test data for comparison purposes.

The typical of tress–strain relationships and effective stress paths measured in undrained compression and tension monotonic triaxial tests on LSS mixed fiber with different effective mean pressures σ_c' as shown in Figure 6-7.

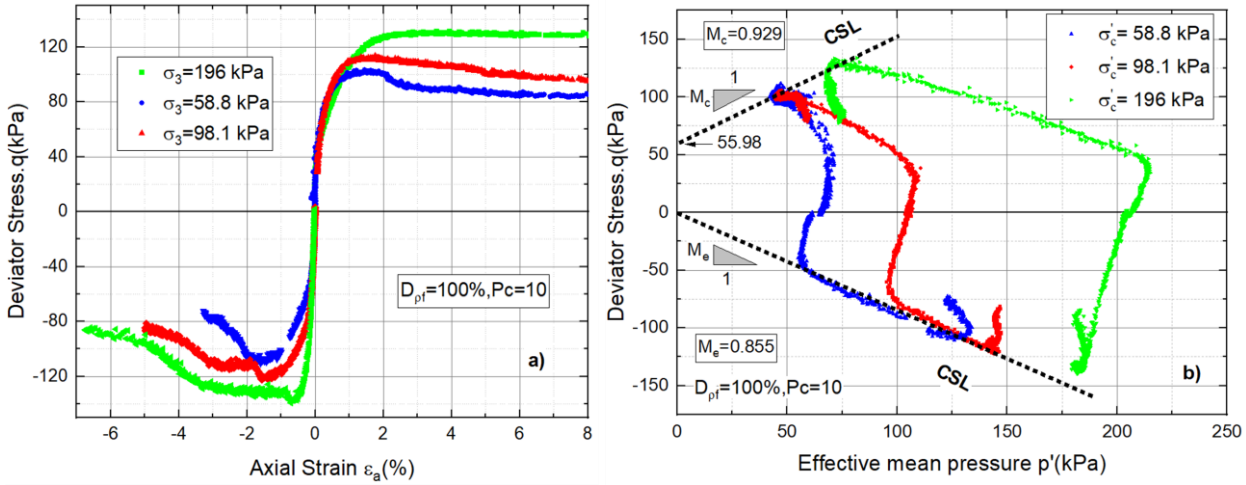

Figure 6-7 Typical of tress–strain relationships and effective stress paths measured in undrained compression and tension monotonic triaxial tests on LSS mixed fiber with different initial mean pressures σ_c'

The summary of effective stress paths and total stress paths measured in undrained compression and tension monotonic triaxial tests on LSS mixed fiber with different initial mean pressures σ_c' show in Figure 6-7-A

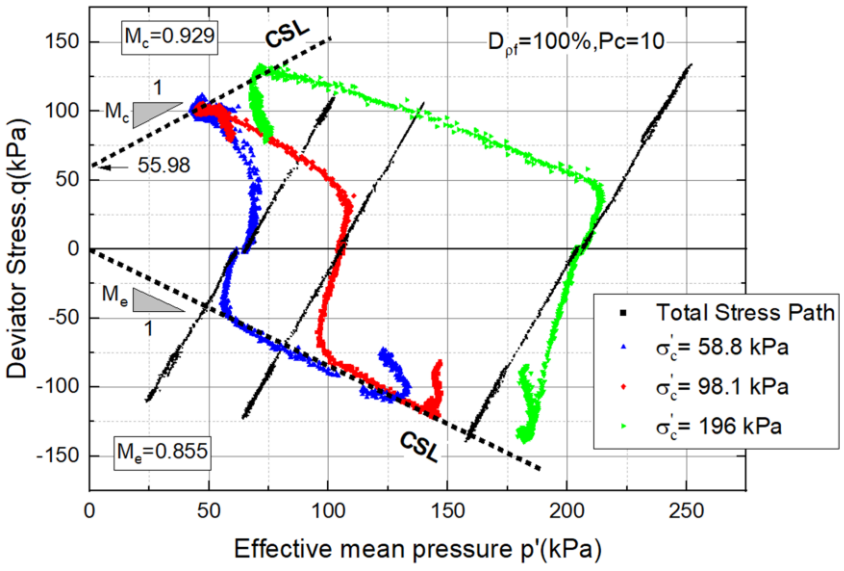

Figure 6-7-A Summary of the effective stress paths and total stress paths with different initial mean pressures σ_c'

6.5. Cyclic Test Results and Discussion

6.5.1. Variation of Stress Amplitude at Symmetrical Cyclic Loading

In order to investigate the effect of stress amplitude on the LSS mixed fiber material *(P_c = 10)* with basic slurry density ($D_{\rho f}$ =100 %). Five undrained cyclic triaxial tests C19-C23 were performed with isotropic consolidation (σ_c' = 98.1 kPa, σ_s = 0 kPa, η_0 = 0) and variation of the deviator stress amplitude 40 kPa $\leq \sigma_d \leq$ 98.1 kPa (0.204 $\leq$ *CSR* $\leq$ 0.5). The cyclic loading was applied with a displacement rate $\dot{s} = 5.04\ \%/min$.

A typical result on test C23 with deviatoric stress amplitude of σ_d = 98.1 kPa is given in Figure 6-8. A constant triangular deviatoric stress with a peak amplitude of 98.1 kPa was applied to the consolidated sample under undrained conditions. The figure shows the effective stress paths in *p'* - *q* space, stress-strain cyclic behavior, excess pore water pressure generation, and the axial strain progression in the sample with loading cycles. As seen that the sample reached failure criterion at the 42th loading cycle.

As shown in Figures 6-8, the excess pore water pressure (Δu) in the LSS sample continuously increases and simultaneously decreases the effective stresses of LSS with the number of loading cycles (*N*). As a result, the sample becomes weaker with the number of loading cycles, and accumulated axial strain increases gradually. In contrast to sand, Wichtmann et al. (2016), the true liquefaction (*p'* = *q* = 0) is not reached in this test on LSS

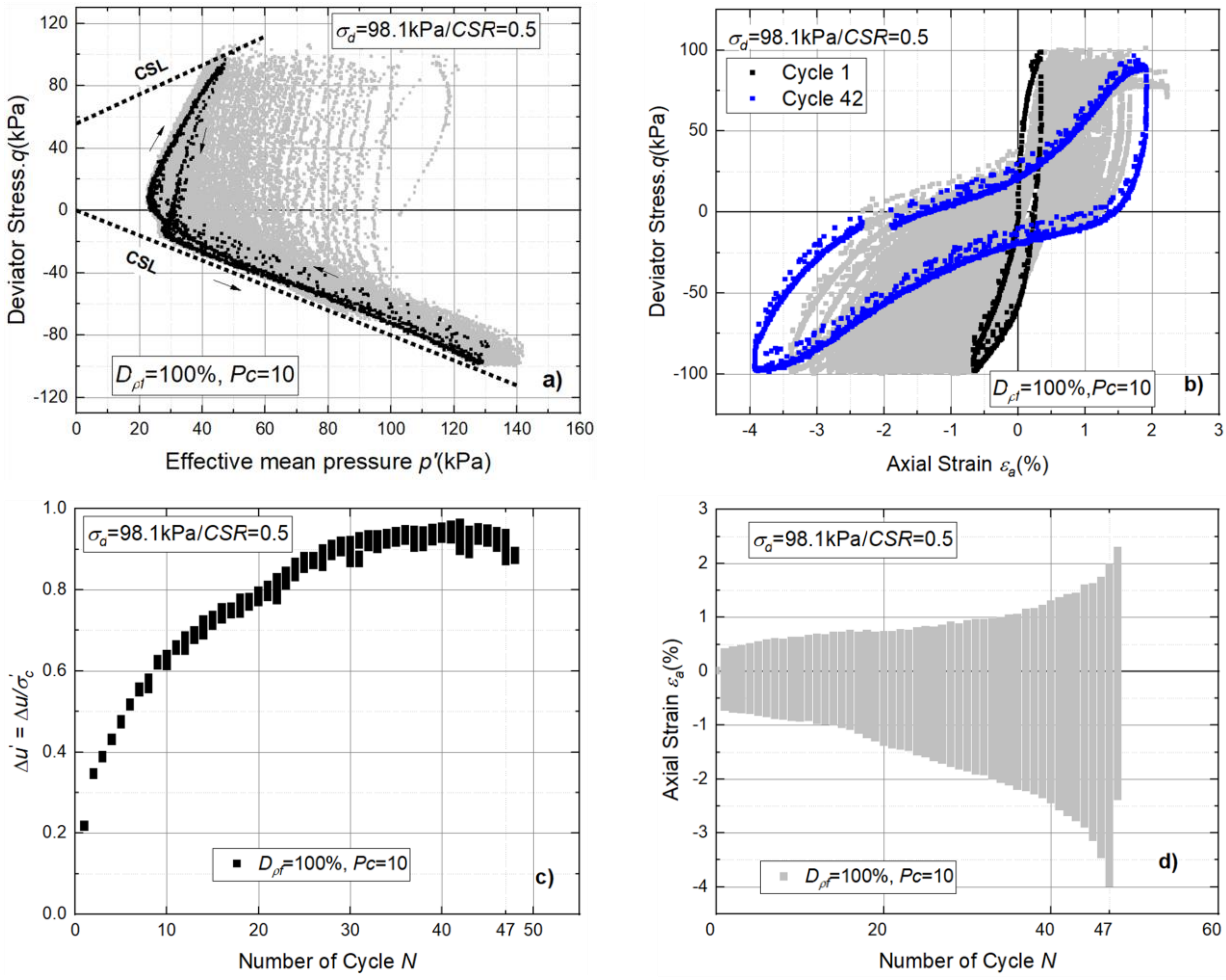

Figure 6-8 Typical results of an undrained cyclic test with σ_d = *98.1* kPa (test C22 in Table 5-2 with σ_c' = 98.1 kPa, σ_s = 0 kPa, η_0 = 0, $\dot{s} = 5.04\ \%/min$); a) Effective stress paths, b) Deviator stress *q* versus axial strain ε_a, c) Porewater pressure ratio versus number cycle *N*, d) Axial strain versus number cycle *N*.

mixed fiber material (*Pc*=10). In addition, the effective stress path tends to migrate to intercept the critical state line (CSL) obtained from the undrained monotonic test when increasing the number of cycles (see Figure 6-8 a).

The resulting stress-strain curves provided in a q-ε_a diagram in Figure 6-8 b) enclose a much larger area than typically observed for sand which means the material damping is much higher for the tested LSS. Furthermore, the strain accumulation in the sample is not symmetric in compression and extension. This behavior reflects the presence of an anisotropic fiber, and the response of LSS mixed fiber is stronger in compression and weaker in the extension loading mode, which induces all the cyclic tests conducted as a part of this study to fail in the extension mode. In some previous studies, this behavior is the same as that of soft soil subjected to cyclic loading.

The influence of cyclic deviator stress amplitude on the direction/orientation of effective stress paths in p – q plane is significant as shown in Figure 6-9. The higher in stress amplitude σ_d, the stress loop is closer to CSL and significantly incline to touches CSL line in the left upper corner of the p' – q diagram at the failure state. In the final stage, the stress loop highlighted in black color passes a "Butterfly" stress path shape. However, it does not reach $p' = q = 0$, and the distance of this final stress loop observed smaller than to origins of p' – q plane with the lower stress amplitude as seen in Figure 6-9 f).

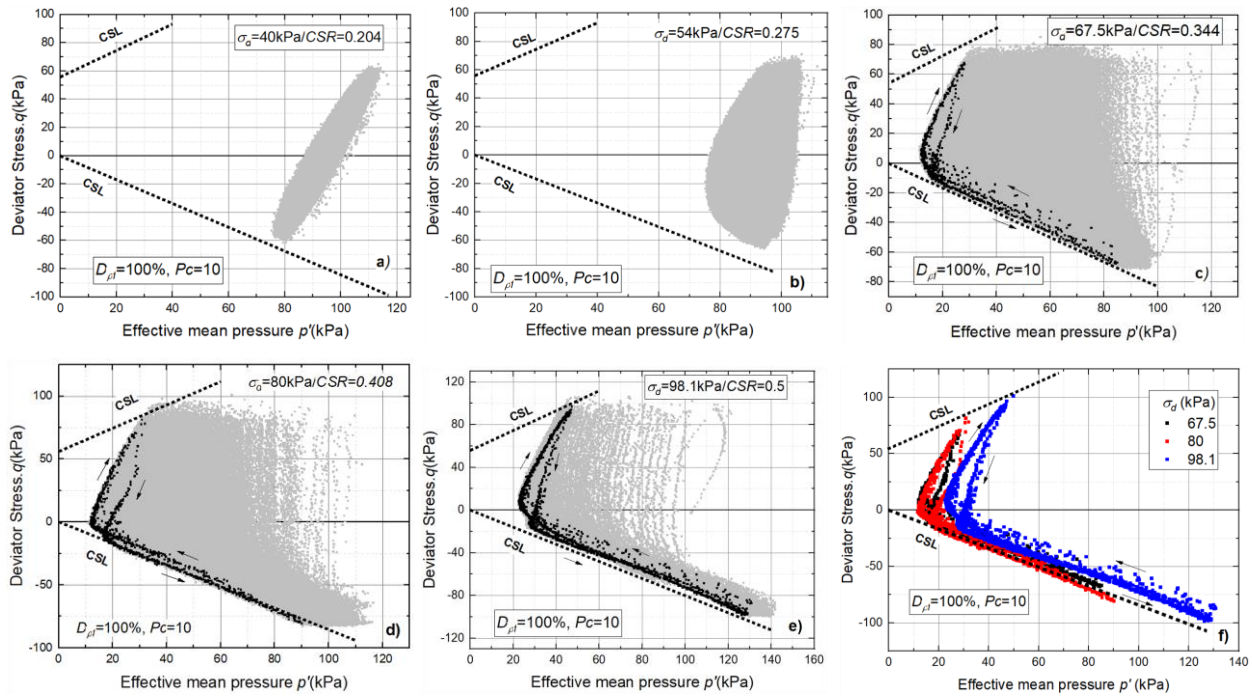

Figure 6-9 Summary of effective stress paths in the p - q plane in undrained cyclic tests C19 to C23 with different stress amplitudes; a) σ_d*=40 kPa,* b) σ_d*=54 kPa,* c) σ_d*=67.5 kPa,* d) σ_d*=80 kPa,* e) σ_d*=98.1 kPa,* f) The final effective stress paths.

Figure 6-10 a) shows graphs of pore water pressure ratio, $\Delta u'$, with the number of cycles. Value of $\Delta u'$shown represent the maximum value mobilized over the duration of an individual cycle. A ratio $\Delta u/\sigma'_c = 1$ corresponding to zero effective stress not been reached in this test on LSS mixed fiber material. The figure shows that the accumulation of excess pore water pressure and simultaneously the relaxion of effective stress run faster with increasing cyclic stress amplitude in reinforced LSS. In cases of the tests with cyclic stress amplitude higher than 54 kPa (*CSR* > 0.275), the pore water pressure curves present three very different accumulation rates. At the first cycle, a high rate of pore water pressure accumulation is observed about 20 %. Then, the accumulation rate decreases and gets almost constant between cycle 1 up to about $\Delta u'$ =40 ÷ 60 %, after which the rate of accumulation increases significantly to the failure criterion. In contrast, an inspection of tests undertaken at lower cyclic stress amplitude (σ_d < *54* kPa or *CSR*< 0.275) shows that the sample was able to withstand more than 10^4

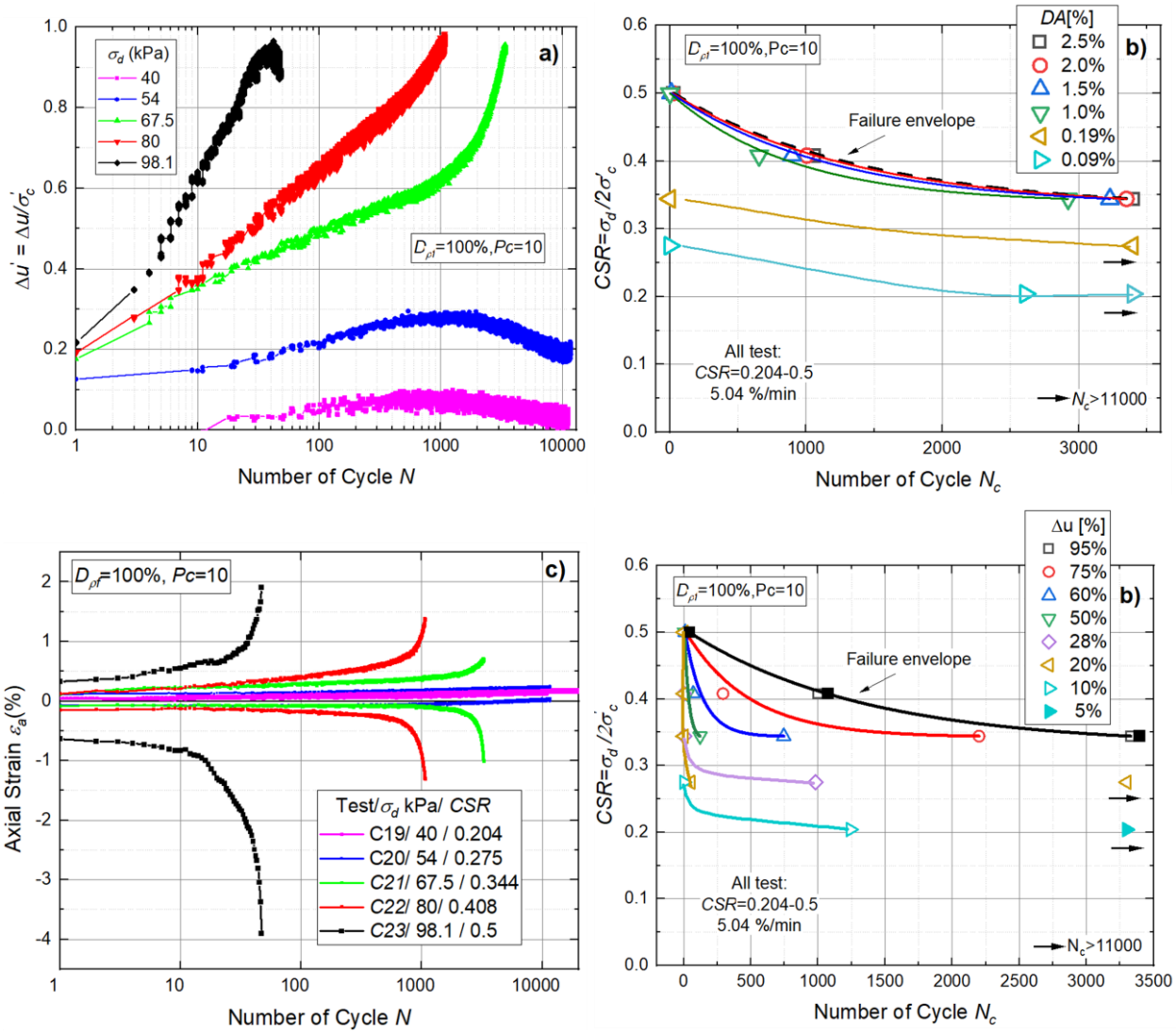

Figure 6-10 Summary of results from tests with different stress amplitudes at symmetrical loading (All tests with σ'_c = 98.1 kPa, σ_s = 0 kPa, η_0 = 0, $\dot{s} = 5.04\ \%/min$); a) Excess porewater pressure ratio against the number of cycle N, b) Cyclic cycle ratio CSR against the number of cycles for each excess pore water pressure ratio, c) Axial strain against the number of cycles, d) Cyclic stress ratio CSR against the number of cycles for each double axial strain.

cycles without mobilizing significant permanent axial strains or large double axial strain amplitude. After the $\Delta u'$value reaches the peak with a small value of about 10 % ÷ 20 %, the excess pore water pressure decreases and subsequent increases in effective stress. This is because adding fiber material into LSS cause the sample tend to dilate when sheared at a low cyclic stress ratio and subsequent stiffness increases.

Similar behavior trends of pore water pressures are observed above, indicating that the rate and magnitude of accumulated strains are closely related to the build-up of excess pore water pressures and a corresponding reduction in mean effective stress as shown in Figure 6-10 a)-c). The result showed that the axial strain accumulation increased gradually until reaching the stage where pore water pressures start to increase quickly, after that double strain amplitude (DA) grows quickly with each subsequent cycle and reached the defined failure criterion. The results also suggest that the axial strain accumulation is higher on the extension side than on the compression side. As shown in Figure 6-11, the accumulation of double axial strain amplitude is dominant at a high-stress ratio compared with a low-stress ratio, and there is a remarkable increase in the DA value with increasing deviatoric stress amplitude. The analysis of the cyclic stress ratio $CSR = \sigma_d / (2\sigma_c')$ against the number of cycles for each excess pore water pressure and the double axial strain amplitude observed in Figure 6-10 b)-d). It is found that the existence of threshold cyclic stress amplitude for LSS mixed fiber obtained from the figures, the threshold value varies from 0.275 to 0.344 of *CSR*. The test with cyclic deviatoric stress amplitude more than 0.275 of *CSR* is required to fail sample. In contrast, with CSR in test less than 0.275, the failure criterion was not achieved even with great amount of cycles was applied (>11000 cycle). The double axial strain amplitude (DA) was only reached at relatively small value of 0.19 % and 20% of the pore water pressure ratio ($\Delta u'$), whereas the failure threshold required 2.5 % of DA and more than 95 % of $\Delta u'$. Figure 6-10 b)-d) also shows the envelope failure for the two aspects of double axial strain amplitude and excess pore water pressure.

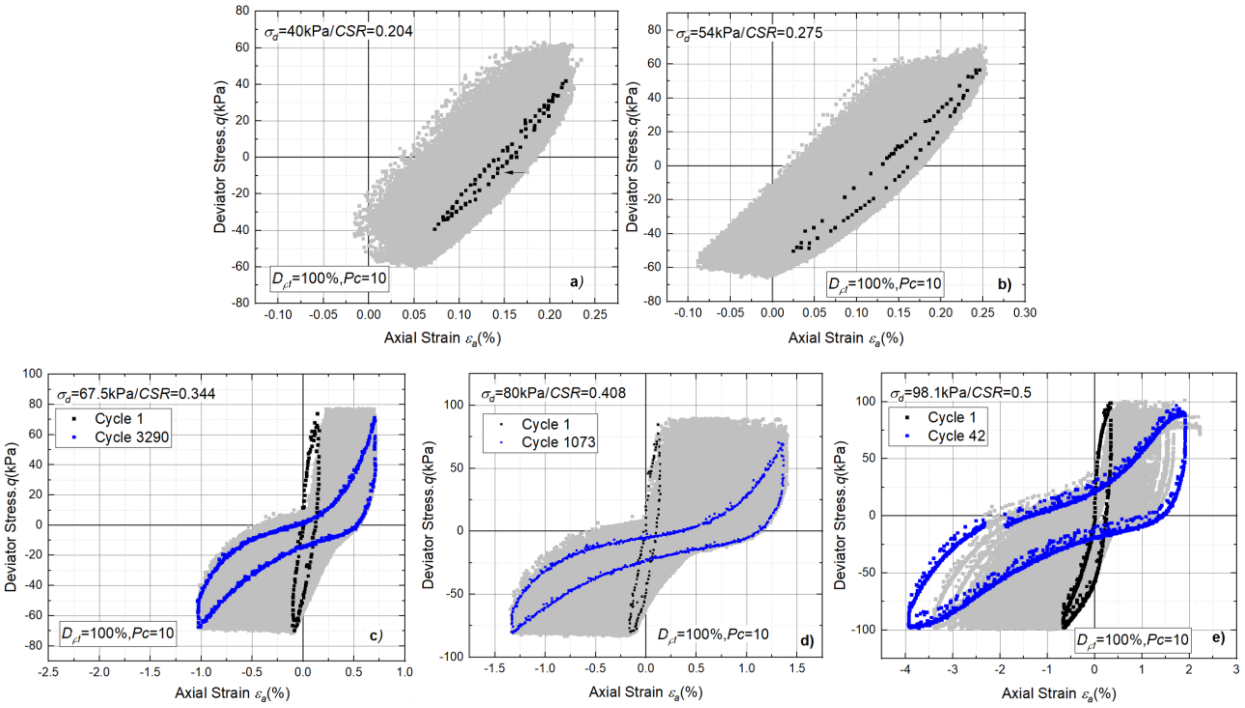

Figure 6-11 Summary of results from tests with different stress amplitudes at symmetrical loading (All tests with σ_c' = 98.1 kPa, σ_s = 0 kPa, η_0 = 0, $\dot{s} = 5.04\ \%/min$); $q - \varepsilon_1$ space.

This envelope predicts when LSS samples failure with a certain cycle and CSR value. The results suggest a remarkable reduction in N_f with increasing *CSR*. The failure envelope was well described (R^2 =0.96) by a potential function in the form $CSR = aN_f^b$, with a = 0.6453, b = 0.073 for DA, and a = 0.6799, b = 0.08 for excess pore water pressure.

6.5.2. Variation of Initial Stress σ_s (nonsymmetrical cyclic loading)

Five undrained cyclic triaxial tests C30 to C35 on LSS (P_c=10) with different initial stress σ_s between 27 kPa and 64 kPa ($0.28 \leq \eta_0 = {}^{\sigma_s}/_{\sigma_c'} \leq 0.65$) were conducted to analyze the behavior on LSS mixed fiber with initial stress (nonsymmetric cyclic loading). The samples were consolidated at σ_c' = 98.1 kPa. The stress amplitude was σ_d =54 kPa and the displacement rate was $\dot{s} = 5.04\ \%/min$ in all tests. A typical result is given in Figures 6-12 for illustration purposes.

The accumulation of double axial strain seems to be predominant in LSS subjected to symmetrical cyclic loading, as shown in section 6.5.1. However, permanent axial strain (ε_p) accumulation prevailed in nonsymmetrical cyclic loading (one-way loading) tests. The results shown in Figure 6-12 reveal that the accumulation rate of permanent axial strain increased with increasing numbers of cycles, while mobilized double

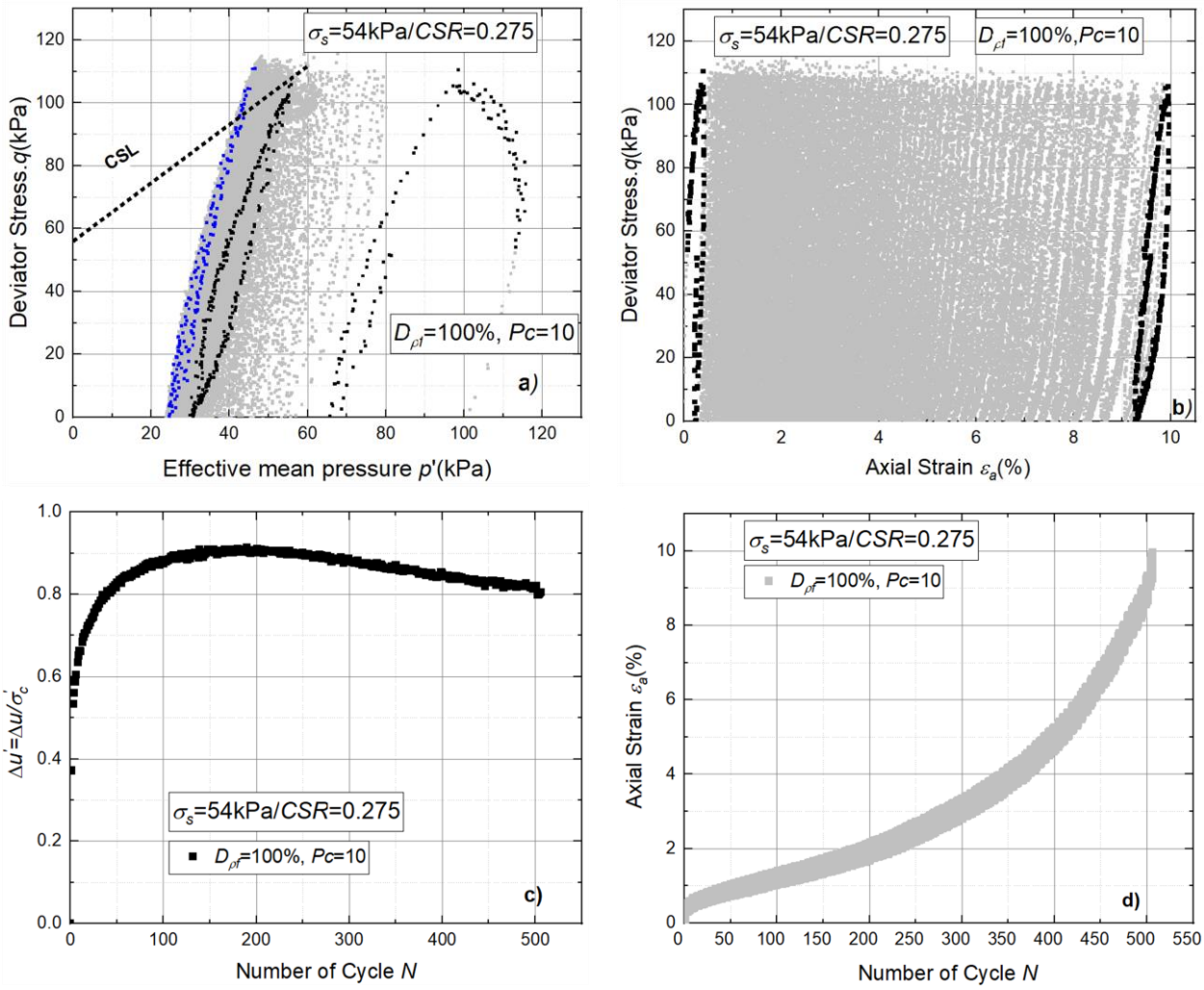

Figure 6-12 Typical result of an undrained cyclic triaxial test (C33) with initial stress σ_s=*54* kPa and constant deviator stress amplitude σ_d =54; a) *p'- q* space; b) *q*-ε_a relationship; c) $\Delta u'$ against with N; d) ε_a-*N* relationship.

axial strain remained almost constant (Figure 6-12 b)). The rate of normalized accumulated excess pore water pressure increases significantly in the first cycle; then, it is relatively linear between cycle one up to the maximum value. Nevertheless, in contrast to the symmetrical loading case, the excess pore water pressure decreases quickly to failure, as shown in Figure 6-12 c). The experimental result also suggests that the axial strain progressively grows in each subsequent cycle to the defined failure criterion while pore water pressure accumulation decreases after reaching the maximum value. The failure criterion ε_a = 10 % was reached from the tests with nonsymmetrical cyclic loading due to excessive permanent axial strain and not too large strain amplitude.

The mean effective stress shown in Figure 6-12 a) decreases, and its loop migrates to pass over the compression CSL line with increasing cycles due to the increase in pore water pressure. After reaching the maximum pore water pressure value, effective stress increasing is observed, and the effective stress paths go far away from the origin to touch the failure criterion. The stress loop at the maximum value of pore water pressure is highlighted in blue color, the first and the final stress loop at failure is highlighted in black color, and the rest of the paths are formatted in grey. From this result, by adding fiber material, LSS tends to dilate, and subsequent stiffness increases resulting from the increased mean effective stress when applying nonsymmetrical cyclic loading. The improvement of the brittle property of LSS mixed fiber material to prevent cyclic loading observed from the monotonic test as mentioned in section 5 was verified in these tests.

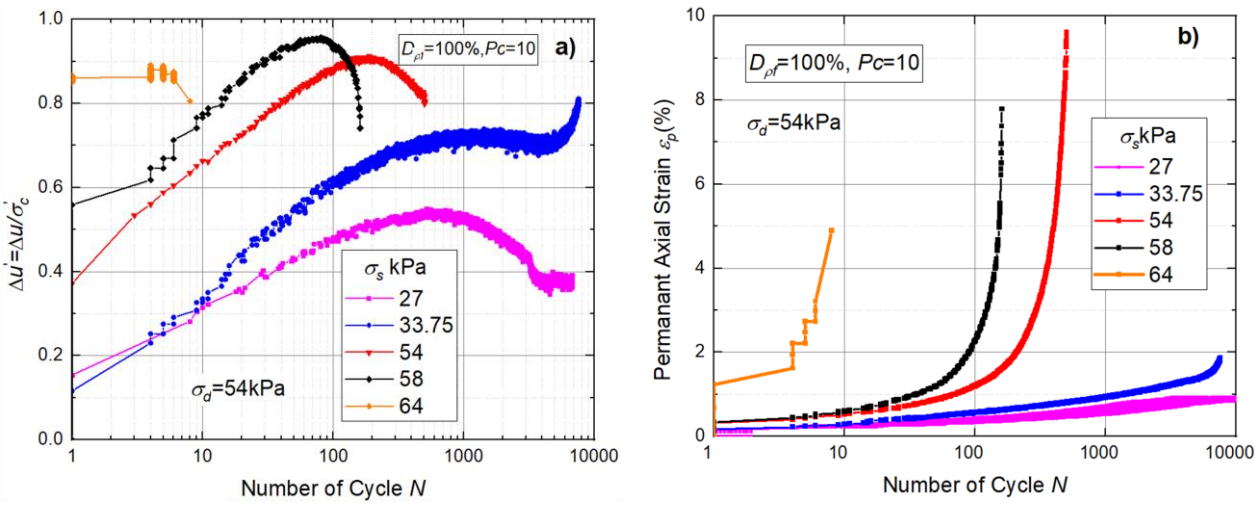

Figure 6-13 Summary of undrained triaxial test result C30-C35 with various initial stress σ_s; a) Normalized accumulation of pore water pressure against a number of cycles *N*; b) Accumulation of permanent axial strain against a number of cycles *N*

The results of undrained cyclic triaxial tests C30 to C35 with various initial stress σ_s = {27, 33.75, 54, 58, 64} were summarized in Figure 6-13, Figure 6-14 and Figure 6-15. The result suggests that there is a remarkable influence of initial stress on the LSS behavior subjected to cyclic loading. Increasing the magnitude of the initial stress σ_s or initial stress ratio $\eta_0 = {}^{\sigma_s}/_{\sigma_c'}$, remarkably reduces the number of cycles to reach the failure criterion N_f as shown in Figure 6-13. The rate at which excess pore water pressures develop is shown to be influenced by the value of η_0, with higher values leading to faster accumulation rates. This is exemplified in tests C32 to C34, which shows that σ_s ≥ 54 kPa (η_0 ≥ 0.55), the failure criterion of 10 % permanent axial strain is reached after

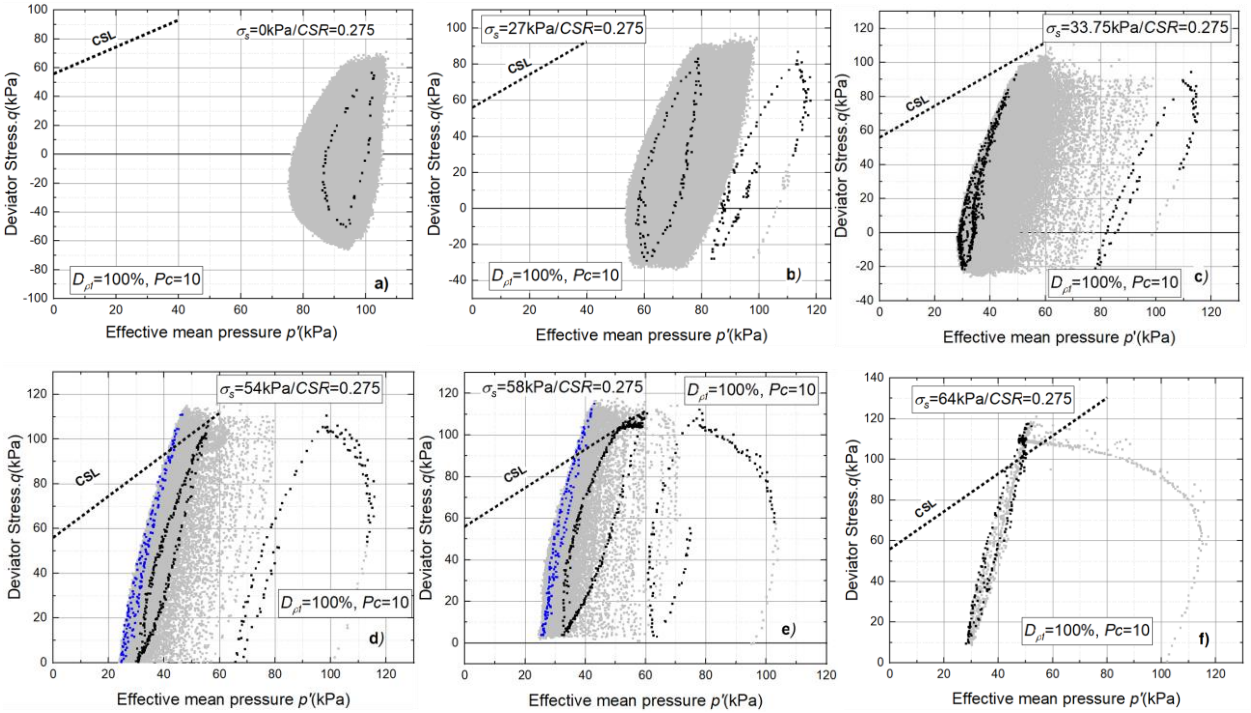

Figure 6-14 Effective stress paths in the *p*-*q* space measure in tests with different initial stress; a) σ_s = 0 kPa, b) σ_s = 27 kPa, c) σ_s = 33.75 kPa, d) σ_s = 54 kPa, e) σ_s = 58 kPa, f) σ_s = 64 kPa,

less than 160 cycles. However, in tests C30 and C31 undertaken at $\sigma_s \leq 33.75$ kPa ($\eta_0 \leq 0.34$), the failure criterion did not reach after 10^4 cycles, especially, the test with C30 at $\sigma_s \leq 27$ kPa ($\eta_0 \leq 0.28$) shows the steady accumulation of approximately 1 % of permanent axial strain after 10^4 cycles and the cyclic stress path remains relatively far away from CSL resulting from the increasing mean effective stress after dilation.

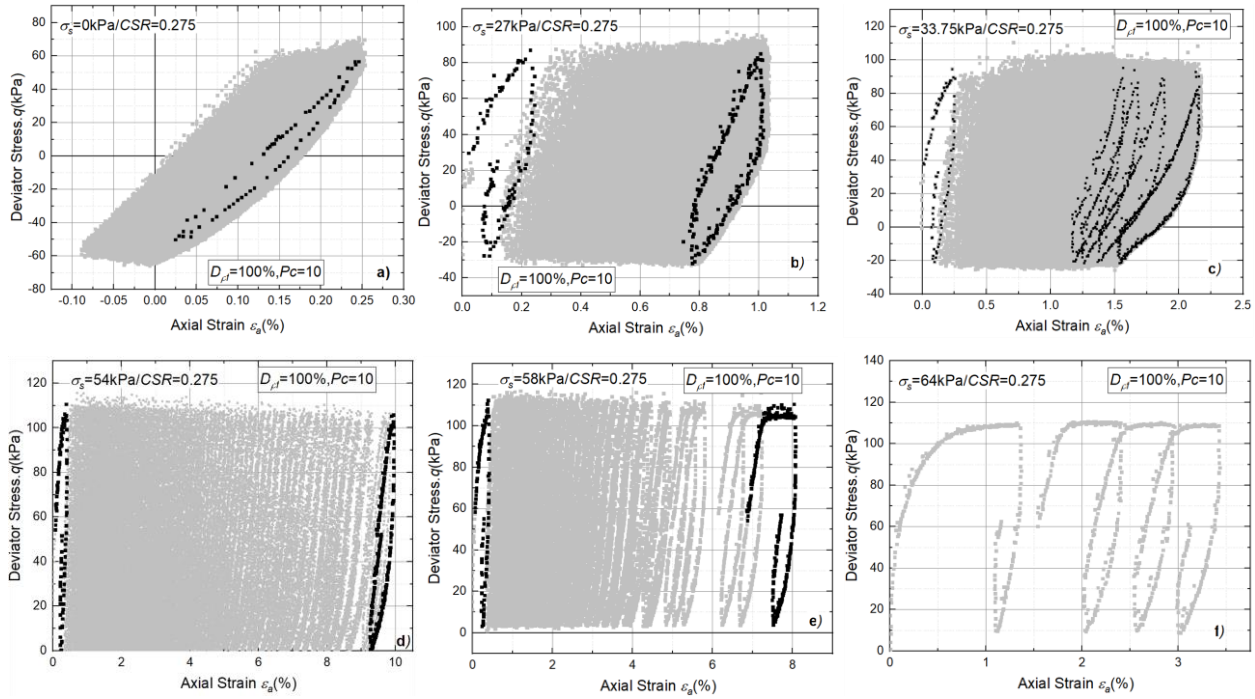

Figure 6-15 Relationship between cyclic deviator stress and axial strain for a) symmetrical cyclic loading σ_s = 0, b) σ_s = 27 kPa, c) σ_s = 33.75 kPa, d) σ_s = 54 kPa, e) σ_s = 58 kPa, f) σ_s = 64 kPa.

Figure 6-14 shows that the cyclic effective stress paths migrate closer to the failure envelope, and the shape of the stress loop at the final stage did not pass the "butterfly" shape or lens shape that is the same as two-way loading when increasing initial stress σ_s. In contrast to symmetrical loading with no initial stress, the orientation/direction of the stress path means that the extension failure envelope will be intercepted at a lower magnitude of stress than in compression. This type of behavior is evident in Figure 6-9, which shows the stress path intercepting the extension dilatancy surface during the unloading component of cycle 0. Therefore, increasing initial stress can improve the resistance of the material, by 'shifting' the stress path up in p'– q space, and thus further away from the extension failure envelope. As the result the cyclic resistance of LSS mixed fiber increase significantly when increasing initial stress σ_s.

Typical result demonstrating the relationship between cyclic deviator stress and axial strain are presented in Figure 6-15. In case of the symmetrical loading (two-way) significant magnitude of strain amplitude developed near the failure stage of cyclic loadings while in the nonsymmetrical loading (one-way), the permanent strain was predominant instead of cyclic component. Furthermore, it should be noted that increase in the permanent strain of LSS during a cycle was triggered at final stage of cycling when the stress paths approached the critical state line.

6.5.3. Variation of Initial Mean Pressure σ_c'

The influence of initial mean pressure σ_c' on cyclic behavior of LSS mixed fiber was investigated with the cyclic tests under isotropic consolidation at 58.8 kPa, 98.1 kPa, and 196 kPa (test C22, C24 and C25 in table 6-2). All the samples were subjected to a symmetrical cyclic loading (two-way) with stress amplitude σ_d = 80 kPa and a displacement rate $\dot{s} = 0.504\ \%/min$. The result of the accumulation of excess pore water pressure and the axial strain were summarized in Figure 6-16. It was found that the rate of accumulation of excess pore water pressure ratio increases quickly with increasing number of cycles when the decrease of initial mean pressure σ_c'. Tests undertaken at initial mean pressure σ_c' = 58.8 kPa and σ_c' = 98.1 kPa show the high rate of pore water pressure accumulation to the failure. However, the highest rate was observed at the lowest isotropic consolidation pressure, σ_c' = 58.8 kPa. In contrast, the tests at σ_c' = 196 kPa, the mobilized pore water pressure rate showed a significant increase before reaching stable at about 44 % of $\Delta u'$, after which there was a light decrease in pore water pressure after 4000 cycles and did not achieve failure. The excess pore water pressure behavior causes to reduce significantly effective stress in LSS; therefore, the cyclic effective stress paths move quickly to the compression critical state line, as shown in Figure 6-17 when reducing confining pressure. However, since the increase in effective stress after 1000 cycles was found due to the dilatation behavior of LSS mixed fiber, the

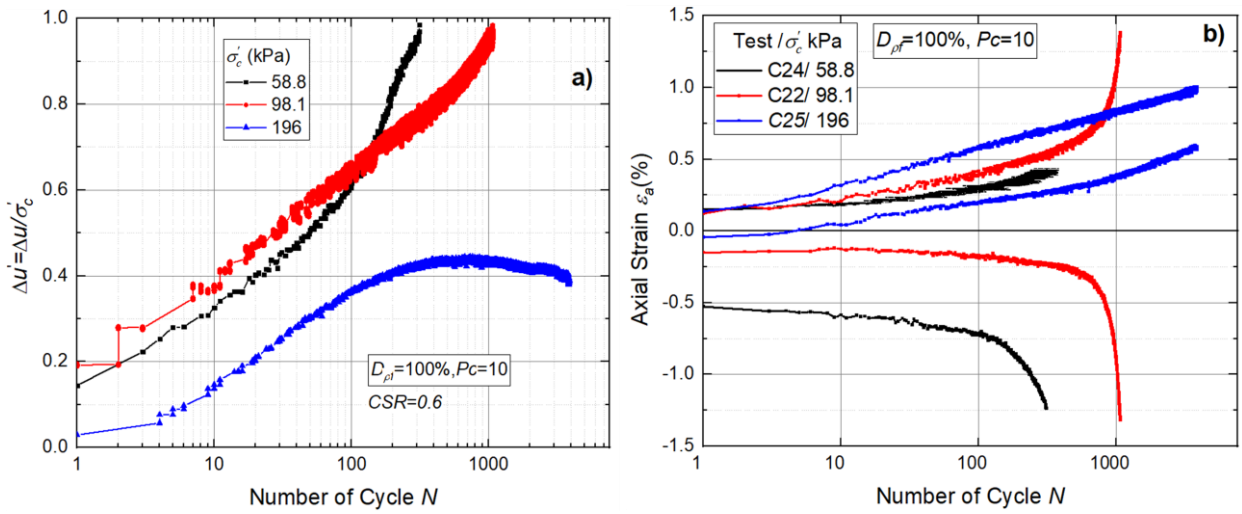

Figure 6-16 Summary of undrained triaxial test results with various mean initial stress σ_c'; a) Normalized accumulation of pore water pressure against a number of cycles *N*; b) Accumulation of permanent axial strain against a number of cycles *N*. (all tests in symmetrical cyclic loading, $\dot{s} = 5.04\ \%/min$)

effective stress paths tend to move further away from the origin and are more compressive at initial mean pressure σ_c' = 196 kPa. This behavior is similar to LSS behavior under low-stress amplitude, low initial stress ratio, and cyclic symmetrical and nonsymmetrical loading, respectively. The first and last stress loops were highlighted in black, while the rest paths were highlighted in grey as shown in Figure 6-17.

The relationship between deviator stress and axial strain is shown in the figure 6-18, and Figure 6-16 b) presents a summary of the axial strain accumulation results with number of cycles. Based on the test results, the axial strain amplitude was accumulated at σ_c' = 58.8 kPa and σ_c' = 98.1 kPa, and the LSS sample failed suddenly with rapidly increasing axial strain in the extension mode, causing significant necking to appear on one-third of the sample when the excess pore water pressure was greater than 95 % as shown in Figure 6-19. In contrast, the

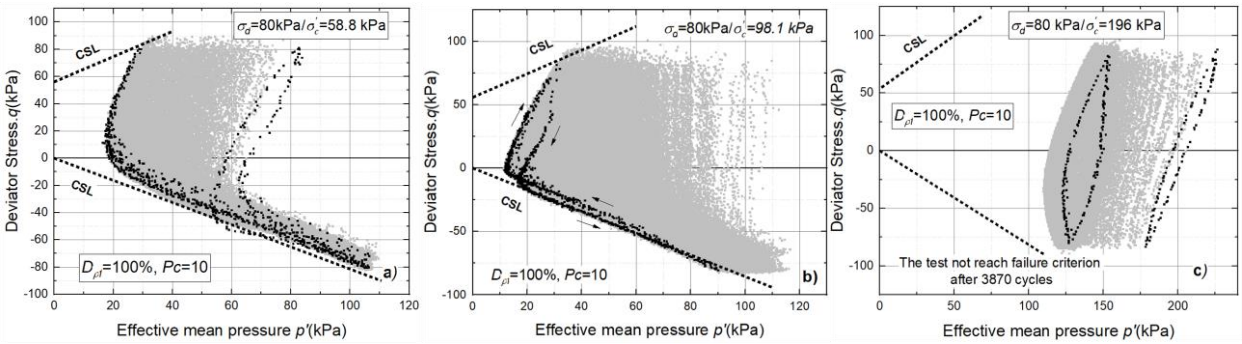

Figure 6-17 Effective stress paths in the p'–q plane measured in tests with different initial mean pressures σ_c'; a) C24 test with σ_c' = 58.8 kPa, a) C24 test with σ_c' = 58.8 kPa, b) C22 test with σ_c' = 98.1 kPa, c) C25 test with σ_c' = 196 kPa. (all tests in symmetrical cyclic loading, $\dot{s} = 5.04\ \%/min$)

permanent axial strain accumulation with the negligible mobilized double axial strain accumulation was found at test with σ_c' = 196 kPa.

In conclusion, increasing initial mean pressures σ_c' leads to increasing cyclic resistance. In contrast, reducing the initial mean pressure significantly decreases the number of cycles N_f required to reach the failure criterion, with 1075 cycles required for the test at σ_c' = 98.1 kPa and 314 cycles required for the test at σ_c' = 58.8 kPa, respectively.

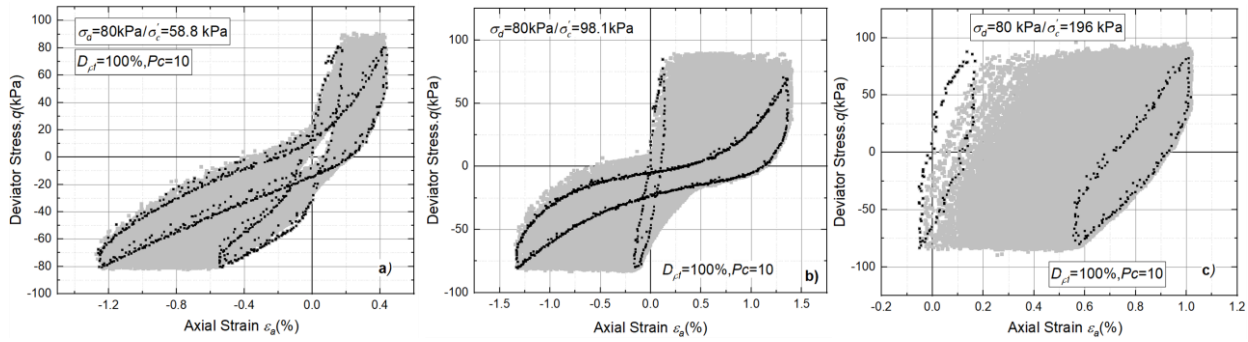

Figure 6-18 The relationship between cyclic deviator stress and axial strain of undrained cyclic triaxial test with different initial mean pressure σ_c'; a) C24 test with σ_c' = 58.8 kPa, a) C24 test with σ_c' = 58.8 kPa, b) C22 test with σ_c' = 98.1 kPa, c) C25 test with σ_c' = 196 kPa. (all tests in symmetrical cyclic loading, $\dot{s} = 5.04\ \%/min$)

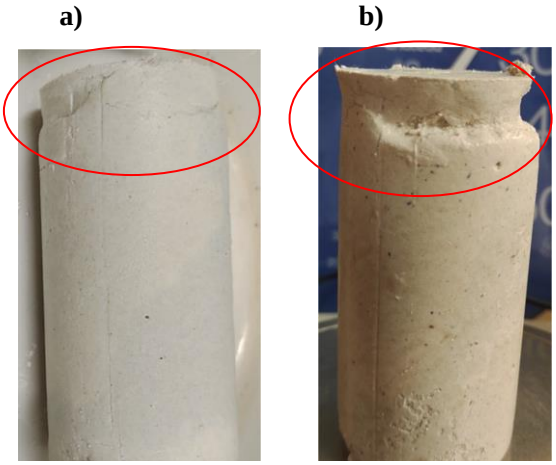

Figure 6-19 The cyclic loading failure mode of LSS; a) The sample of test at σ_c' = 98.1 kPa, b) The sample of test at σ_c' = 98.1 kPa,

6.5.4. Variation of Displacement Rate

The undrained cyclic triaxial test with different displacement rate, $\dot{s} = 2.04\ \%/min$, $\dot{s} = 5.04\ \%/min$, respectively, has been performed to inspect the effect of displacement on LSS mixed fiber (*Pc=10*). All test was isotropically consolidated at σ_c' = 98.1 kPa and under cyclic stress amplitude σ_d = 80 kPa (*CSR* = 0.408).

The test results were presented in Figures 6-20, 6-21, and 6-22. It was found that the accumulation rate of pore water pressure in the test at a low displacement rate is higher in comparison to the test with a high displacement rate at the first cycle, as shown in Figure 6-20 a). However, after the first cycle, the accumulation rate seems lower than the rate in the test with a high displacement rate. Especially with a low displacement rate $\dot{s} = 2.04\ \%/min$, the failure criterion was reached in a lower number of cycles required to the failure than in the test with $\dot{s} = 5.04\ \%/min$, 399 cycles required to failure for the case of a low displacement rate and 1075 cycles for the case of a high displacement rate, respectively. It means that the effective stress paths in the test with $\dot{s} = 2.04\ \%/min$ tend to migrate early to CSL and the last stress loop that highlighted in black color shown in Figure 6-21 further away from to origin than in case of test with $\dot{s} = 5.04\ \%/min$. This behavior of LSS was explained in that under a lower displacement rate, the strength of the sample reduces more quickly than under a higher displacement rate with each subsequent cycle. The stress strain becomes more nonsymmetrical and tends to enlarge in compression mode, revealing that the compression strength is weaker than when applying a cyclic test with a low displacement rate. In agreement with the tendency in this behavior of LSS, most of the experimental investigations on cohesive soils in the literature found the level of stiffness degradation is high for low loading frequencies; for higher frequencies, the level of degradation will be lower.

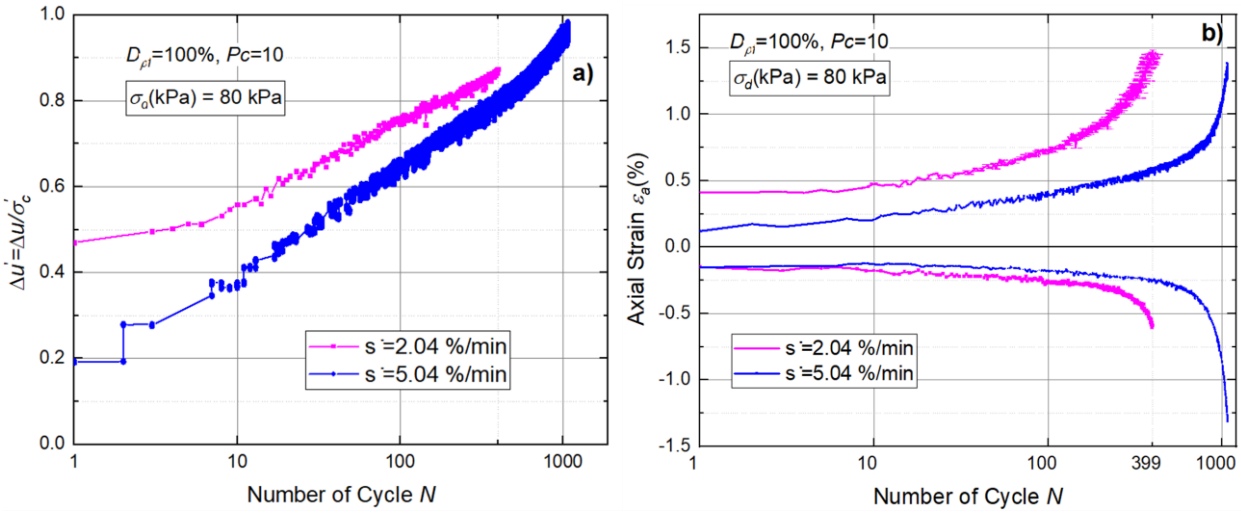

Figure 6-20 Comparison of accumulated pore water pressure and axial strain in LSS (*Pc=10*) at *CSR* =0.408 with different displacement rate; a) $\dot{s} = 2.04\ \%/min$, b) $\dot{s} = 5.04\ \%/min$

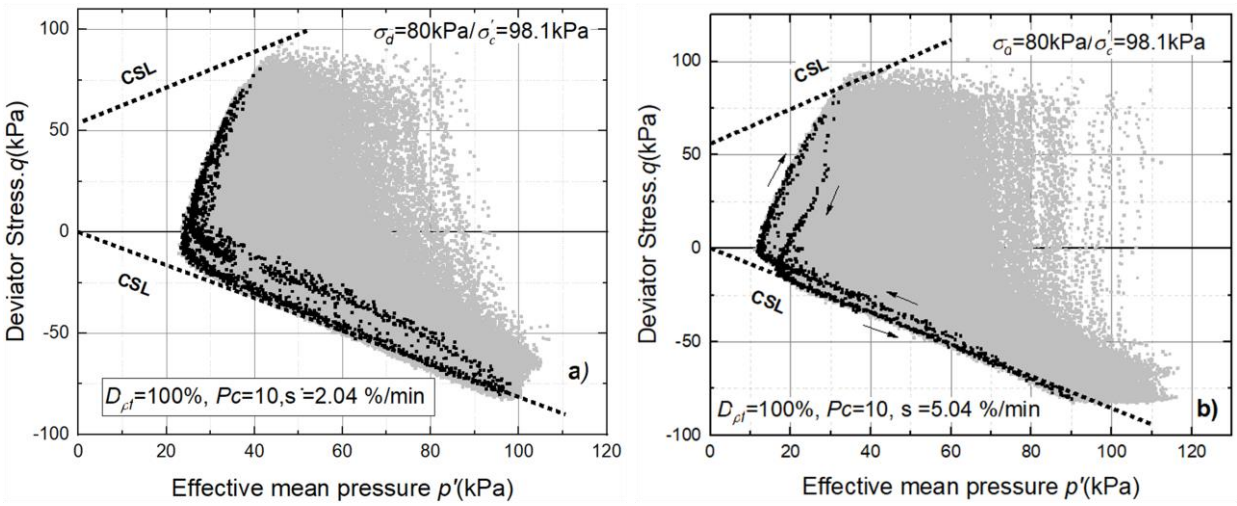

Figure 6-21 Effective stress paths in the *p'* - *q* plane in cyclic test on LSS mixed fiber at *CSR* = 0.408 with different displacement rate; a) $\dot{s} = 2.04\ \%/min$, b) $\dot{s} = 5.04\ \%/min$

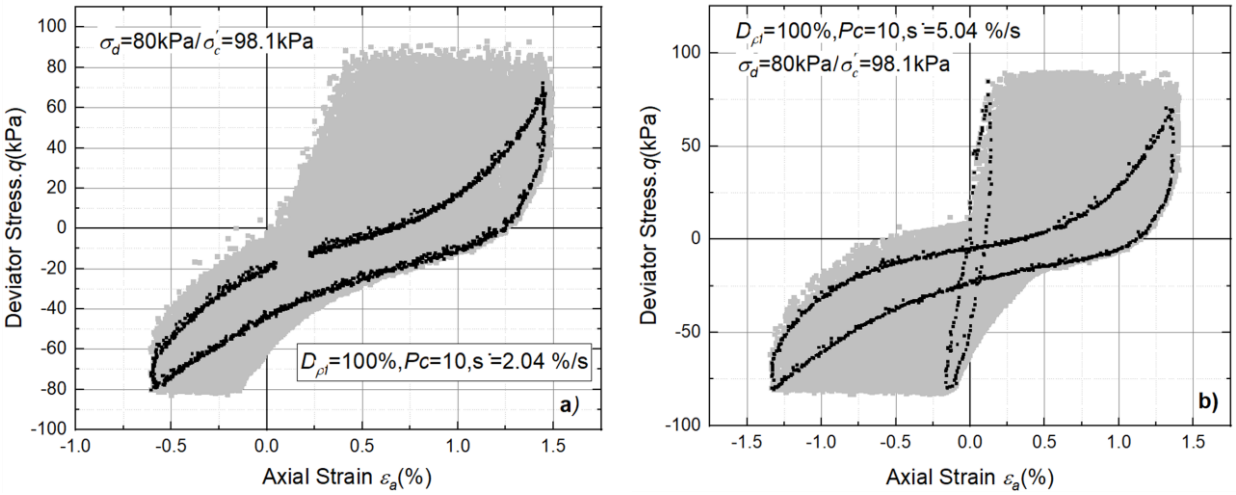

Figure 6-22 The stress-strain behavior in cyclic test on LSS mixed fiber at *CSR* = 0.408 with different displacement rate; a) $\dot{s} = 2.04\ \%/min$, b) $\dot{s} = 5.04\ \%/min$

6.5.5. Tests with Strain-controlled Cyclic Loading

The effect of strain cycles has been examined in two undrained strain-controlled cyclic triaxial tests (C40-41).

All test was isotropically consolidated at σ_c' = 98.1 kPa and under cyclic strain amplitudes ε_{ampl} = ε_{static} = 1.35 % and ε_{ampl} =2* ε_{static} = 2.7 %.

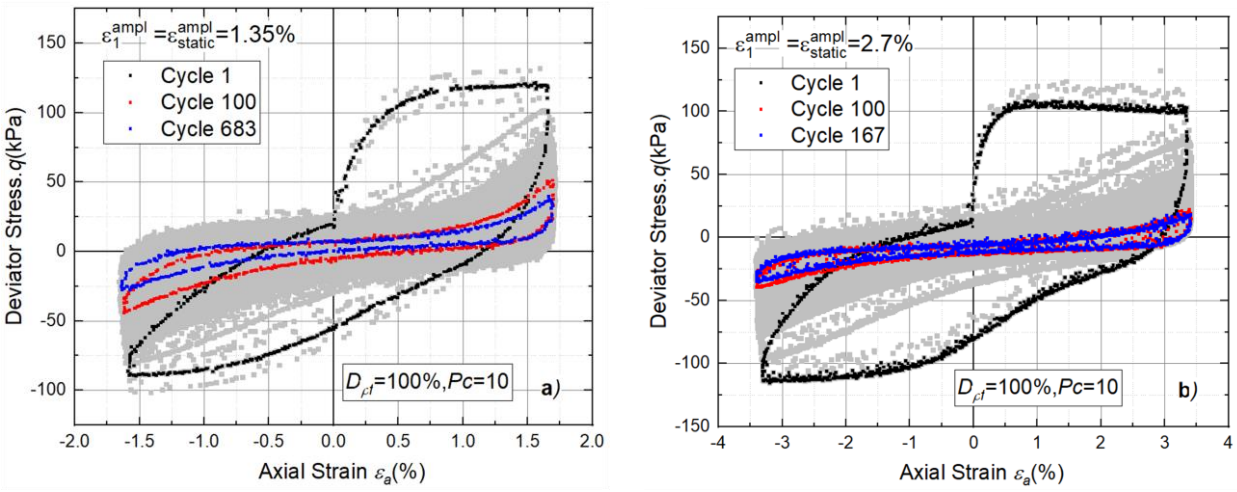

Figure 6-23 The stress-strain behavior in strain-controlled cyclic test on LSS mixed fiber; a) Axial strain amplitude $\varepsilon_1^{ampl} = \varepsilon_{static}^{ampl}$=1.35 % , a) Axial strain amplitude $\varepsilon_1^{ampl} = 2 * \varepsilon_{static}^{ampl}$=2.7 %.

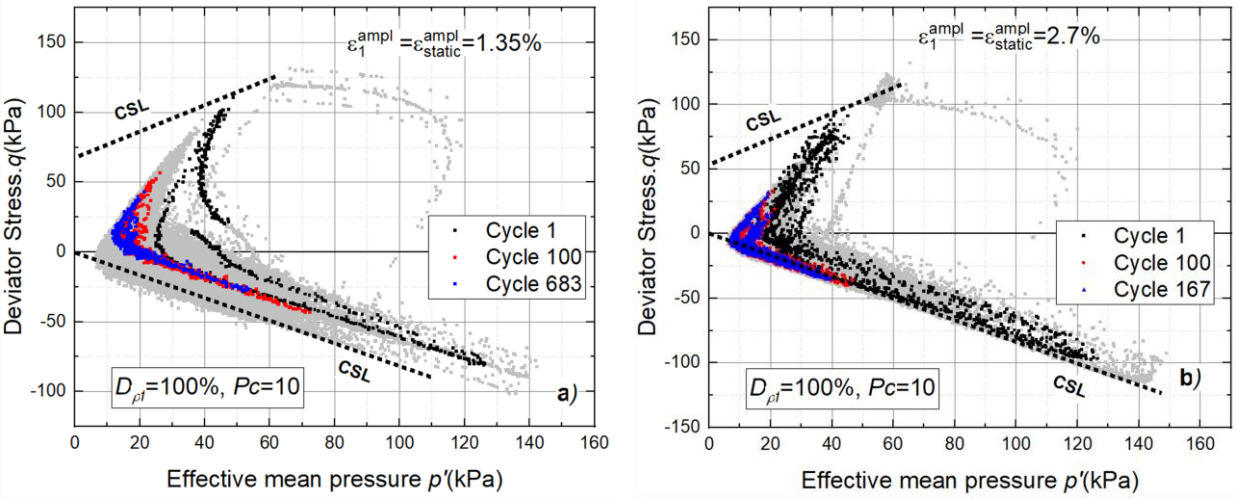

Figure 6-24 Effective stress paths in the p-q plane in strain-controlled cyclic test on LSS mixed fiber; a) Axial strain amplitude $\varepsilon_1^{ampl} = \varepsilon_{static}^{ampl}$=1.35 % , b) Axial strain amplitude $\varepsilon_1^{ampl} = 2 * \varepsilon_{static}^{ampl}$=2.7 %.

The strain-controlled cyclic test results are shown in Figures 6-23, 6-24, and 6-25. All tests show that the deviator stress decreases suddenly after the first cycle in strain-controlled cyclic tests. The effective stress paths move to the CSL and exhibit a “fir tree” shape similar to those observed in tests on the sand. However, the state with zero effective deviator stress has not been passed in LSS mixed fiber, as shown in Figure 6-24. The *p - N* curve shown in Figure 6-25 shows that the average mean pressure p_{av} reduces rapidly until about cycle 100, then decreases slightly at the end of the test, and an asymptotic p_{av} value has not been reached with the applied number

of cycles. However, the descending tendency in mean effective pressure and the number to reach a certain asymptotic value will increase with increasing the cyclic strain amplitude.

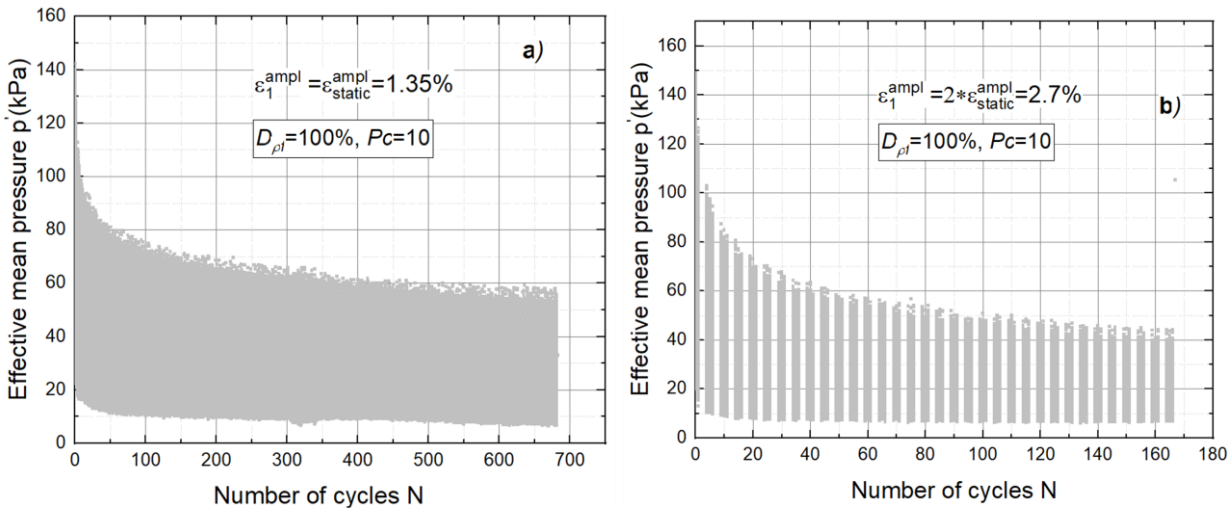

Figure 6-25 Relaxation of average mean pressure p^{av} with increasing number of cycles in tests with strain cycles of different amplitude; a) $\varepsilon_1^{ampl} = \varepsilon_{static}^{ampl}$=1.35 % , b) $\varepsilon_1^{ampl} = 2 * \varepsilon_{static}^{ampl}$=2.7 %.

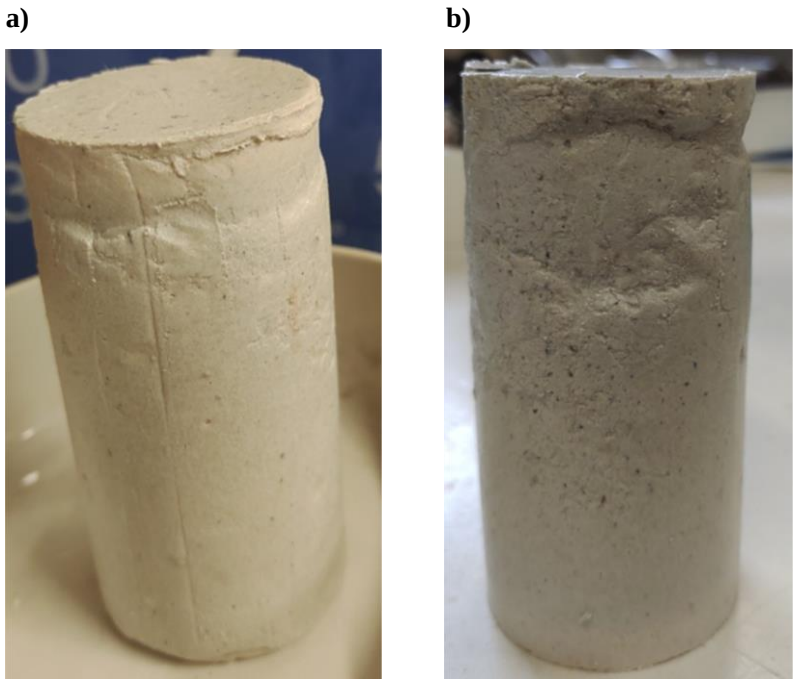

Figure 6-26 The state of LSS mixed fiber at the end of test; a) $\varepsilon_1^{ampl} = \varepsilon_{static}^{ampl}$=1.35 %, b) $\varepsilon_1^{ampl} = 2 * \varepsilon_{static}^{ampl}$=2.7 %.

6.5.6. The Effect of Fiber Material on LSS under Cyclic Loading

Five undrained cyclic triaxial tests C08-C12 on the LSS at standard slurry density ($D_{\rho f}$ = 100 %) without fiber material (Pc = 0) were performed with isotropic consolidation (σ_c' = 98.1 kPa, σ_s = 0 kPa, η_0 = 0) and variation of the deviator stress amplitude 40 kPa ≤ σ_d ≤ 80 kPa (0.204 ≤ CSR ≤ 0.408) to investigate the influence of adding fiber into LSS under cyclic loading. The cyclic loading was applied with a displacement rate $\dot{s} = 5.04\ \%/min$.

A typical result on LSS without fiber (Pc = 0) with deviator stress amplitude of σ_d = 67.5 kPa C10 is given in figure 6-27. The result shows the true liquefaction ($p' = q = 0$) also is not occur on the LSS without fiber (Pc = 0). In contrast to the case of LSS with fiber (Pc = 10), stress-strain cyclic behavior is nonsymmetrical and tends to be larger than in compression mode. It means the compression strength of LSS without fiber (Pc = 0) is weaker than in the case of LSS mixed fiber (Pc = 10).

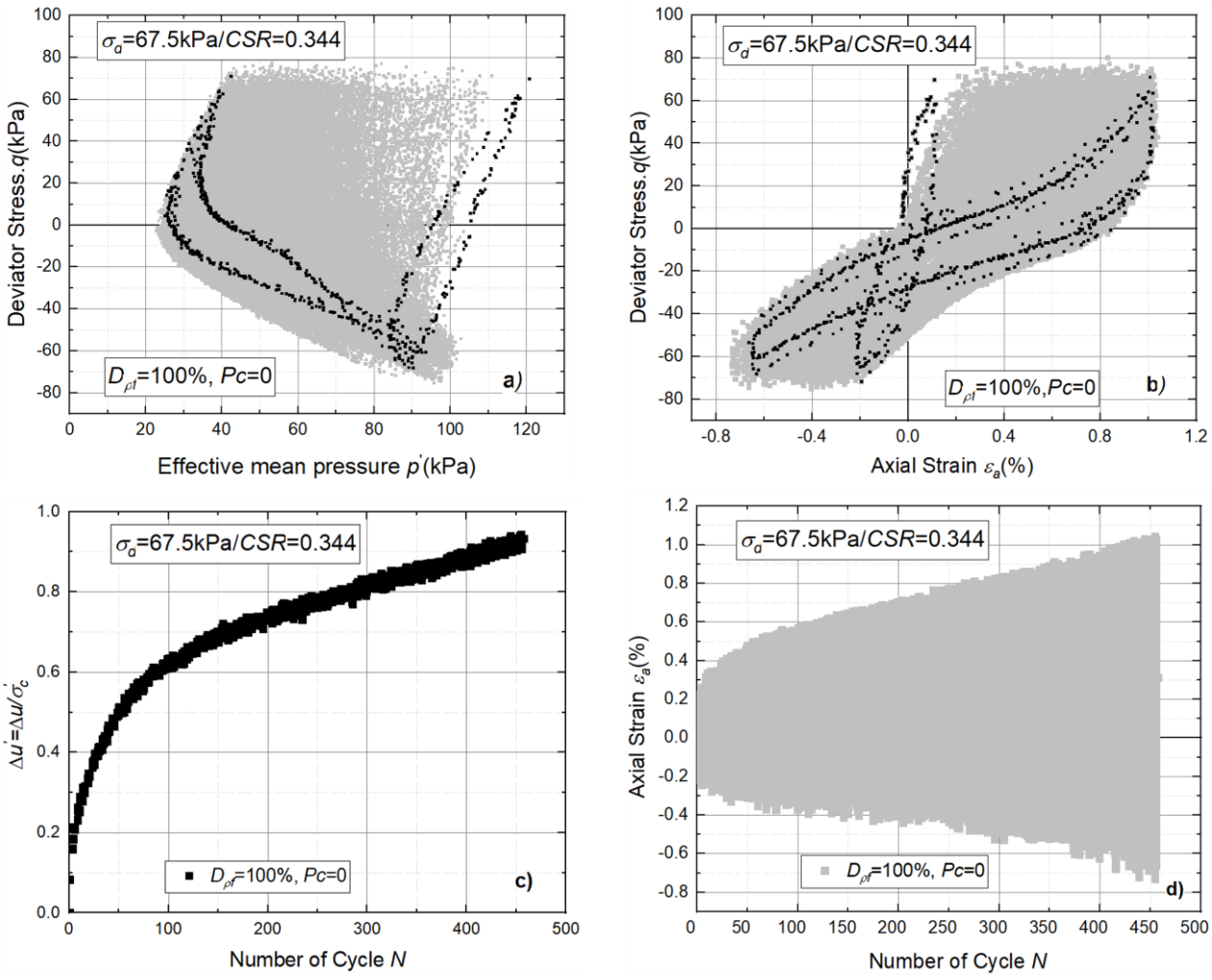

Figure 6-27 Typical results of an undrained cyclic test on LSS without fiber (P_c = 0) with σ_d = *67.5* kPa (test C10), σ_c' = 98.1 kPa, σ_s = 0 kPa, η_0 = 0, $\dot{s} = 5.04\ \%/min$); a) Effective stress paths, b) Deviator stress q versus axial strain εa, c) Porewater pressure ratio versus number cycle N, d) Axial strain versus number cycle N.

The effect of cyclic stress ratio *CSR* or cyclic stress amplitude on the accumulated pore water pressure and axial strain in LSS without fiber (*Pc* = 0) was presented in Figure 6-28. The pore water pressure, and axial strain increases with increasing *CSR* at the same number of cycles.

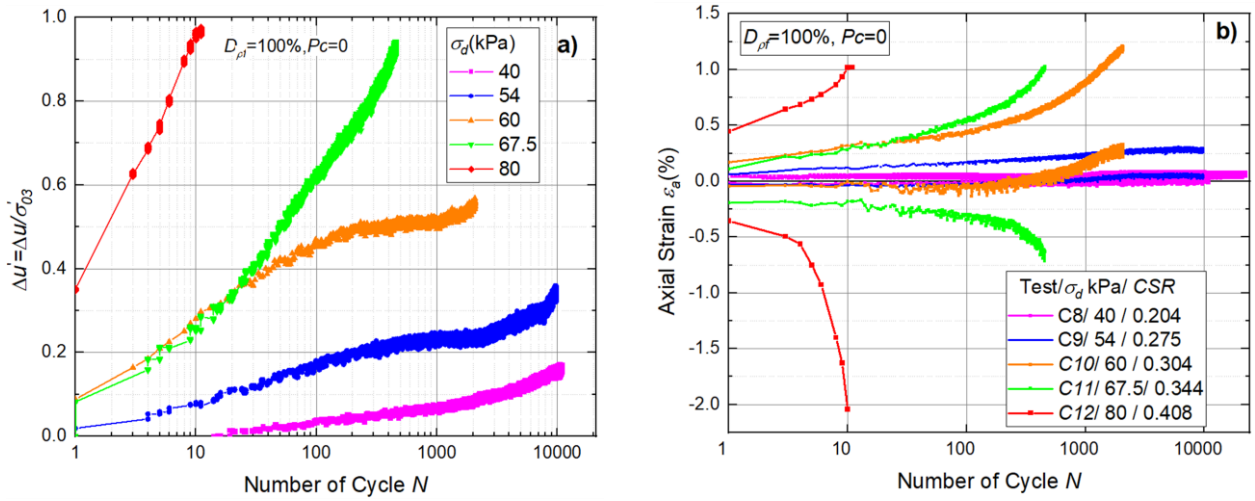

Figure 6-28 Summary of results from tests on LSS (*Pc = 0*) with different stress amplitudes (All tests with σ'_c = 98.1 kPa, σ_s = 0 kPa, η_0 = 0, $\dot{s} = 5.04\ \%/min$); a) Excess porewater pressure ratio against the number of cycle *N*, b) Axial strain against the number of cycles.

In terms of accumulated excess pore water pressure and mobilized axial strain, these are the most important results or observations of applying cyclic load on LSS. The comparison of reinforced (*Pc* = 10) and unreinforced LSS (*Pc* = 0) test results at each *CSR* are given respectively in Figure 6-29, Figure 6-30, and Figure 6-31.

The result is clearly shown that adding fiber improves significantly the cyclic shear strength. The increment in shear strength makes the LSS mixed fiber more resistant against to deformation.

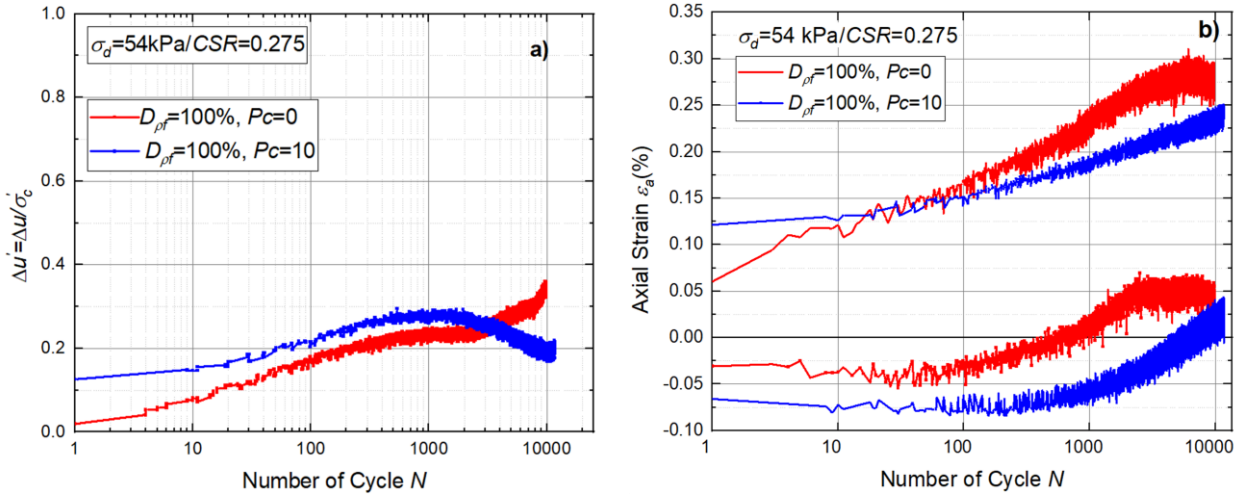

Figure 6-29 Comparison of accumulated pore water pressure and axial strain in unreinforced (*Pc* = 0) and fiber-reinforced LSS at *CSR* =0.275 (All tests with σ'_c = 98.1 kPa, σ_s = 0 kPa, η_0 = 0, $\dot{s} = 5.04\ \%/min$)

Inspection of the cyclic test at a low cyclic stress ratio *CSR* = 0.275 shows that the excess pore water pressure continuously increases with each subsequent cycle in LSS without fiber (*Pc* = 0). In contrast, the negative pore water pressure was observed in LSS mixed fiber (*Pc* = 10) after 1000 cycles cause by the dilation phenomenon as shown in Figure 6-29. The permanent axial strain was accumulated and larger than in case of LSS without fiber. As a result, the shear strength and stiffness increase in LSS when adding fiber material.

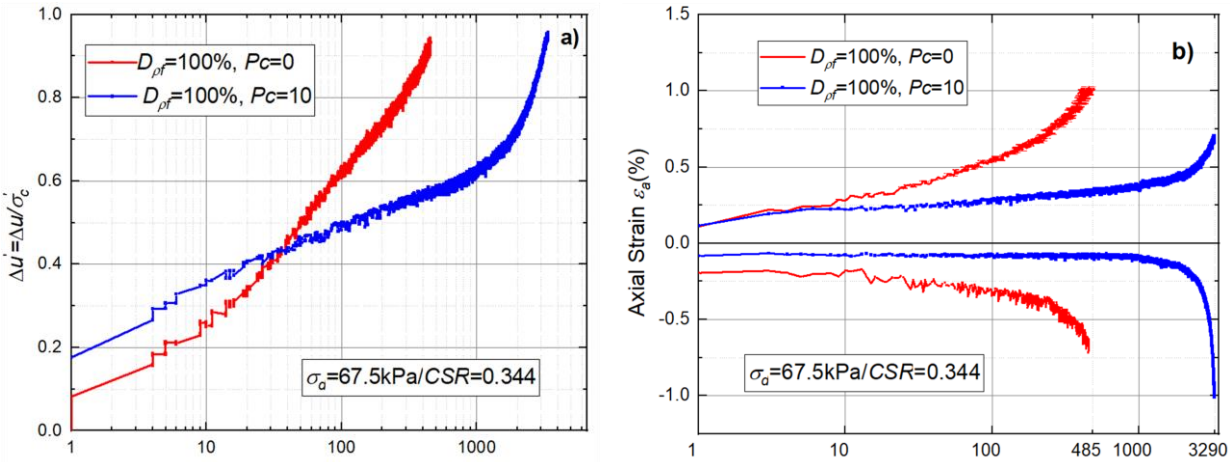

Figure 6-30 Comparison of accumulated pore water pressure and axial strain in unreinforced (*Pc* = 0) and fiber-reinforced LSS at *CSR* = 0.344 (All tests with σ_c' = 98.1 kPa, σ_s = 0 kPa, η_0 = 0, $\dot{s} = 5.04\ \%/min$)

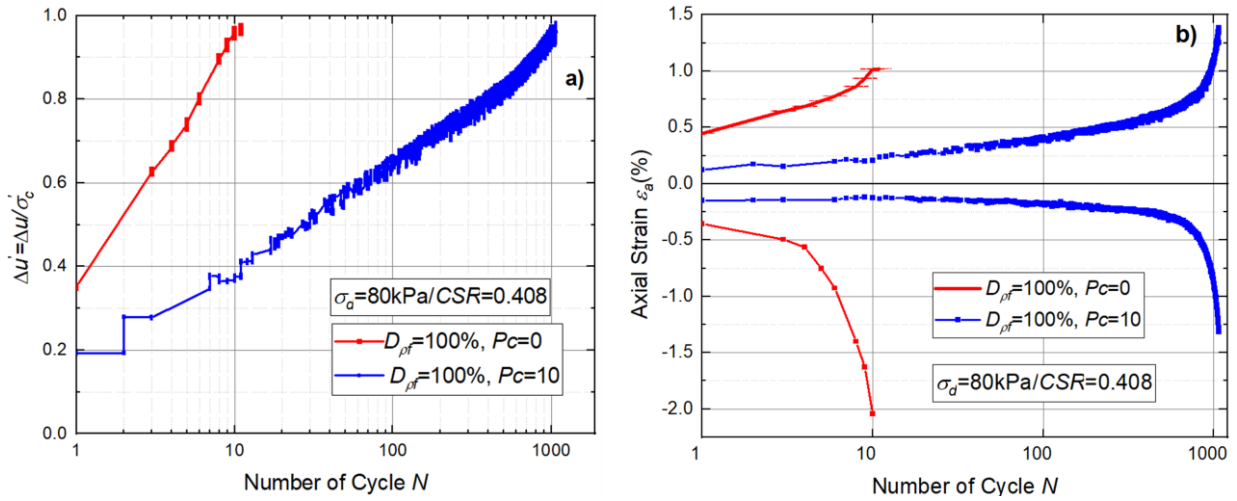

Figure 6-31 Comparison of accumulated pore water pressure and axial strain in unreinforced (*Pc* = 0) and fiber-reinforced LSS at *CSR* = 0.408 (All tests with σ_c' = 98.1 kPa, σ_s = 0 kPa, η_0 = 0, $\dot{s} = 5.04\ \%/min$)

The excess pore water pressure and double axial strain accumulation rate were found to increase in high rate to failure criterion at LSS without fiber, as shown in Figure 6-30, 31. Therefore, the number of cycles N_f required to reach failure reduces remarkably in LSS without fiber material (*Pc* = 0) in comparison to LSS (*Pc* = 10) at high cyclic stress ratio; the reduction of number of cycles about 6 times at *CSR* =0.344, and about 10 times at *CSR* = 0.408, respectively. This result can be seen as the most effective method to mix fiber material into LSS to improve the cyclic strength and be more resistant against cyclic load. The analysis of cyclic stress ratio *CSR* against the number of cycles to reach the failure criterion N_f for unreinforced and fiber-reinforced LSS is presented in Figure 6-32. It was found clearly that the failure envelops of unreinforced LSS (*Pc* = 0) are so low

in comparison to reinforced LSS (Pc = 10) and it was well described (R^2 = 0.99) by a potential function in form $CSR = aN_f^b$ with a = 0.46 and b = -0.05.

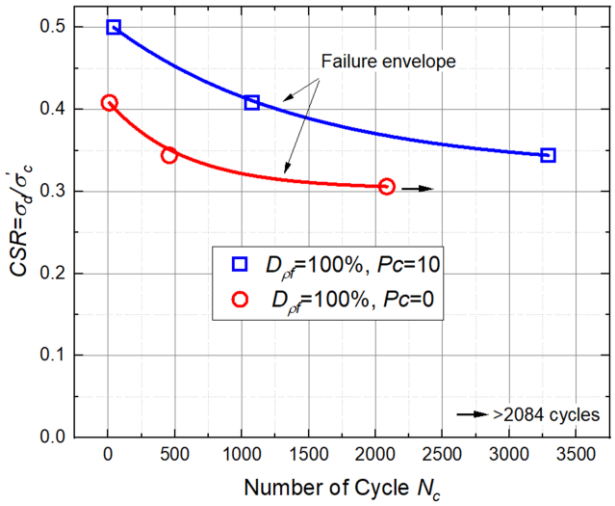

Figure 6-32 CSR versus Number of cycles N_f for unreinforced LSS and reinforced LSS

6.5.7. The Effect of Slurry Density on Unreinforced and Reinforced LSS under Cyclic Loading

In this part of study, the undrained cyclic triaxial tests were performed on unreinforced (Pc = 0) and reinforced LSS (Pc = 10) with changing slurry density. The aim of the tests is to observe the effect of slurry density on the cyclic behavior of LSS. The slurry density changing rate was applied at 95 %, 100%, and 105%, respectively. All tests were consolidated isotropically at 98.1 kPa and cyclic stress amplitude of 67.5 kPa with a displacement rate $\dot{s} = 5.04\ \%/min$.

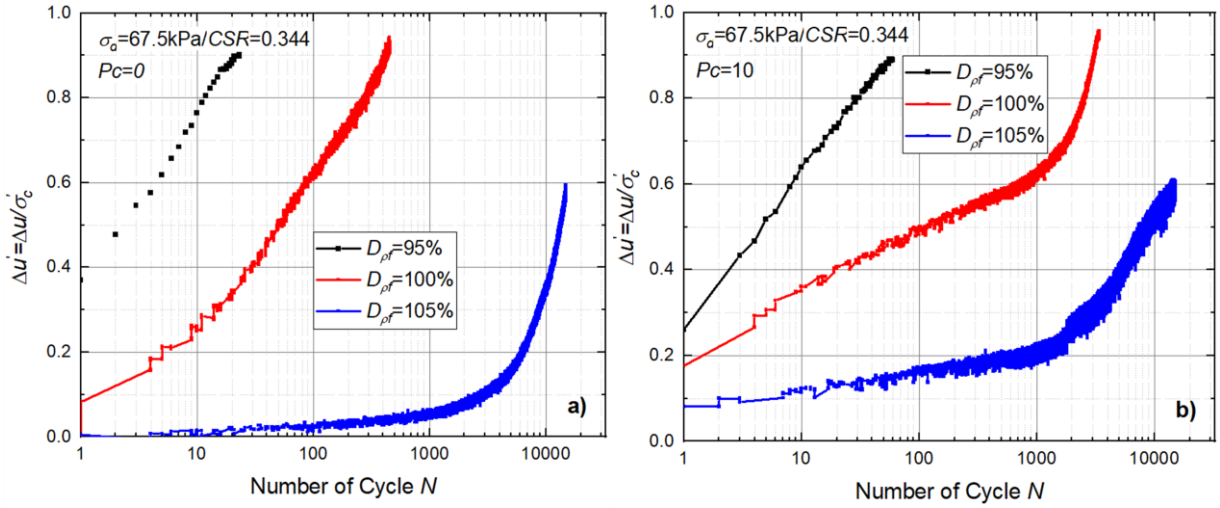

Figure 6-33 Comparison of accumulated pore water pressure with changing rate of slurry density for both unreinforced and reinforced LSS

The comparison of accumulated pore water pressure and double axial strain in tests at CSR = 0.344 with different slurry density changing rates for both unreinforced and reinforced LSS were presented in Figure 6-33 and Figure 6-34.

The result shows a great influence of slurry density on the development of pore water pressure and double axial strain in LSS (Pc = 0) and LSS (Pc = 10) with each subsequent cycle. The accumulation rate of pore

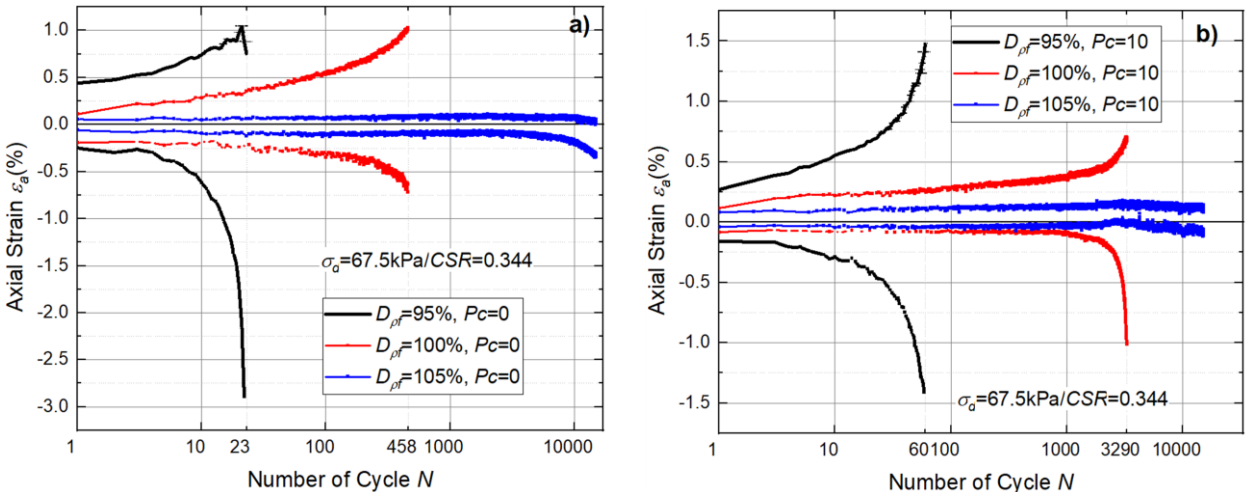

Figure 6-34 Comparison of accumulated double axial strain with changing rate of slurry density for both unreinforced and reinforced LSS

pressure in the test with slurry density $D_{\rho f}$ = 95 % increased rapidly to the failure criterion compared to the test with basic slurry density $D_{\rho f}$ = 100 %. While the rate of pore water pressure accumulation in the test with the highest slurry density changing rat $D_{\rho f}$ = 105 % is the lowest and did not reach the failure criterion, as shown in Figure 6-33. Double axial strain development was similar to the development of pore water pressure, as shown in Figure 6-34. In addition, the increasing tendency of pore water pressure and axial strain when reducing slurry density was also found to be similar to both LSS without fiber and LSS mixed fiber. However, in the case of adding fiber, the rate of this accumulation was observed to be lower than. In terms of the number of cycles required to reach failure criterion N_f when subjected to cyclic loading, the number of cycles N_f reduces rapidly with decreasing slurry density. 23 cycles were required to reach failure for LSS without fiber (Pc = 0) at low slurry density ($D_{\rho f}$ = 95 %) while LSS at basic slurry density ($D_{\rho f}$ = 100 %) necessitated 458 cycles, and LSS at high slurry density ($D_{\rho f}$ = 105 %) not reach failure after 10000 cycles. Inspection of LSS mixed fiber (Pc = 10), 60 cycles were required to reach failure at low slurry density ($D_{\rho f}$ = 95 %) while LSS at basic slurry density ($D_{\rho f}$ =100 %) necessitated 3290 cycles, and LSS at high slurry density ($D_{\rho f}$ = 105 %) not reach failure after 10000 cycles. As a result, increasing slurry density decreases the rate of development of pore water pressure and axial strain. It increases cyclic strength and deformation resistance in both unreinforced and reinforced LSS under cyclic loading.

Figure 6-35 shows the cyclic stress-strain behavior of unreinforced and reinforced LSS with different slurry densities. It was found that the effect of slurry density on cyclic stress-strain behavior of LSS is significant. By adding fiber material into LSS, the cyclic stress-strain behavior is more symmetrical than in the case of unreinforced fiber. In conclusion, increasing slurry density and adding fiber material into LSS significantly improve the cyclic strength and earthquake resistance.

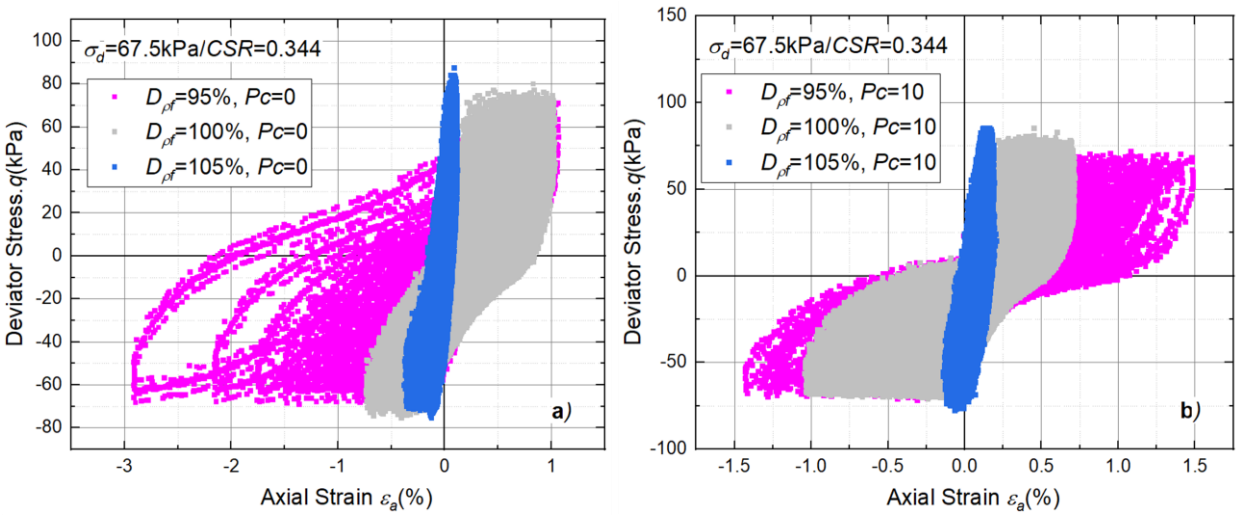

Figure 6-35 The cyclic stress-strain behavior of unreinforced and reinforced LSS with different slurry density

6.5.8. The Effect of Cement on Reinforced LSS (*Pc = 10*) under Cyclic Loading

As mentioned in section 4, the LSS easily occurs brittle failure with increasing cement content, and it was found that adding fiber content improves the brittle property of the LSS. However, cement content plays a vital role in improving the cohesion of LSS mixed fiber under cyclic loading. Therefore, in this section the cyclic test on the LSS mixed fiber (*Pc* = 10) with reducing 20 % of amount of cement content (*C* = 80 %) was conducted to investigate the effect of cement content on the cyclic behavior of LSS. The effect of cyclic stress ratio *CSR* on the LSS (*Pc* = 10) was also presented.

The comparison of accumulated pore water pressure and axial strain in LSS (*Pc* = 10) with a range of *CSR* from 0.204 to 0.408 were shown in Figures 6-36, 6-37, and Figure 6-38.

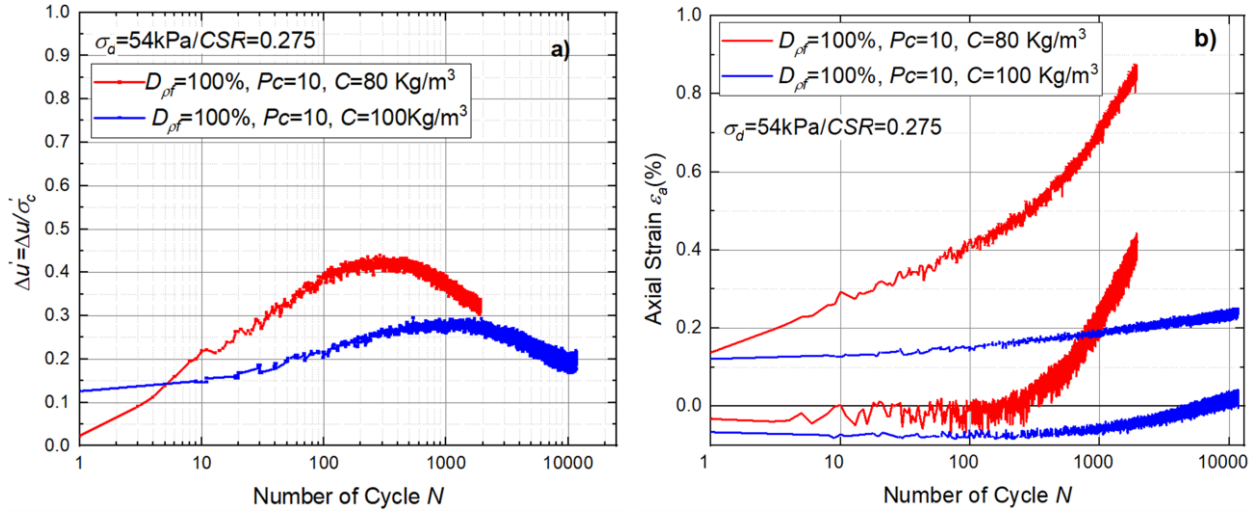

Figure 6-36 Comparison of accumulated pore water pressure and axial strain in fiber-reinforced LSS (*Pc* = 10) at *CSR* = 0.275 (All tests with σ_c' = 98.1 kPa, σ_s = 0 kPa, η_0 = 0, $\dot{s} = 5.04\ \%/min$)

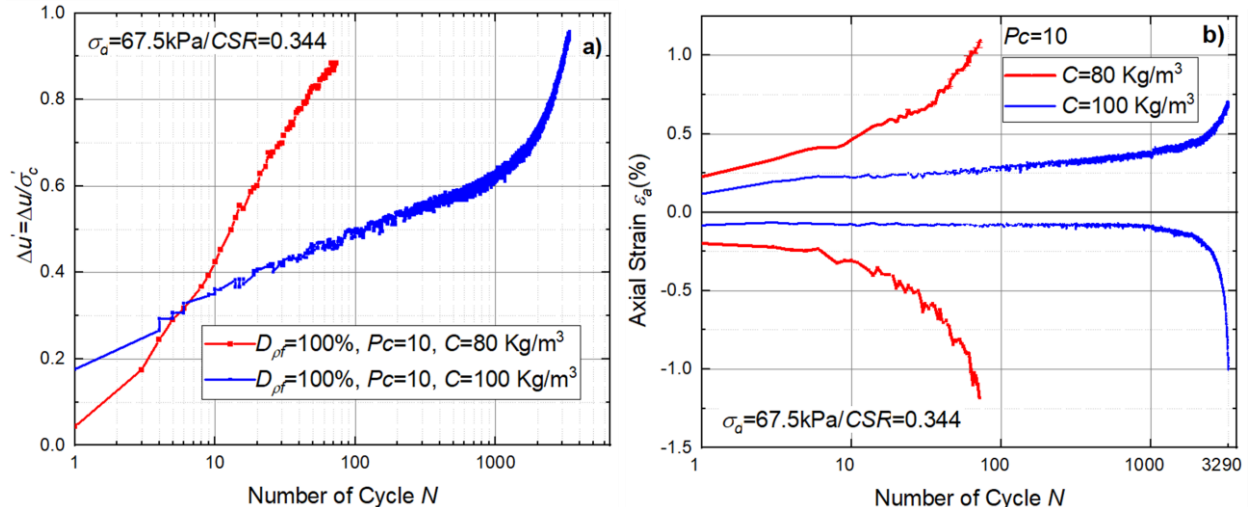

Figure 6-37 Comparison of accumulated pore water pressure and axial strain in fiber-reinforced LSS (*Pc* = 10) at *CSR* = 0.344 (All tests with σ_c' = 98.1 kPa, σ_s = 0 kPa, η_0 = 0, $\dot{s} = 5.04\ \%/min$)

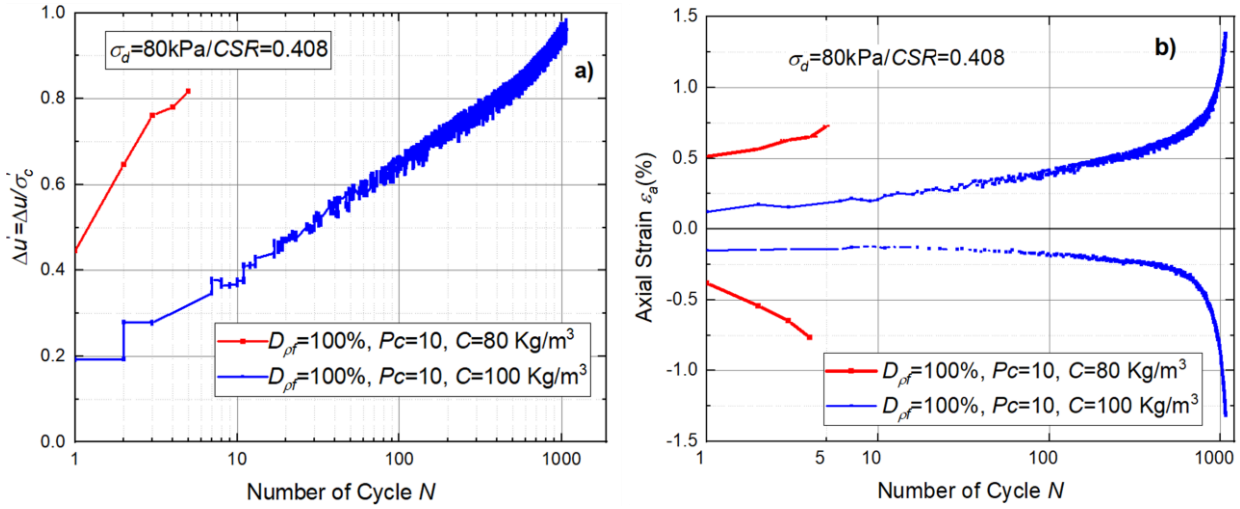

Figure 6-38 Comparison of accumulated pore water pressure and axial strain in fiber-reinforced LSS (*Pc* = 10) at *CSR* = 0.408 (All tests with σ_c' = 98.1 kPa, σ_s = 0 kPa, η_0 = 0, $\dot{s} = 5.04\ \%/min$)

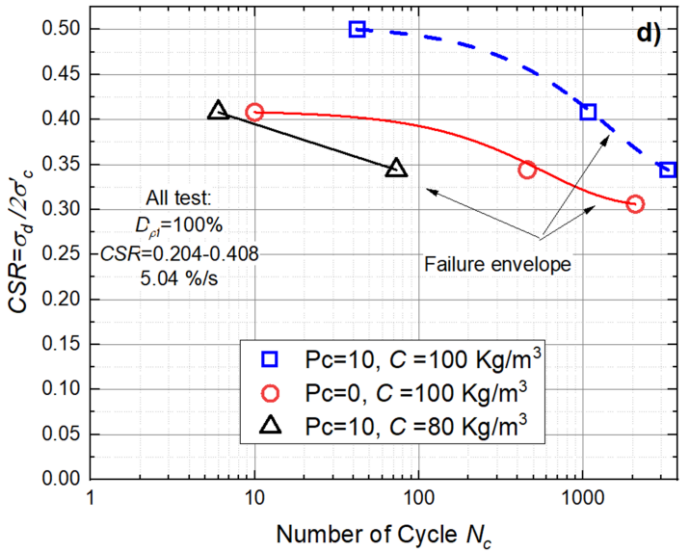

Figure 6-39 *CSR* versus Number of cycles N_f for reinforced LSS (*Pc* = 10) with different amount of cement content

The result suggested that the accumulation rate of pore water pressure and axial strain in LSS grew up quickly to the failure criterion when reducing 20 % of the amount of cement content in compared to LSS (*Pc* = 10, *C* = 100 Kg/m^3). By adding fiber at a low cyclic stress amplitude, the negative pore water pressure appears in both LSS (*C* = 100 Kg/m^3) and LSS (*C* = 80 Kg/m^3). In addition, the number of cycles required to fail N_f also decreases rapidly with increasing the *CSR* and reducing the amount of cement content. Compared to adding fiber, cement content reduction's influence on reducing the cyclic strength of LSS seems more remarkable, as shown in Figure 6-39.

6.5.9. Stiffness Degradation

Cyclically loaded LSS exhibited stiffness degradation. In order to investigate the stiffness degradation of LSS, the degradation of undrained equivalent Young's modulus E_{eq} during cyclic loading was quantified by the so-called "degradation index" δ, which is defined as follows:

$$\delta = \frac{E_{eq}(N)}{E_{eq}(1)}$$

Where $E_{eq}(N)$ and $E_{eq}(1)$ are equivalent Young's modulus after N cycles and the first cycle at constant deviator stress amplitude, respectively. Small δ values correspond to a high degree of stiffness degradation.

From Figure 6-40 to Figure 6-43 present the evolution of the degradation index and normalized equivalent Young's modulus, with increasing number of cycles, and shows that both the magnitude and rate of its influenced by a number of factors: Cyclic stress ratio, fiber material, slurry density, initial mean pressure σ_c', initial stress σ_s, displacements rate, and amount of cement.

Typically, E_{eq} is nonlinear, which decreases with increasing the number of cycles and increasing strain amplitude. Strong influence by cyclic stress ratio, fiber material, and slurry density on rate of stiffness degradation as shown in Figures 6-40 and 6-41. The degradation index was smaller and the stiffness degraded quicker than when the cyclic stress ratio was increased. At a low cyclic stress ratio (*CSR* = 0.275), E_{eq} started to decrease at the beginning of the loading, then kept stable until about 10000 cycles, then increased to the end of the cyclic test without reaching failure due to the dilation. In contrast, the degradation index δ drops significantly more than 40% during the first 100 cycles and reduces quickly to reach the failure in medium and high cyclic stress ratios (*CSR* = 0.344 and *CSR* = 0.408). The degradation rate was also faster than with LSS without fiber material (*Pc* = 0). The results show that the curve of normalized equivalent modulus with amplitude strain is nonlinear, and initial E_{eq} decreases with increasing *CSR* and increasing single strain amplitude, as shown in Figure 6-40 b). Especially after 0.2 % of single amplitude strain, the curve seems to be returned to the normalized E_{eq}/E_0 curve of the monotonic test.

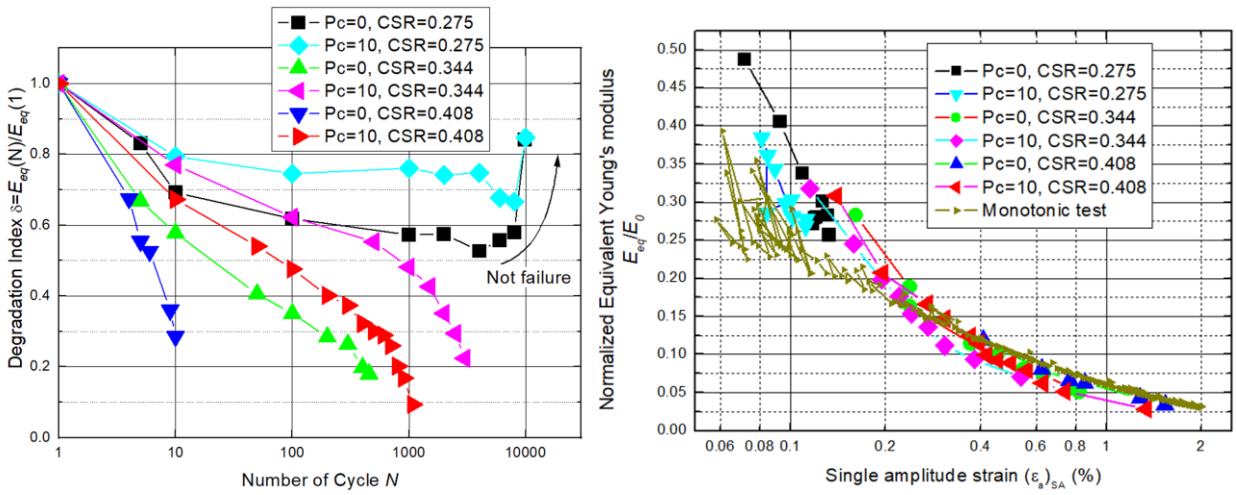

Figure 6-40 The effect of cyclic stress ratio and fiber material on stiffness degradation; a) Degradation index versus number of cycles, b) Normalized Equivalent Young's modulus versus single amplitude strain.

As similar to the tendency of degradation index effected by cyclic stress ratio, the effect of slurry density on stiffness degradation is remarkable. The degradation index was found to be high at high slurry density and initial Equivalent Young's modulus E_{eq} decrease with decreasing slurry density.

Figure 6-42 presents the effect of initial mean pressure σ_c' on stiffness degradation of LSS mixed fiber (Pc = 0). The Figure show that the rate of degradation index is same during 10 cycles, then decreases faster at lower initial mean pressure σ_c'(σ_c' = 98.1 kPa) when increasing number of cycles than a high initial mean pressure σ_c' (σ_c' = 196 kPa) and approach the failure at large single amplitude strain, while did not reach in case of σ_c' = 196 kPa.

The tendency of stiffness degradation of reinforced LSS under the effect of initial stress σ_s is different from other factor at the beginning of loading as shown in Figure 6-43. The degradation index tends to increasing slightly during first 10 cycles, then decrease quickly to the failure with the case of a high initial stress and did not to reach the failure at the case of a low initial stress (σ_s = 27 kPa). This result show that LSS mixed fiber tend to dilates slightly before continuously compress to the failure. In addition, at a low initial stress degradation index increase after 1000 cycles cause by the dilation in LSS mixed fiber. The decrease tendency of normalized

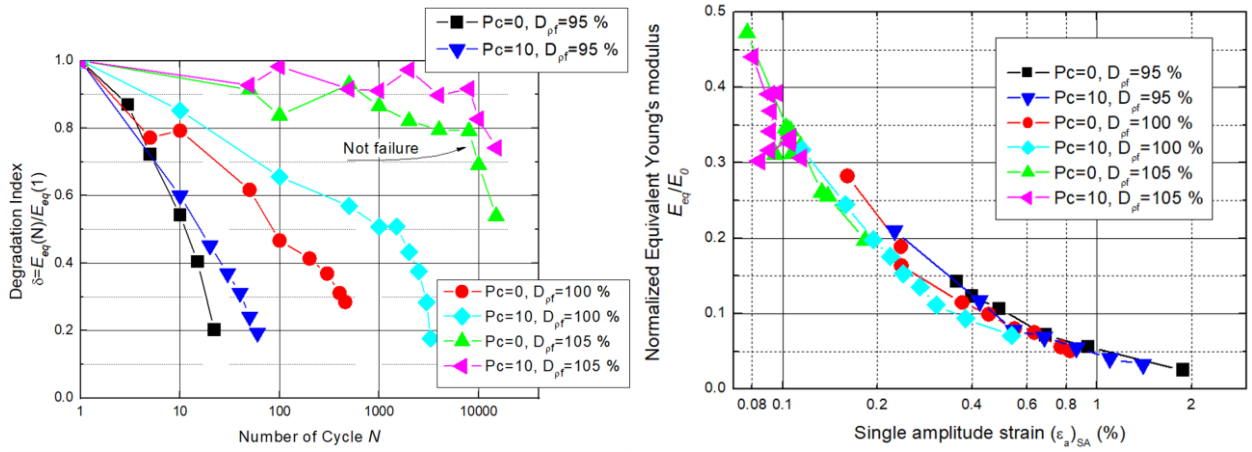

Figure 6-41 The effect of Slurry density and fiber material on stiffness degradation; a) Degradation index versus number of cycles, b) Normalized Equivalent Young's modulus versus single amplitude strain.

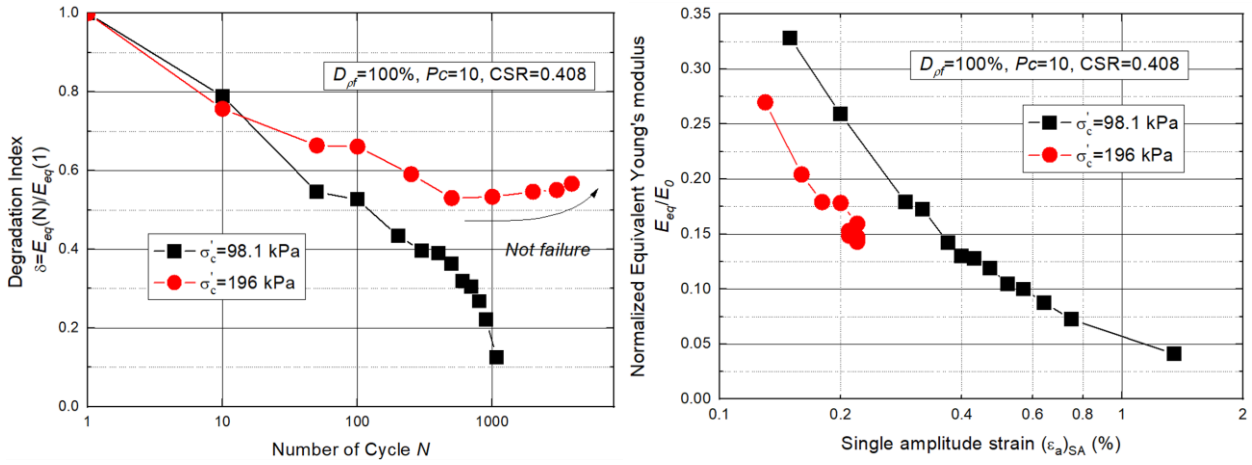

Figure 6-42 The effect of initial mean pressure σ_c' on stiffness degradation; a) Degradation index versus number of cycles, b) Normalized Equivalent Young's modulus versus single amplitude strain.

Equivalent Young's modulus with single strain amplitude was found to be similar and independent with increasing initial stress σ_s.

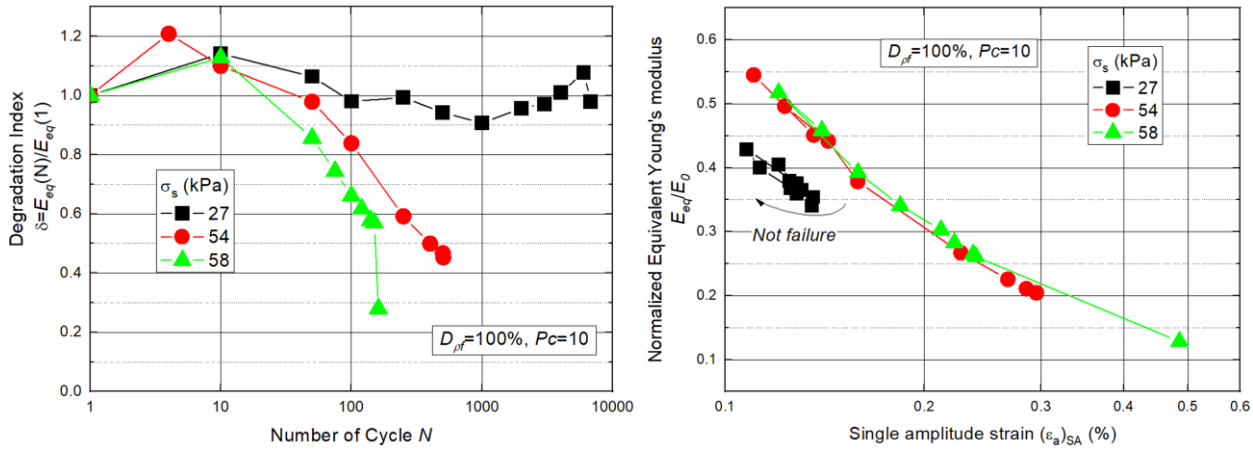

Figure 6-43 The effect of initial stress σ_s on stiffness degradation; a) Degradation index versus number of cycles, b) Normalized Equivalent Young's modulus versus single amplitude strain.

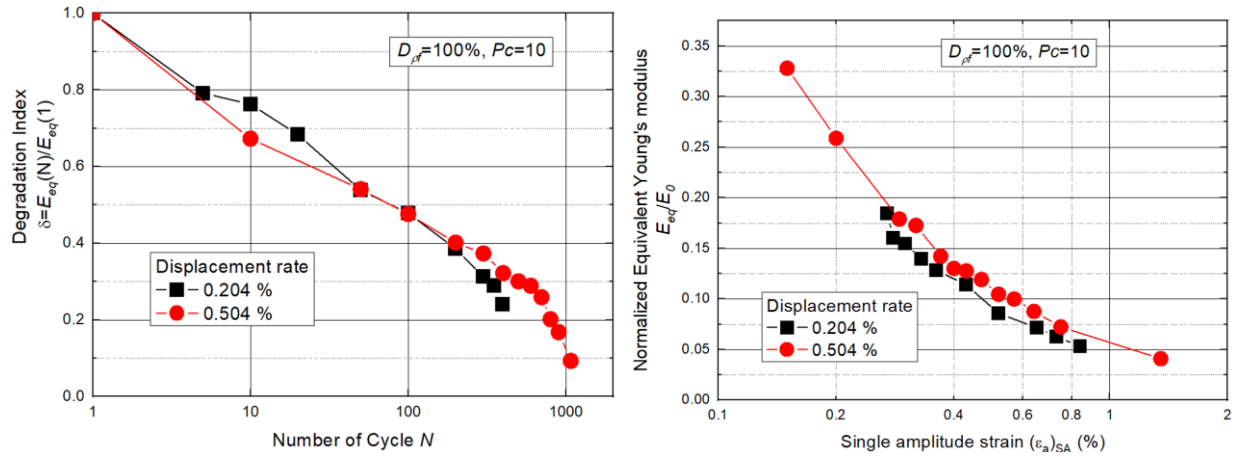

Figure 6-44 The effect of displacement rate on stiffness degradation; a) Degradation index versus number of cycles, b) Normalized Equivalent Young's modulus versus single amplitude strain.

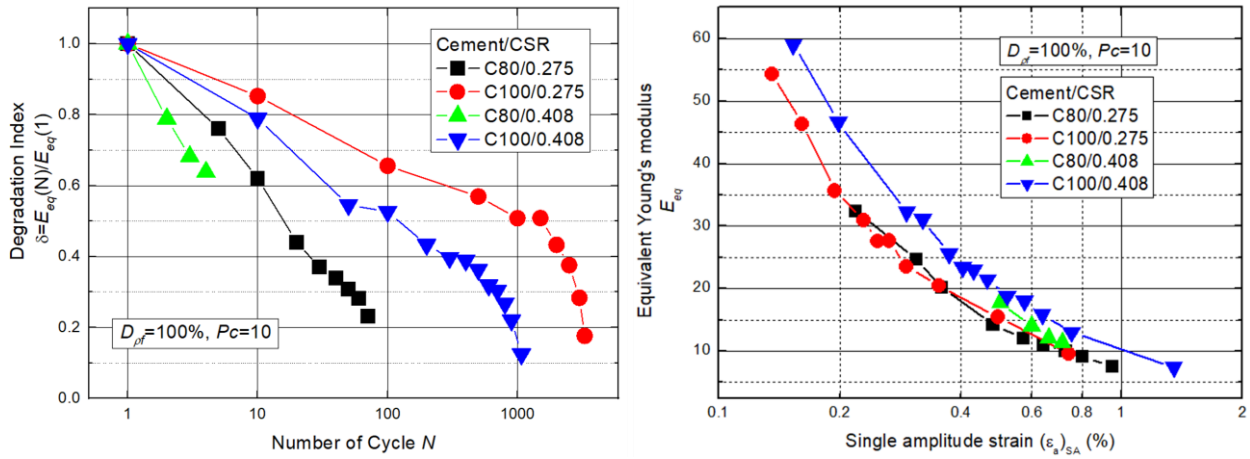

Figure 6-45 The effect of amount of cement on stiffness degradation; a) Degradation index versus number of cycles, b) Normalized Equivalent Young's modulus versus single amplitude strain.

The results also show that the effect of displacement rate on reinforced LSS stiffness degradation is negligible in comparison with the effect of cement reduction was found strong influence on degradation index as shown in Figures 6-34 and 6-35. The rate of degradation index decreases faster to reach the failure when decreasing amount of cement as shown in Figure 6-35.

6.5.10. Hysteresis Damping Factor *h* (%)

Figure 6-46 to Figure 6-51 show the evolution of the energy loss factor, *h*, with cycle number and single strain amplitude under various factors. It shows clear that the hysteresis damping factor, *h*, appears to be governed by the cyclic strain level, which increase with increasing number of cycles and cyclic strain amplitude. The dissipated strain energy increases substantially and simultaneously decreases the stored strain energy to the failure with increasing cycle number and cyclic strain level. Especially after curtain cycle or cyclic strain level, the hysteresis damping factor raise up quickly to the failure.

The effect of fiber material, slurry density, cement content, cyclic stress ratio, initial stress, initial mean pressure, and displacement rate of test on the energy loss factor was found be remarkable. The adding fiber material into LSS reduce significantly dissipated strain energy, which means the cyclic strength improve substantially. At a low cyclic stress level (*CSR* = 0.275), a high slurry density ($D_{\rho f}$ = 105 %), and a low initial stress (σ_s =27 kPa), the response of LSS is largely elastic. Therefore, hysteresis damping factor increase lightly at the beginning of loading, the remained stably after 10000 cycles and the damping factor points migrated down and to the left at small single strain amplitude.

In contrast, accumulated plastic strain and energy loss factor increasing remarkable when increasing cyclic stress level CSR, increasing initial stress σ_s, and decreasing slurry density, initial mean pressure, cement content, and displacement rate, respectively.

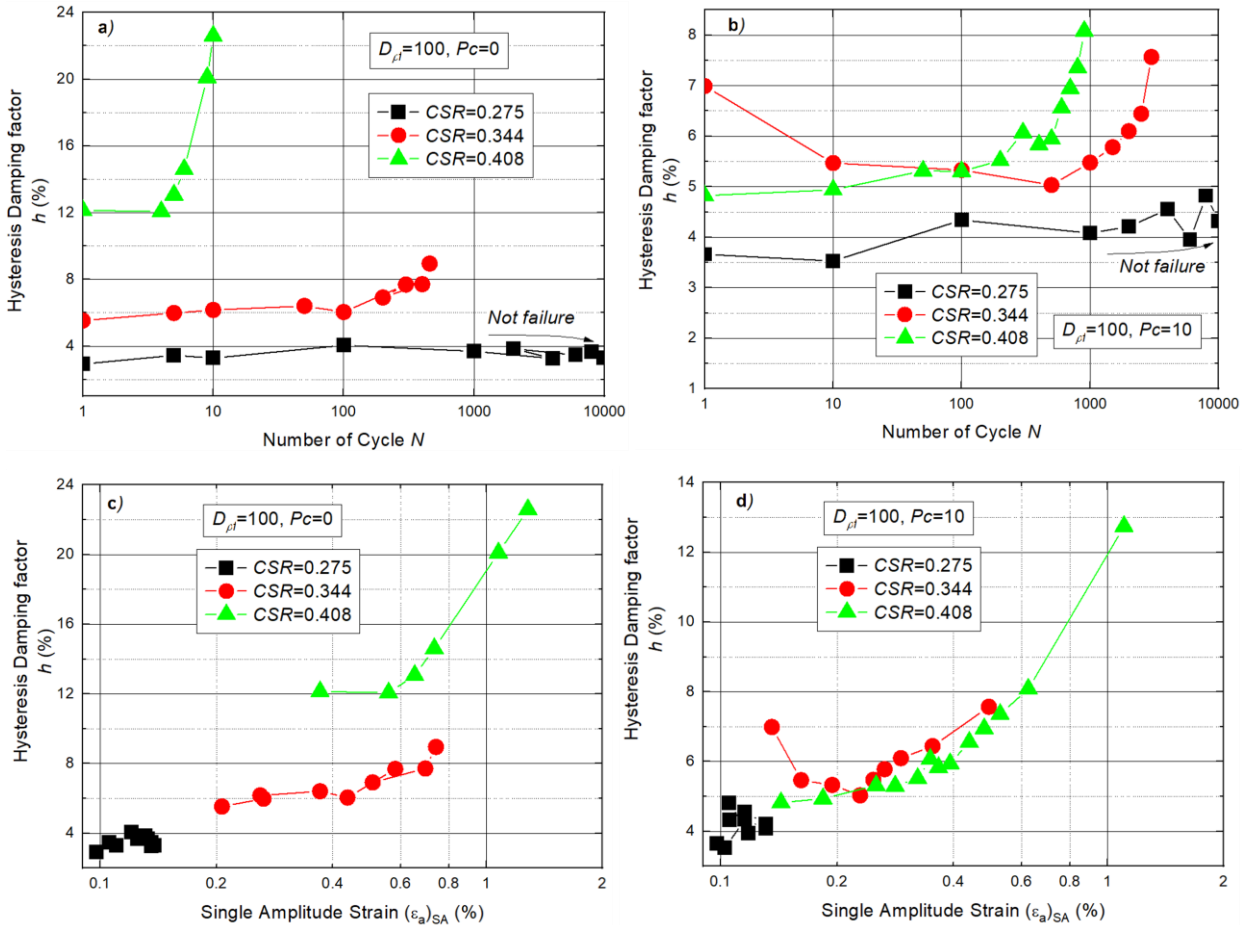

Figure 6-46 The effect of cyclic stress ratio on hysteresis damping factor; a) and b) Hysteresis damping factor against with number of cycles, c) and d) Hysteresis damping factor against with single amplitude strain.

The results also show that the hysteresis damping factor decrease in beginning of loading during 10 cycles and reveal U-shaped damping ratio cluster in the most cases that approach to failure. It can be explained the response of the stress-strain behavior of LSS during first few cycles are highly elastic. Which cause dissipated strain energy decreases and progressively increase stored strain energy.

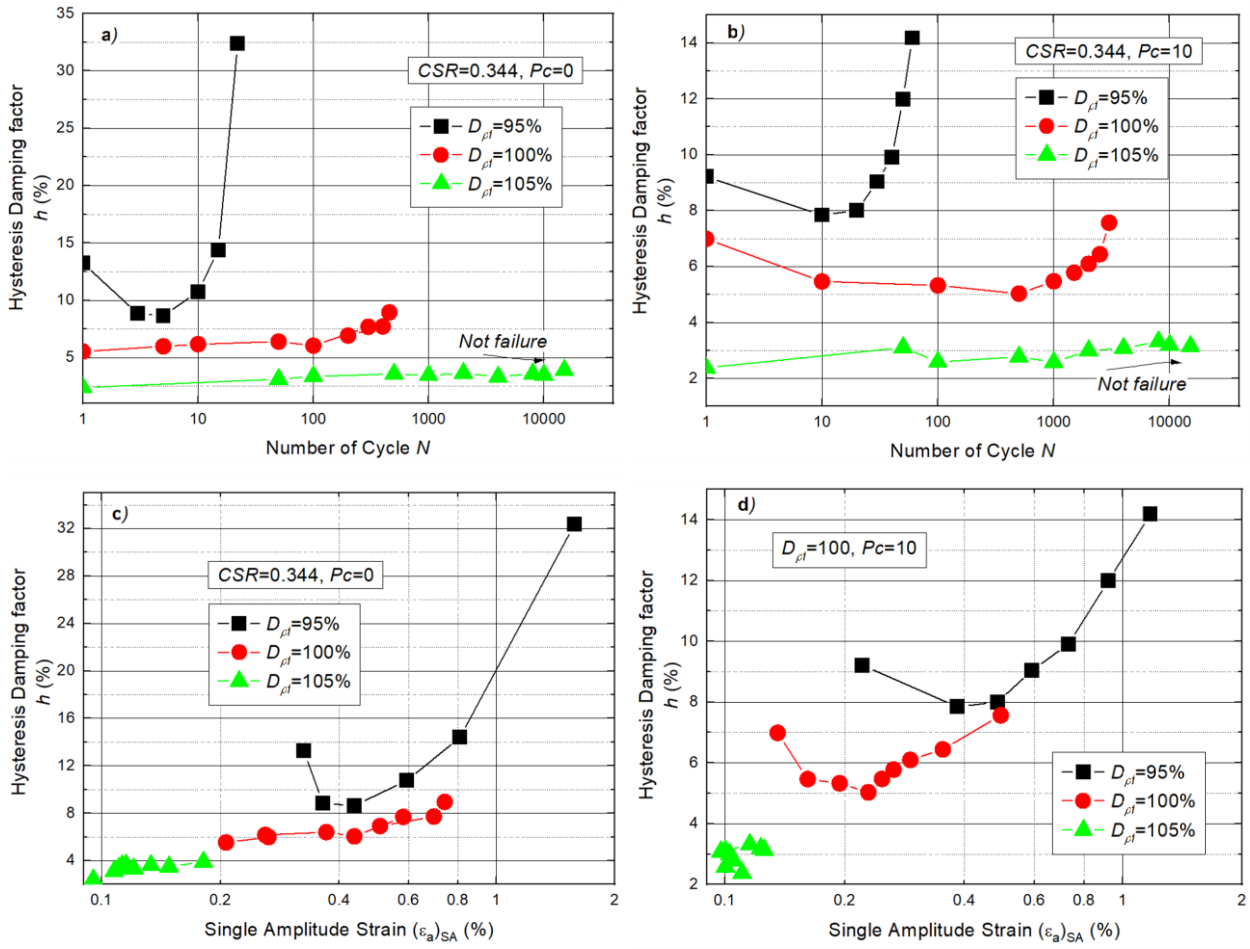

Figure 6-47 The effect of slurry density on hysteresis damping factor; a) and b) Hysteresis damping factor against with number of cycles, c) and d) Hysteresis damping factor against with single amplitude strain.

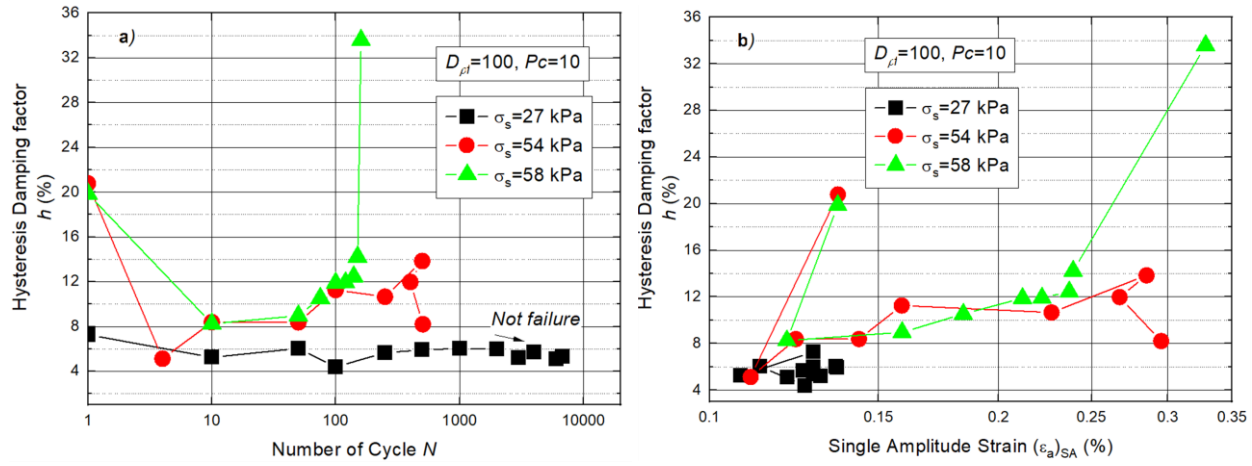

Figure 6-48 The effect of initial stress σ_s on hysteresis damping factor; a) Hysteresis damping factor against with number of cycles, b) Hysteresis damping factor against with single amplitude strain.

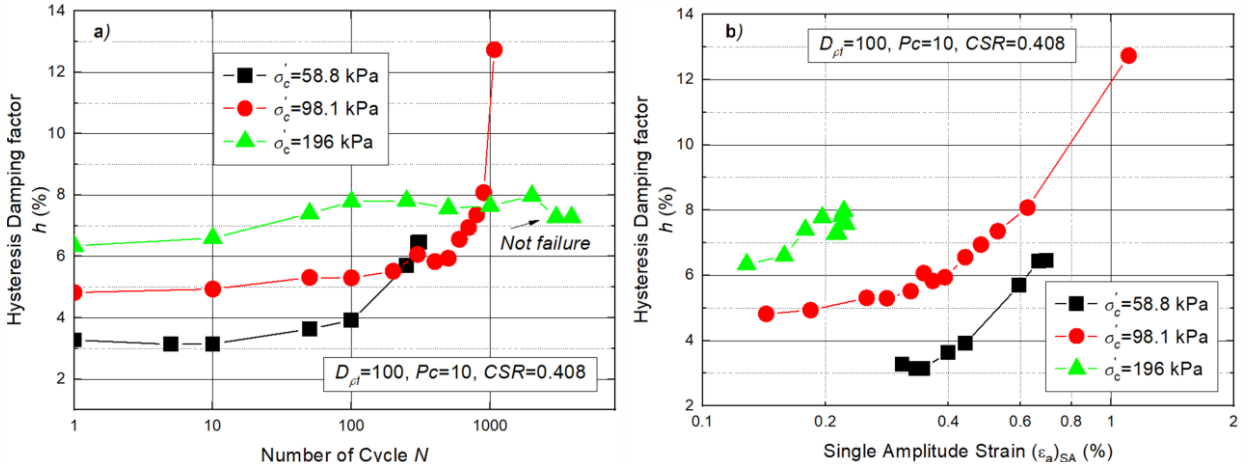

Figure 6-49 The effect of initial mean pressure σ_c' on hysteresis damping factor; a) Hysteresis damping factor against with number of cycles, b) Hysteresis damping factor against with single amplitude strain.

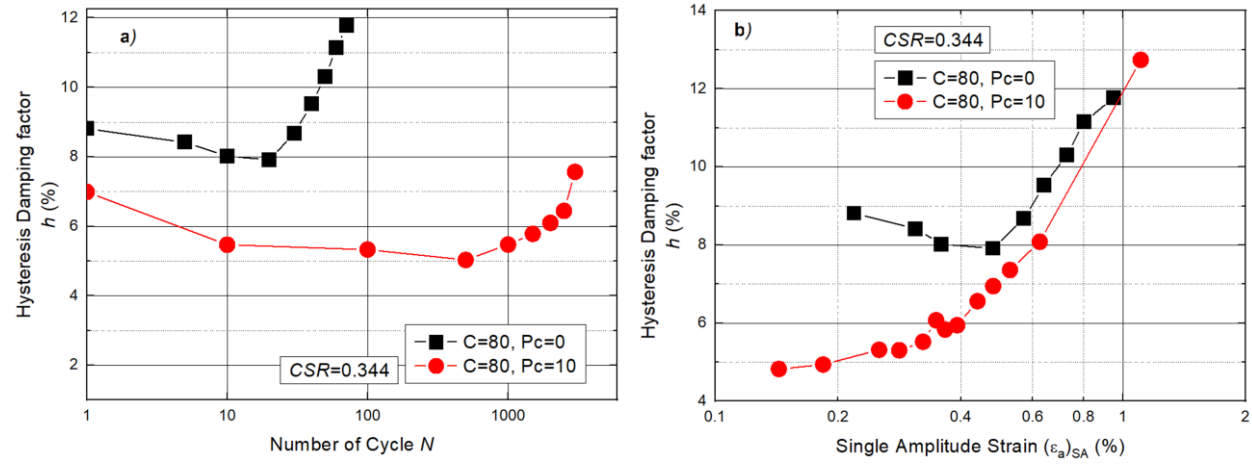

Figure 6-50 The effect of cement content on hysteresis damping factor; a) Hysteresis damping factor against with number of cycles, b) Hysteresis damping factor against with single amplitude strain.

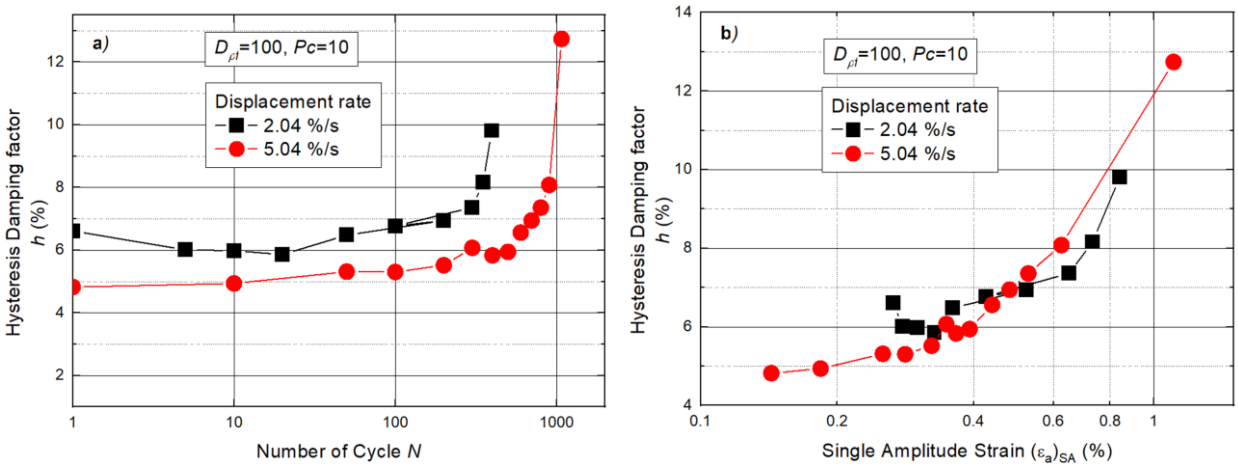

Figure 6-51 The effect of cement content on hysteresis damping factor; a) Hysteresis damping factor against with number of cycles, b) Hysteresis damping factor against with single amplitude strain.

6.6. Summary

This chapter has presented the results of 54 undrained monotonic and cyclic triaxial tests undertaken on reinforced and unreinforced LSS at variations of cyclic tests and different material variables. All LSS samples were cured at the laboratory with 28 days of curing time.

The monotonic tests with different initial pressures primarily served to provide the critical state lines used as a reference for the analysis of the cyclic tests.

In the cyclic tests, the excess pore water pressure continuously increases and simultaneously decreases the effective stresses with increasing number of cycles. The sample becomes weaker with the cycle number and accumulated axial strain increases gradually.

The failure mode is highly dependent on the cyclic deviator stress amplitude (σ_d) and initial deviator stress (σ_s). For symmetrical loading (σ_s = 0), the pore water pressure and double axial strain amplitude grew with an increasing number of cycles and deviator stress amplitude. LSS mixed fiber material finally failed due to too large strain amplitudes (a failure criterion of ε_1 = 2.5 % was used in all tests). The true liquefaction ($q = p' = 0$) did not reach in LSS. In the final stage, the effective stress loops pass a "Butterfly" stress path shape, and the distance of the final stress loop is smaller than to the origin with lower stress amplitude.

For nonsymmetrical loading ($\sigma_s > 0$), an accumulation of compressional axial strain with each subsequent cycle occurred, while the mobilized double axial strain remained almost constant. Therefore, the failure criterion was fulfilled due to an excessive accumulation of permanent strains (a failure criterion of ε_1 = 10 %). In contrast to the tests with symmetrical loading, the accumulated pore pressure increases from the first cycle up to maximum value and, after that, decreases quickly to failure while the axial strain progressively grows in each subsequent cycle. This caused the effective stress loops to migrate to pass over the CSL, then return to the touch again of the failure envelope, and the shape of the stress loop at the final stage did not pass the "butterfly" shape or lens shape. As a result, LSS mixed fiber material tends to dilate before reaching the failure criterion.

Increasing initial stress can improve the cyclic resistance of the material, by 'shifting' the stress path up in $p' - q$ space and, thus, further away from the extension failure envelope. As a result, the cyclic resistance of LSS mixed fiber increase significantly when increasing initial stress σ_s.

There is a threshold value of the stress level *CSR* between 0.275 to 0.344. If the stress level is higher than that value, the LSS cyclic behavior is more contractive and reaches the failure criterion by excessing the double axial strain amplitude; otherwise, the LSS sample is more dilative by the accumulation of permanent axial strain and did not reach to the failure.

An increase of deviator stress amplitude and initial stress drastically reduces the number of cycles to reach failure conditions and simultaneously equivalent Young's modulus decrease remarkable, while hysteresis damping factor increase significantly with cycle number and cyclic strain level.

For smaller stress levels and low initial stress (*CSR* <0.275), the equivalent Young's modulus started to decrease at the beginning of the tests and then increased until the end of the tests. That means the LSS mixed fiber softened at the beginning, then hardened.

In the tests with symmetrical loading, the rate of pore pressure accumulation grew with increasing stress or strain amplitude, while it was reduced with increasing values of initial mean pressure. Therefore, increasing

initial mean pressures σ_c' leads to increasing cyclic resistance. In contrast, reducing the initial mean pressure significantly decreases the number of cycles N_f required to reach the failure criterion.

Under a lower displacement rate, the strength of the sample reduces more quickly than under a higher displacement rate with each subsequent cycle. The stress-strain becomes more nonsymmetrical and tends to enlarge in compression mode, revealing that the compression strength is weaker than when applying a cyclic test with a low displacement rate.

The effect of fiber material, slurry density, and cement content on LSS cyclic behavior are significant.

Adding fiber material into LSS significantly reduces dissipated strain energy and is more resistant to deformation. It causes the cyclic stress-strain behavior to be more symmetrical than in the case of unreinforced fiber, which means the cyclic strength improves substantially.

With LSS without fiber and decreasing slurry density and cement content, the rate of accumulated pore water pressure and axial strain increases rapidly with the number of cycles. In addition, the degradation index and the number of cycles required for the failure also reduce remarkably.

The accumulated plastic strain and energy loss factor increase remarkably when increasing cyclic stress level *CSR*, increasing initial stress σ_s, and decreasing slurry density, initial mean pressure, cement content, and displacement rate, respectively.

Compared to adding fiber, cement content reduction's influence on reducing the cyclic strength of LSS seems more remarkable.

The hysteresis damping factor decreases at the beginning of loading during ten cycles and reveals a U-shaped damping ratio cluster in most cases that approach failure. It can be explained the response of the stress-strain behavior of LSS during the first few cycles are highly elastic. Which cause dissipated strain energy to decrease and progressively increase stored strain energy.

All tests show that the deviator stress decreases suddenly after the first cycle in strain-controlled cyclic tests and the effective stress paths move to the CSL and exhibit a “fir tree” shape similar to those observed in tests on the sand.

Tests at the cyclic test and material variables showed patterns of behavior that could be captured by empirical equations allowing the strains, stiffness, and damping ratios to be predicted under given numbers of cycles and specified cyclic loading conditions.

CHAPTER 7
NUMERICAL MODELING

7. Numerical Modeling

7.1. Introduction

The purpose of this chapter is the implementation of a numerical simulation route for the modified Ramberg-Osgood model using the Delphi programming language to verify the behavior of reinforced LSS under undrained cyclic triaxial tests. For this purpose, the undrained cyclic triaxial test model is simulated by the modified Ramberg-Osgood formulations and compared with experimental test results. Based on this result, the satisfactory evaluation of the model is presented, and the set of dynamic parameters of the model will propose, which play a vital role in the analysis of seismic vibration of the application LSS under cyclic loading by Finite Element Method (FEM).

Firstly, review of constitutive model of material, but focus on elastoplasticity model are presented.

Secondly, the detailed descriptions of Ramberg-Osgood formulation are then provided. Numerical integration techniques commonly used for implementing numerical models are briefly reviewed, and the backward Euler method (Smith and Griffith 2004) is applied to determine the shear stress increment. The Delphi implementation is performed.

Finally, the performance of undrained cyclic triaxial test model to compare with experimental results is assessed, and recommendations are provided.

7.2. Constitutive Models of Materials (Nghiem MH 2009)

7.2.1. Definition of Stress

The stress tensor defining stress state at a point can be represented by a vector in Cartesian coordinates:

$$\{\sigma\} = [\sigma_x \quad \sigma_y \quad \sigma_z \quad \tau_{xy} \quad \tau_{yz} \quad \tau_{zx}]^T \tag{7.1}$$

where σ_x, σ_y and σ_z are normal stresses in x, y and z directions, respectively; and τ_{xy}, τ_{yz} and τ_{zx} are shear stresses.

It is often more convenient to use principal stress than Cartesian stress components when formulating material models. The principal stresses can be shown as a stress vector:

$$[\sigma_1 \quad \sigma_2 \quad \sigma_3]^T \tag{7.2}$$

Each principal stress can be represented in terms of the fist stress invariant, I_1, and the second stress invariant, J_2, and Lode angle, θ (Smith and Griffiths, 1997):

$$\begin{aligned} \sigma_1 &= \frac{2}{\sqrt{3}}\sqrt{J_2}\,sin\left(\theta - \frac{2\pi}{3}\right) + \frac{I_1}{3} \\ \sigma_2 &= \tfrac{2}{\sqrt{3}}\sqrt{J_2}\,sin(\theta) + \tfrac{I_1}{3} \\ \sigma_3 &= \frac{2}{\sqrt{3}}\sqrt{J_2}\,sin\left(\theta + \frac{2\pi}{3}\right) + \frac{I_1}{3} \end{aligned} \tag{7.3}$$

where I_1 is the first stress invariant; J_2 and J_3 are the second and third stress invariants, respectively, and θ is the Lode angle. These values can be expressed in the following equations (Smith and Griffiths, 1997):

$$I_1 = \sigma_x + \sigma_y + \sigma_z \tag{7.4}$$

$$J_2 = \tfrac{1}{6}\left[\left(\sigma_x - \sigma_y\right)^2 + \left(\sigma_y - \sigma_z\right)^2 + (\sigma_z - \sigma_x)^2\right] + \tau_{xy}^2 + \tau_{yz}^2 + \tau_{zx}^2 \tag{7.5}$$

$$\theta = \tfrac{1}{3}sin^{-1}\left(\frac{-3\sqrt{3}}{2}\frac{J_3}{J_2^{3/2}}\right) \tag{7.6}$$

$$J_3 = s_x s_y s_z - s_x\tau_{yz}^2 - s_y\tau_{zx}^2 - s_z\tau_{xy}^2 + 2\tau_{xy}\tau_{yz}\tau_{zx} \tag{7.7}$$

$$\text{where } s_x = \left(\sigma_x - \frac{I_1}{3}\right);\ s_y = \left(\sigma_y - \frac{I_1}{3}\right);\ s_z = \left(\sigma_z - \frac{I_1}{3}\right) \tag{7.8}$$

Their derivatives are:

$$\begin{aligned}
\left\{\frac{\partial I_1}{\partial \sigma}\right\} &= [1 \quad 1 \quad 1 \quad 0 \quad 0 \quad 0]^T \\
\left\{\frac{\partial J_2}{\partial \sigma}\right\} &= \left[\sigma_x - \frac{I_1}{3} \quad \sigma_y - \frac{I_1}{3} \quad \sigma_z - \frac{I_1}{3} \quad 2\tau_{xy} \quad 2\tau_{yz} \quad 2\tau_{zx}\right]^T \\
\left\{\frac{\partial J_3}{\partial \sigma}\right\} &= \left[s_y s_z + \frac{J_2}{3} - \tau_{yz}^2 \quad s_z s_x + \frac{J_2}{3} - \tau_{zx}^2 \quad s_x s_y + \frac{J_2}{3} - \tau_{xy}^2\right. \\
&\left. -2s_z\tau_{xy} + 2\tau_{yz}\tau_{zx} \quad 2s_x\tau_{yz} + 2\tau_{xy}\tau_{zx} \quad 2s_y\tau_{zx} + 2\tau_{xy}\tau_{yz}\right]^T \\
\left\{\frac{\partial \theta}{\partial \sigma}\right\} &= \frac{\sqrt{3}}{2\cos 3\theta J_2^{\frac{3}{2}}}\left(-\left\{\frac{\partial J_3}{\partial \sigma}\right\} + \frac{3J_3}{2J_2}\left\{\frac{\partial J_2}{\partial \sigma}\right\}\right)
\end{aligned} \tag{7.9}$$

7.2.2. Definition of Strain

The strain tensor at a point can be represented by a vector in Cartesian coordinates:

$$\{\varepsilon\} = [\varepsilon_x \quad \varepsilon_y \quad \varepsilon_z \quad \gamma_{xy} \quad \gamma_{yz} \quad \gamma_{zx}]^T \tag{7.10}$$

where ε_x, ε_y and ε_z are the normal strain in the x, y and z directions, respectively; and γ_{xy}, γ_{yz} and γ_{zx} are shear strains.

The relationships between strain and three components of displacements, u, v, and w in Cartesian coordinates are given by:

$$\{\varepsilon\} = \begin{bmatrix} \frac{\partial}{\partial x} & 0 & 0 \\ 0 & \frac{\partial}{\partial y} & 0 \\ 0 & 0 & \frac{\partial}{\partial z} \\ \frac{\partial}{\partial y} & \frac{\partial}{\partial x} & 0 \\ 0 & \frac{\partial}{\partial z} & \frac{\partial}{\partial y} \\ \frac{\partial}{\partial z} & 0 & \frac{\partial}{\partial x} \end{bmatrix} \begin{Bmatrix} u \\ v \\ w \end{Bmatrix} \tag{7.11}$$

7.2.3. Elasticity

The relationship between stresses and strains is generally expressed in the material model. Hook's law gives this relation for an isotropic elastic model:

$$\begin{Bmatrix} \sigma_x \\ \sigma_y \\ \sigma_z \\ \tau_{xy} \\ \tau_{yz} \\ \tau_{zx} \end{Bmatrix} = \frac{E}{(1-2\nu)(1+\nu)} \begin{bmatrix} 1-\nu & \nu & \nu & 0 & 0 & 0 \\ \nu & 1-\nu & \nu & 0 & 0 & 0 \\ \nu & \nu & 1-\nu & 0 & 0 & 0 \\ 0 & 0 & 0 & \frac{1}{2}-\nu & 0 & 0 \\ 0 & 0 & 0 & 0 & \frac{1}{2}-\nu & 0 \\ 0 & 0 & 0 & 0 & 0 & \frac{1}{2}-\nu \end{bmatrix} \begin{Bmatrix} \varepsilon_x \\ \varepsilon_y \\ \varepsilon_z \\ \gamma_{xy} \\ \gamma_{yz} \\ \gamma_{zx} \end{Bmatrix} \tag{7.12}$$

or:

$$\{\sigma\} = [E]\{\varepsilon\} \tag{7.13}$$

The elastic material stiffness is denoted as $[E]$. Two parameters are used in Eq. (7.12), E is Young's modulus of material, and ν is Poisson's ratio. The relationship between Young's modulus, E, and other stiffness moduli, such as the shear modulus, G, and the bulk modulus, K, are given by:

$$G = \frac{E}{2(1+\nu)};\ K = \frac{E}{3(1-\nu)} \tag{7.14}$$

7.2.4. Elasto-Plastic Rate Integration of Differential Plasticity Models

According to the classical theory of plasticity, the strains can be decomposed into an elastic part and plastic part when stress state reaches yield surface:

$$\begin{aligned}\{d\varepsilon\} &= \{d\varepsilon^e\} + \{d\varepsilon^p\} \\ \{d\varepsilon^e\} &= \{d\varepsilon\} - \{d\varepsilon^p\}\end{aligned} \tag{7.15}$$

The stress increments can be written based on Hook's law:

$$\begin{aligned}\{d\sigma\} &= [E^e]\{d\varepsilon^e\} \\ \{d\sigma\} &= [E^e](\{d\varepsilon\} - \{d\varepsilon^p\})\end{aligned} \tag{7.16}$$

In general, plastic strains are written as:

$$\{d\varepsilon^p\} = \lambda\left\{\frac{\partial g}{\partial \sigma}\right\} \tag{7.17}$$

in which λ is plastic multiplier, λ equals to zero if behavior is elastic, whereas in the case plastic behavior, λ is different to zero, λ can be calculated by Forward Euler's method or Backward Euler's method (Smith & Griffith, 1997).

According to Forward Euler's method:

$$\lambda = \frac{\left[\frac{\partial f}{\partial \sigma}\right][E^e]}{\left[\frac{\partial f}{\partial \sigma}\right][E^e]\left\{\frac{\partial g}{\partial \sigma}\right\}+h}\{d\varepsilon\} \tag{7.18}$$

Substitute Eq. (5.18) and Eq. (5.17) to Eq. (5.16):

$$\{d\sigma\} = \left([E^e] - \frac{[E^e]\left\{\frac{\partial g}{\partial \sigma}\right\}\left[\frac{\partial f}{\partial \sigma}\right][E^e]}{\left[\frac{\partial f}{\partial \sigma}\right][E^e]\left\{\frac{\partial g}{\partial \sigma}\right\}+h}\right)\{d\varepsilon\} \tag{7.19}$$

According to Backward Euler's method:

$$\lambda = \frac{f_{(\sigma)}}{\left[\frac{\partial f}{\partial \sigma}\right][E^e]\left\{\frac{\partial g}{\partial \sigma}\right\}+h} \tag{7.20}$$

Substitute Eq. (7.20) and Eq. (7.19) to Eq. (7.16):

$$\{d\sigma\} = [E^e]\{d\varepsilon\} - \frac{f_{(\sigma)}[E^e]\left\{\frac{\partial g}{\partial \sigma}\right\}}{\left[\frac{\partial f}{\partial \sigma}\right][E^e]\left\{\frac{\partial g}{\partial \sigma}\right\}+h} \tag{7.21}$$

where f is yield function and g is potential function. The symbol h denotes the hardening parameter, which is zero for perfectly-plastic models and constant for linear hardening models.

The derivative of yield functions that used in Eq. 7.21:

$$\left\{\frac{\partial f_i}{\partial \sigma}\right\} = \frac{\partial f_i}{\partial I_1}\left\{\frac{\partial I_1}{\partial \sigma}\right\} + \frac{\partial f_i}{\partial J_2}\left\{\frac{\partial J_2}{\partial \sigma}\right\} + \frac{\partial f_i}{\partial \theta}\left\{\frac{\partial \theta}{\partial \sigma}\right\} \tag{5.22}$$

7.3. Modified Ramberg-Osgood Model

7.3.1. Governing equations

Ramberg-Osgood (RO) is the nonlinear model used to describe the stress-strain behavior of soil under cyclic loading. The hyperbolic shape of this model's curve can be described by equations (Fig. 7.23):

$$\begin{aligned}\frac{\gamma}{\gamma_r} &= \frac{\tau}{\tau_r} + \alpha\left|\frac{\tau}{\tau_r}\right|^r \text{ for } \gamma \geq 0, \\ \frac{\gamma}{\gamma_r} &= \frac{\tau}{\tau_r} - \alpha\left|\frac{\tau}{\tau_r}\right|^r \text{ for } \gamma < 0\end{aligned} \tag{7.23}$$

where γ is shear strain; τ is shear stress; γ_r is reference shear strain; τ_r is reference stress; α is stress coefficient, and $\alpha \geq 0$ and $r \geq 1$ is a constant.

Note that $\frac{\tau_r}{\gamma_r} = G_0$, where G_0 is the shear modulus at very small strain. The stress coefficient, α, used to adjust the position of the stress-strain curve and the stress exponent, r, can control the curvature of the curve.

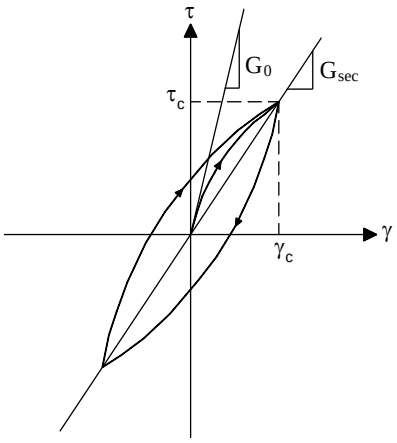

Figure 7-1 Shear Modulus at Very Small Strain and Secant Modulus (Kramer, 1996)

Equation (7.23) can be rearranged by:

$$\frac{\gamma}{\tau} = \frac{\gamma_r}{\tau_r} + \alpha \frac{\gamma_r}{\tau_r} \left|\frac{\tau}{\tau_r}\right|^{r-1} = \frac{1}{G_0}\left(1 + \alpha \left|\frac{\tau}{\tau_r}\right|^{r-1}\right) \qquad (7.24)$$

For the implementation of a RO model in three dimensions, the original RO equation will be changed in which the reference shear stress is replaced by shear strength of soil. The α value in original RO model needs to be multiplied by factor of shear strength and reference shear stress when it is used in new equation then α becomes

$\bar{\alpha} = \alpha\left(\frac{\tau_f}{\tau_r}\right)$.

For triaxial test, shear stress and ultimate shear stress in Eq. (7.24) can be written in the form of main stress as:

$$2\frac{\gamma_{oct}}{\tau_{oct}} = \frac{1}{G_0}\left(1 + \bar{\alpha}\left(\frac{\tau_{oct}}{(\tau_{oct})_f}\right)^{r-1}\right) \qquad (7.25)$$

or

$$2\gamma_{oct} = \frac{\tau_{oct}}{G_0}\left(1 + \bar{\alpha}\left|\frac{\tau_{oct}}{(\tau_{oct})_f}\right|^{r-1}\right) = \frac{\sqrt{2J_2}}{\sqrt{3}G_0}\left(1 + \bar{\alpha}\left(\frac{\sqrt{J_2}}{(\sqrt{J_2})_f}\right)^{r-1}\right) \qquad (7.26)$$

According to Mohr-Coulomb criterion, the second deviatoric invariant at failure is defined as:

$$\left(\sqrt{J_2}\right)_f = \frac{\frac{I_1}{3}\sin\phi - c\cos\phi}{\frac{\sin\theta\sin\phi}{\sqrt{3}} - \cos\theta} \qquad (7.27)$$

From the relationship between total strain, elastic strain and plastic strain, $\gamma^p_{oct} = \gamma_{oct} - \gamma^e_{oct}$ and $\gamma^e_{oct} = \frac{\tau_{oct}}{2\beta G_0}$, Eq. (7.27) can be written in the form of a yield surface:

$$f_1 = \left(\sqrt{J_2} - \left(\sqrt{J_2}\right)_0\right)\left((\beta - 1)\left(\left(\sqrt{J_2}\right)_f - \left(\sqrt{J_2}\right)_0\right)^{r-1} + \bar{\alpha}\beta\left(\sqrt{J_2} - \left(\sqrt{J_2}\right)_0\right)^{r-1}\right) - \cdots \qquad (7.28)$$
$$\sqrt{6}G_0\beta\left(\left(\sqrt{J_2}\right)_f - \left(\sqrt{J_2}\right)_0\right)^{r-1}\gamma^p_{oct}$$

$$f_2 = \bar{\alpha}\left(\left(\sqrt{J_2}\right)_0 - \sqrt{J_2}\right)^r - \sqrt{6}G_0\beta\left(\left(\sqrt{J_2}\right)_f + \left(\sqrt{J_2}\right)_0\right)^{r-1}\left(\left(\gamma_{oct}^p\right)_0 - \gamma_{oct}^p\right) f_2 = \bar{\alpha}\left(\left(\sqrt{J_2}\right)_0 - \sqrt{J_2}\right)^r - \sqrt{6}G_0\beta\left(\left(\sqrt{J_2}\right)_f + \left(\sqrt{J_2}\right)_0\right)^{r-1}\left(\left(\gamma_{oct}^p\right)_0 - \gamma_{oct}^p\right) \quad (7.29)$$

For reloading, the yield function can be rewritten as:

$$f_3 = \bar{\alpha}\left(\sqrt{J_2} - \left(\sqrt{J_2}\right)_0\right)^r - \sqrt{6}G_0\beta\left(\left(\sqrt{J_2}\right)_f - \left(\sqrt{J_2}\right)_0\right)^{r-1}\left(\gamma_{oct}^p - \left(\gamma_{oct}^p\right)_0\right) \quad (7.30)$$

For unloading but increase plastic strain, the yield function can be rewritten as:

$$f_4 = \bar{\alpha}\left(\left(\sqrt{J_2}\right)_0 - \sqrt{J_2}\right)^r - \sqrt{6}G_0\beta\left(\left(\sqrt{J_2}\right)_f + \left(\sqrt{J_2}\right)_0\right)^{r-1}\left(\gamma_{oct}^p - \left(\gamma_{oct}^p\right)_0\right) \quad (7.31)$$

For reloading but decrease plastic strain, the yield function can be rewritten as:

$$f_5 = \left(\sqrt{J_2} - \left(\sqrt{J_2}\right)_0\right)^r \bar{\alpha} - \sqrt{6}G_0\beta\left(\left(\sqrt{J_2}\right)_f - \left(\sqrt{J_2}\right)_0\right)^{r-1}\left(\left(\gamma_{oct}^p\right)_0 - \gamma_{oct}^p\right) \quad (7.32)$$

where $\left(\sqrt{J_2}\right)_0$ and $\left(\gamma_{oct}^p\right)_0$ are second deviatoric invariant and octahedral plastic strain, respectively, at turning points as shown in Figure 7-2.

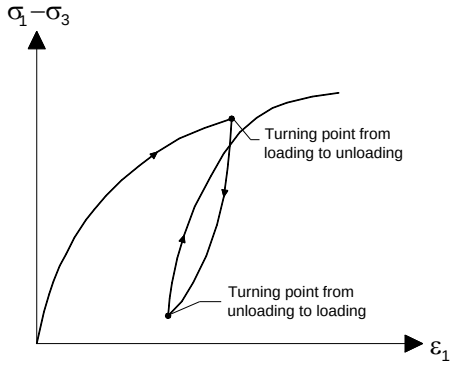

Figure 7-2 Unloading-Reloading Behavior

7.3.2. Stress increment

The backward Euler method (Smith and Griffith 2004) is applied to determine the shear stress increment. Consider an illegal stress state at point B (Figure7-3), the stress state at a point C on the yield surface is computed from the first order Taylor expansion of the yield function at point B as:

$$f_{(C)} = f_{(B)} + \frac{\partial f_{(B)}}{\partial \tau} d\tau + \frac{\partial f_{(B)}}{\partial \gamma_{oct,p}} d\gamma_{oct,p} \quad (7.33)$$

By enforcing consistency of the yield function at point C:

$$f_{(B)} + \frac{\partial f_{(B)}}{\partial \tau}\left(-\lambda G_0 \frac{\partial g_{(B)}}{\partial \tau}\right) + \lambda \frac{\partial f_{(B)}}{\partial \gamma_{oct,p}} \frac{\partial g_{(B)}}{\partial \tau_{oct}} = 0 \quad (7.34)$$

The plastic scalar can be obtained from Eq. (17) as:

$$\lambda = \frac{f_{(B)}}{\frac{\partial f_{(B)}}{\partial \tau} G_0 \frac{\partial g_{(B)}}{\partial \tau} - \frac{\partial f_{(B)}}{\partial \gamma_{oct,p}} \frac{\partial g_{(B)}}{\partial \tau_{oct}}} \quad (7.35)$$

The following expression is given for the stress increment:

$$d\tau = G_0\left(d\gamma - d\gamma_p\right) = G_0\left(d\gamma - \lambda \frac{\partial g_{(B)}}{\partial \tau}\right) \quad (7.36)$$

Introducing Eq. (18) to Eq. (19) results in:

$$d\tau = G_0\left(d\gamma - \frac{f_{(B)}}{\frac{\partial f_{(B)}}{\partial \tau}G_0\frac{\partial g_{(B)}}{\partial \tau} - \frac{\partial f_{(B)}}{\partial \gamma_{oct,p}}\frac{\partial g_{(B)}}{\partial \tau_{oct}}}\frac{\partial g_{(B)}}{\partial \tau}\right) \tag{7.37}$$

The increment of the plastic strain is determined as:

$$d\gamma_p = \frac{f_{(B)}}{\frac{\partial f_{(B)}}{\partial \tau}G_0\frac{\partial g_{(B)}}{\partial \tau} - \frac{\partial f_{(B)}}{\partial \gamma_{oct,p}}\frac{\partial g_{(B)}}{\partial \tau_{oct}}}\frac{\partial g_{(B)}}{\partial \tau} \tag{7.38}$$

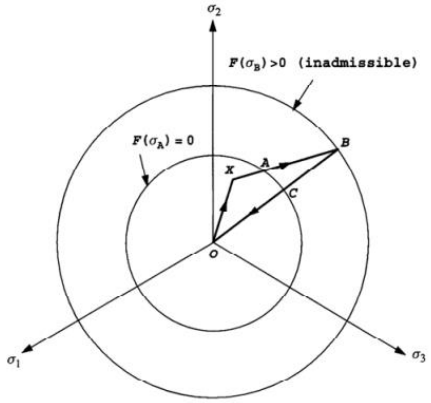

Figure 7-3 Stress correction

7.3.3. Parameter Determination of Modified Ramberg-Osgood Model

The parameters of modified Ramberg-Osgood model are given in Table 7-1.

The Young's modulus at small strain computed from shear modulus at small strain and Poisson's ratio.

Table 7-1: Material parameter for the modified Ramberg-Osgood model

Parameter	Description
E_0	Young's modulus at very small strain
ν	Poisson's ratio
α	Stress coefficient
r	Stress exponent

The shear modulus at very small strain related to shear wave velocity and mass density of the soil by following equation:

$$G_0 = \rho V_s^2 \tag{7.39}$$

The other parameters of modified Ramberg-Osgood material model can be determined from laboratory test.

By rearranging Eq. (7.23), the tangent shear modulus for the backbone curve can be expressed as:

$$G_t = \frac{\partial \tau}{\partial \gamma} = \frac{\tau_r}{\gamma_r}\left(\frac{1}{1+\alpha r\left|\frac{\tau}{\tau_r}\right|^{r-1}}\right) \tag{7.40}$$

For very small strain, i.e., $\gamma \to 0$ and $\tau \to 0$, because $r > 1$,

$$(G_t)_{\gamma=0} = G_0 = \frac{\tau_r}{\gamma_r} \tag{7.41}$$

Then the backbone relation can be rewritten as:

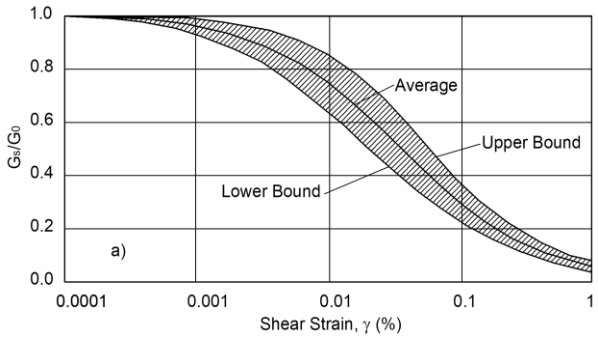

Figure 7-4 Variation of Shear Modulus with Shear Strain for Sands Seed and Idriss (1970)

$$\frac{\gamma}{\gamma_r} = \frac{\tau}{G_0\gamma_r}\left(1 + \alpha r \left|\frac{\tau}{G_0\gamma_r}\right|^{r-1}\right) \tag{7.42}$$

Hence, besides G_0, there are three other parameters (γ_r, α, and r) left to be determined for the modified Ramberg-Osgood model. By substituting $\tau = G_{sec}\ \gamma$ and rearranging Eq. (7.40), one gets the following equation:

$$\frac{G_0}{G_{sec}} - 1 = \alpha r \left|\frac{G_{sec}\ \gamma}{G_0\gamma_r}\right|^{r-1} \tag{7.43}$$

By applying logarithm to both side of Eq. 7.37, one obtains:

$$log\left(\frac{G_0}{G_{sec}} - 1\right) = log\, r\, \alpha + (r-1)\, log\left(\frac{G_{sec}\ \gamma}{G_0\gamma_r}\right) \tag{7.44}$$

From Eq. (7.44), with an assumed value for the reference shear strain γ_r and the experimental modulus reduction curve (Figure 7-4), the values of α and r can be determined from the intercept and the slope, respectively, of the best fit straight line shown in Figure 7-5.

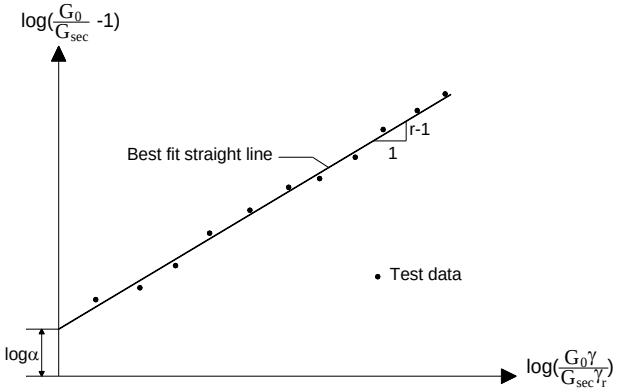

Figure 7-5 Example of a Best Fit Straight Line for Determining Parameters α and r (after Ueng and Chen, 1992)

The value of the reference shear strain γ_r can affect the shape of the backbone curve and the hysteresis loop. γ_r can be refined through an iteration procedure listed in the following:

Assume a value for γ_r and obtain the values of α and r by plotting the data according to Eq. (7.44).

Compute γ_y according to Eq. (7.42) from the given modulus reduction and obtain an average value of γ_r.

Compare the new value of γ_r with the previous value. Repeat steps 1 and 2 if the difference is too large.

Finally, the reference shear stress τ_r can be calculated using Eq. (7-41).

7.4. Undrained Cyclic Triaxial Test Simulation

For undrained triaxial test conditions, $\Delta\varepsilon_p = 0$, therefore the constitutive equation (Eq. (7-21)) may be solved by applying a known increment of total strain, $\Delta\boldsymbol{\varepsilon}$, the procedure for undrained triaxial test simulation is described in the following:

1. Specify an increment of total axial strain, $\Delta_{\varepsilon z}$, to be applied in the current step;

For undrained triaxial test conditions: $\gamma_{xy} = \gamma_{yz} = \gamma_{zx} = 0$ and $\Delta\varepsilon_p = 0$; therefore

$$\Delta\varepsilon_x = \Delta\varepsilon_y = -0.5\Delta\varepsilon_z;$$

2. Initialize state variables (e.g. σ_0, σ_c', σ_s, σ_d,, c, φ, μ, β, α, E_0, K, G, etc.);

3. Enter the stress update algorithm with the current stress state, σ_0, hardening modulus, h, and specified increment of total strain, $\Delta\boldsymbol{\varepsilon}$;

4. Solve the constitutive equation using the backward Euler method Smith and Griffith (2004) is applied to determine the shear stress increment to obtain the updated stress state, $\Delta\sigma$, and hardening modulus, h, at the end of the current strain increment;

5. Update state variables for new stress state;

6. Repeat steps 3 to 5 for the next increment of total strain.

+ Calculate strain increments		$\{\Delta\varepsilon\} = [\Delta\varepsilon_z, -0.5\Delta\varepsilon_z, -0.5\Delta\varepsilon_z, 0, 0, 0]^T$
+ Calculate stresses:	Elastic	$\{\sigma^{th}\} = \{\sigma_{ep}^{i-1}\} + [E^e]\{\Delta\varepsilon\}$
	Constitutive	$\{\sigma_{ep}^{i}\} = \{\sigma^{th}\} - \frac{f(\sigma^{th})}{\left[\frac{\partial f}{\partial\sigma}\right][E^e]\left\{\frac{\partial g}{\partial\sigma}\right\}+h}[E^e]\left\{\frac{\partial g}{\partial\sigma}\right\}$
		$h = -\frac{\partial f}{\partial\gamma}\frac{\partial\gamma}{\partial\lambda}$

By using the Delphi programming language, the undrained cyclic triaxial test was simulated based on Modified Ramberg- Ogood formulations as shown in Figure 7-6.

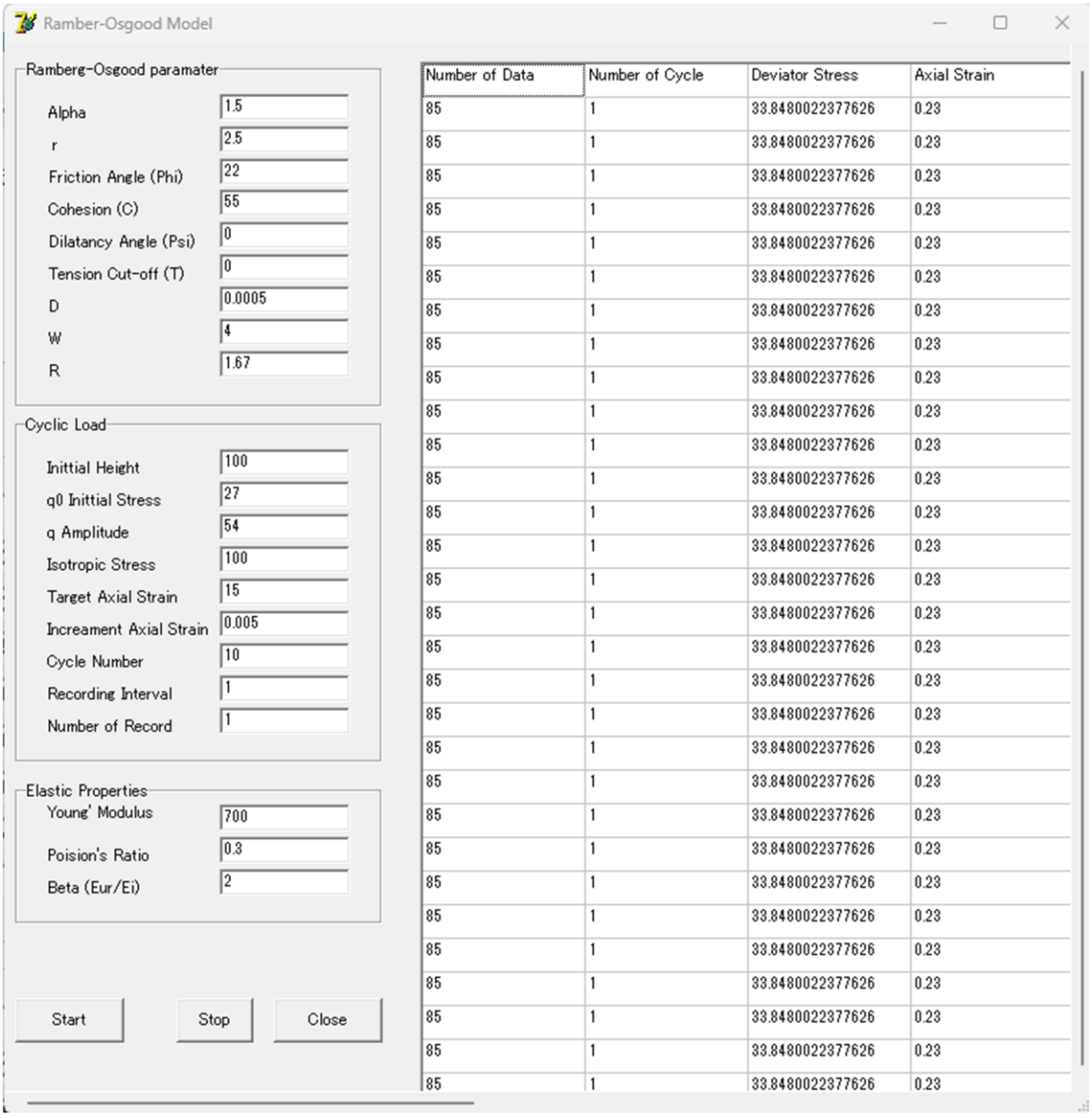

Figure 7-6 Undrained cyclic triaxial test simulation

7.5. Validation of cyclic test model

In order to verify the test model, the dynamic parameters of Ramberg-Osgood are proposed as follow.

E_0 = 180 MN/m^2, ν = 0.49, α = 1.5, r = 3.

7.5.1. Undrained cyclic triaxial Tests – nonsymmetrical loading (one-way loading)

Figure 7-7 shows the undrained cyclic triaxial model simulations considering one-way loading, compared against experimental data (test C34, described in Chapter 6). It is clear show that the models are able to capture the general trends observed in the test data and reasonable prediction of magnitude of stiffness modulus of LSS mixed fiber. However, the model performs poorly in terms of reproducing the shape of the stress-strain curves, and significantly overpredict the magnitude and rate of accumulation of vertical strain.

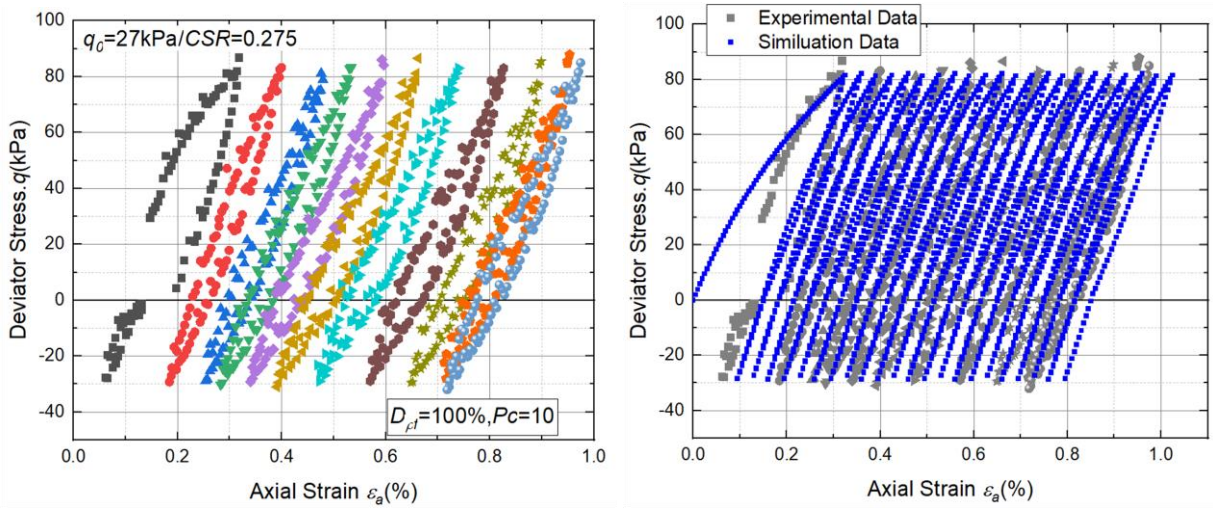

Figure 7-7 Comparison of model predictions with undrained, one-way loading, cyclic triaxial test (C34)

7.5.2. Undrained cyclic triaxial Tests –symmetrical loading (two-way loading)

Figure 7-8 shows the undrained cyclic triaxial model simulations considering two-way loading, compared against experimental data (test C20, described in Chapter 6). The model fails to capture the shape of the stress-strain curves, particularly with respect to the accumulation of double vertical strain observed in the test data. As a same to the one-way loading test, the models are able to capture the general trends observed in the test data and reasonable prediction of magnitude of stiffness modulus of LSS mixed fiber.

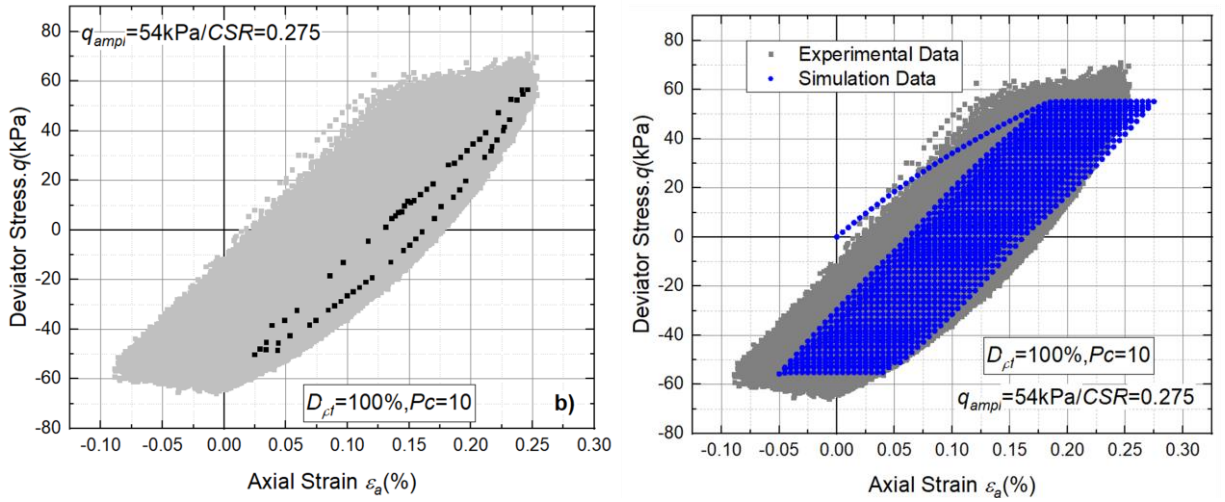

Figure 7-8 Comparison of model predictions with undrained, one-way loading, cyclic triaxial test (C20)

7.6. Summary

Considering what exposed, one may consider that the Ramberg-Osgood model was successfully implemented in Delphi code. A full theoretical constitutive model was exposed.

The comparisons of model simulations with experimental data for both cases one-way and two-way cyclic loading indicate that the models are able to capture the general trends observed in the test data and reasonable prediction of magnitude of stiffness modulus of LSS mixed fiber. However, the model performs poorly in terms of reproducing the shape of the stress-strain curves, and significantly overpredict the magnitude and rate of accumulation of vertical strain.

The relatively poor model predictions obtained in the undrained test simulations may be a result of the calibrated model parameters are determined predominantly from experimental tests. To overcome these issues, the practical process for calibration of parameter model should be done in further work.

In conclusion, the overall is able to apply the Ramberg-Osgood model to evaluate the cyclic behavior of LSS and dynamic parameters will be calibrated properly.

CHAPTER 8

CONCLUSIONS AND RECOMMENDATION

8. Conclusions and Recommendation

In this study, the mechanical behavior of reinforced and unreinforced Liquefied Stabilized Soil (LSS) subjected to monotonic and cyclic loading is discussed based on a database with about 102 Consolidated-Undrained monotonic and cyclic triaxial tests. From the test results, the main findings can be revealed as follow.

8.1. The Effect of Fiber Material, Slurry Density, and Curing Time on Monotonic Behavior of LSS Cured at Laboratory and In-situ (Chapter 5).

In the monotonic tests, the influences of slurry density and curing time on the strength and deformation of LSS are investigated. Also, LSS mixed with the pulverized newspaper in the amount of 0 and 10 kg/m^3 cured laboratory and in-situ are compared and investigated. Based on the results of a series of undrained triaxial compression tests, the following conclusions on the strength and deformation properties of LSS prepare by various conditions were obtained.

1) The slurry density had a considerable effect on the strength of LSS, with increasing density resulting in a 40 % rise in value of q_{max} and lowering density resulting in a 20 % drop in value of q_{max} when the density was changed at the same rate.

2) According to the brittleness index, the brittle properties of LSS were improved significantly about twice by adding fiber material.

3) The relationship between the $\log(q_{max})$ and $\log(t)$ is linear. It seems that $q_{max}=a\times(t)^n$ is approved to the relation between q_{max} and curing time, t of cement-treated soil including LSS.

4) In case of in-situ curing, the effect of curing time on the increasing rate of strength is small when compared to LSS without fiber material cured laboratory. The appearance of cementation was considered to be delayed due to adding fiber material and increasing water content at in-situ.

5) The relationship of $E_0\cong1000\sim3000\times q_{max}$ and $E_{50}\cong600\sim1100\times q_{max}$ irrespective of slurry density and curing time in almost cases is approved to the relationship between E_0 and q_{max} of cement-treated soil including LSS.

6) The effect of curing time on the initial Young's modulus, E_0, is smaller than the effect of slurry density with LSS cured in-situ. In particular, the E_0 value is more sensitively changed by the slurry density with LSS cured laboratory.

7) The slurry density has a substantial influence on the stress-strain relationships of LSS with fiber material cured in-situ**.** With increasing slurry density, the pre-failure stress-strain relation becomes more non-linear and the post-peak stress-strain relation becomes more ductile, while q_{max} decreases slightly. Furthermore, the influence of shear stress level on the degree of damage appears to be independent of slurry density.

8) By adding fiber material into LSS cured in-situ, the non-linearity of pre-failure $q\sim\varepsilon_a$ curve seems to become rather independent of curing time, the effect of curing time on the post-peak deformation is negligible, while the effect of curing time on the degree of damage is found to be largely due to a decrease in the viscous component of deformation and an increase of the elastic component of strain.

9) Since uncontrolled environmental factors make it much more difficult to predict the strength and deformation behavior of LSS cured in-situ. It is considered necessary to conduct further work that controls more factors influencing specimens

8.2. Cyclic Behavior of Reinforced and Unreinforced LSS Cured Laboratory (Chapter 6)

In the cyclic tests, in order to investigate the effect of cyclic load on the deformation property, the deviator stress amplitude, the initial stress, consolidation pressure, strain rate, and the control method (stress vs. strain cycles) were changed and LSS material which includes slurry density, fiber material, and cement on LSS cured 28 days at the laboratory have been also varied. Based on the results, the conclusions of 54 undrained monotonic and cyclic triaxial tests undertaken on reinforced and unreinforced LSS were drawn.

1) The monotonic tests with different initial pressures primarily served to provide the critical state lines used as a reference for the analysis of the cyclic tests.
2) In the cyclic tests, the excess pore water pressure continuously increases and simultaneously decreases the effective stresses with increasing number of cycles. The sample becomes weaker with the cycle number and accumulated axial strain increases gradually.
3) The failure mode is highly dependent on the cyclic deviator stress amplitude (σ_d) and initial deviator stress (σ_s). For symmetrical loading (σ_s = 0), the pore water pressure and double axial strain amplitude grew with an increasing number of cycles and deviator stress amplitude. LSS mixed fiber material finally failed due to too large strain amplitudes (a failure criterion of ε_1 = 2.5 % was used in all tests). The true liquefaction ($q = p' = 0$) did not reach in LSS. In the final stage, the effective stress loops loop passes a "Butterfly" stress path shape, and the distance of the final stress loop is smaller than to the origin with lower stress amplitude.
4) For nonsymmetrical loading (σ_s > 0), an accumulation of compressional axial strain with each subsequent cycle occurred, while the mobilized double axial strain remaining almost constant. Therefore, the failure criterion was fulfilled due to an excessive accumulation of permanent strains (a failure criterion of ε_1 = 10 %). In contrast to the tests with symmetrical loading, the accumulated pore pressure increases from the first cycle up to maximum value and, after that, decreases quickly to failure while the axial strain progressively grows in each subsequent cycle. This caused the effective stress loops to migrate to pass over the CSL, then return to the touch again of the failure envelope, and the shape of the stress loop at the final stage did not pass the "butterfly" shape or lens shape. As a result, LSS mixed fiber material tends to dilate before reaching the failure criterion.
5) Increasing initial stress can improve the resistance of the material, by 'shifting' the stress path up in $p' - q$ space and, thus, further away from the extension failure envelope. As a result, the cyclic resistance of LSS mixed fiber increase significantly when increasing initial stress σ_s.
6) There is a threshold value of the stress level *CSR* between 0.275 to 0.344. If the stress level is higher than that value, the LSS cyclic behavior is more contractive and reaches the failure criterion by excessing the double axial strain amplitude; otherwise, the LSS sample is more dilative by the accumulation of permanent axial strain and did not reach to the failure.
7) An increase of deviator stress amplitude and initial stress drastically reduces the number of cycles to reach failure conditions and simultaneously equivalent Young's modulus decrease remarkable, while hysteresis damping factor increase significantly with cycle number and cyclic strain level.
8) For smaller stress levels and low initial stress (*CSR* <0.275), the equivalent Young's modulus started to decrease at the beginning of the tests and then increased until the end of the tests. That means the LSS mixed fiber softened at the beginning, then hardened.

9) In the tests with symmetrical loading, the rate of pore pressure accumulation grew with increasing stress or strain amplitude, while it was reduced with increasing values of initial mean pressure. Therefore, increasing initial mean pressures σ_c' leads to increasing cyclic resistance. In contrast, reducing the initial mean pressure significantly decreases the number of cycles N_f required to reach the failure criterion.
10) Under a lower displacement rate, the strength of the sample reduces more quickly than under a higher displacement rate with each subsequent cycle. The stress-strain becomes more nonsymmetrical and tends to enlarge in compression mode, revealing that the compression strength is weaker than when applying a cyclic test with a low displacement rate.
11) The effect of fiber material, slurry density, and cement content on LSS cyclic behavior are significant.
12) Adding fiber material into LSS significantly reduces dissipated strain energy and is more resistant to deformation. It causes the cyclic stress-strain behavior to be more symmetrical than in the case of unreinforced fiber, which means the cyclic strength improves substantially.
13) With LSS without fiber and decreasing slurry density and cement content, the rate of accumulated pore water pressure and axial strain increases rapidly with the number of cycles. In addition, the degradation index and the number of cycles required for the failure also reduce remarkably.
14) The accumulated plastic strain and energy loss factor increase remarkably when increasing cyclic stress level *CSR*, increasing initial stress σ_s, and decreasing slurry density, initial mean pressure, cement content, and displacement rate, respectively.
15) Compared to adding fiber, cement content reduction's influence on reducing the cyclic strength of LSS seems more remarkable.
16) The hysteresis damping factor decreases at the beginning of loading during ten cycles and reveals a U-shaped damping ratio cluster in most cases that approach failure. It can be explained the response of the stress-strain behavior of LSS during the first few cycles are highly elastic. Which cause dissipated strain energy to decrease and progressively increase stored strain energy.
17) All tests show that the deviator stress decreases suddenly after the first cycle in strain-controlled cyclic tests and the effective stress paths move to the CSL and exhibit a “fir tree” shape similar to those observed in tests on the sand.
18) Tests at the cyclic test and material variables showed patterns of behavior that could be captured by empirical equations allowing the strains, stiffness, and damping ratios to be predicted under given numbers of cycles and specified cyclic loading conditions.
19) The data in this thesis serve for the examination, calibration, or improvement of constitutive models dedicated to reinforced LSS under cyclic loading, or for the development of new models.

8.3. Constitutive Model (Chapter 7)

The purpose of this chapter is the implementation of a numerical simulation route for the modified Ramberg-Osgood model using the Delphi programming language to verify the behavior of reinforced LSS under undrained cyclic triaxial tests. For this purpose, the undrained cyclic triaxial test model is simulated by the modified Ramberg-Osgood formulations and compared with experimental test results. From the result of comparison of model simulations with experimental data, the conclusions were obtained.

1) The comparisons of model simulations with experimental data for both cases one-way and two-way cyclic loading indicate that the models are able to capture the general trends observed in the test data and reasonable prediction of magnitude of stiffness modulus of LSS mixed fiber. However, the model performs poorly in terms of reproducing the shape of the stress-strain curves, and significantly overpredict the magnitude and rate of accumulation of vertical strain.
2) The relatively poor model predictions obtained in the undrained test simulations may be a result of the calibrated model parameters are determined predominantly from experimental tests. To overcome these issues, the practical process for calibration of parameter model should be done in further work.
3) In conclusion, the overall is able to apply the Ramberg-Osgood model to evaluate the cyclic behavior of LSS and dynamic parameters will be calibrated properly.

8.4. Recommendations

Based on the testing and conclusions, the following recommendation are made:

1) The research on the cyclic behavior of reinforced and unreinforced LSS cured in-situ with influence of curing time was proposed in future work.
2) The improvement of using local deformation transducers (LDTs) to measure axial strain should be done for all LSS sample in next research.
3) The shape of cyclic loading will be update with sinusoidal shape.
4) The results of FEM analysis depend on the constitutive models used, and the model parameters adopted in the numerical analyses. The practical process for calibration of parameter model should be done in next study.
5) Improvement and calibration of the Rambeg-Osgood model for LSS mixed fiber to compare and verify with current software such as Plaxis and Abacus.

REFERENCES

Andersen, K. H., Kleven, A., & Heien, D. (1988). Cyclic soil data for design of gravity structures. Journal of Geotechnical Engineering, 114(5), 517–539.

Ansal, A. M., & Erken, A. (1989). Undrained behavior of clay under cyclic shear stresses. Journal of Geotechnical Engineering, 115(7), 968–983.

Andersen, K. H. (2015). Cyclic soil parameters for offshore foundation design - The Third ISSMGE McClelland Lecturer. In V. Meyer (Ed.), Proceedings of the 3rd International Symposium on Frontiers in Offshore Geotechnics (ISFOG 2015), Oslo, Norway, 10-12 June 2015 (pp. 5–82). CRC Press.

Boominathan, A. and Hari, S., (2002). "Liquefaction strength of fly ash reinforced with randomly distributed fibers." Soil Dynamics and Earthquake Engineering, 22(9), pp.1027-1033.

Boulanger, R. W., & Idriss, I. M. (2006). Liquefaction susceptibility criteria for silts and clays.

Biarez, J., Hicher P.Y. (1994). "Elementary mechanics of soil behaviour: saturated remoulded soils." A.A.Balkema Publishers, Rotterdam.

Chegenizadeh, A., M. Keramatikerman, and Nikraz, H. (2018). "Liquefaction resistance of fiber reinforced low-plasticity silt." Soil Dynamics and Earthquake Engineering, 104, pp.372-377.

Clough, G. W., Iwabuchi, J., Rad, N. S., & Kuppusamy, T. (1989). "Influence of cementation on liquefaction of sands." Journal of Geotechnical Engineering, 115(8), 1102-1117.

Dobry, R., Ladd, R. S., Yokel, F. Y., Chung, R. M., & Powell, D. (1982). Prediction of Pore Water Pressure Buildup and Liquefaction of Sands During Earthquakes By the Cyclic Strain Method. NBS Building Science Series 138. Washington.

Goto, S., Tatsuoka, F., Shibuya, S., Kim, Y-S., and Sato, T. (1991) A simple gauge for local small strain measurements in the laboratory, Soils and Foundations, Vol.31, No.1, pp.169-180.

Horpibulsuk, S., Miura, N., Bergado, D.T. (2004). Undrained shear behavior of cement admixed clay at high water content, Journal of Geotechnical and Geoenvironmental Engineering, Vol.130, No.10, pp.1096-1105.

Hong, Y., Yang, Z., Orense, R. P., and Lu, Y. (2015). "Investigation of Sand-Tire Mixtures as Liquefaction Remedial Measure." Proceedings of the Tenth Pacific Conference on Earthquake Engineering Building an EarthquakeResilient Pacific., Sydney, Australi.

Hamidi, A. and Hooresfand, M. (2013). "Effect of fiber reinforcement on triaxial shear behavior of cement treated sand." Geotextiles and Geomembranes, 36, pp.1-9.

Haeri, S. M., Noorzad, R. and Oskoorouchi, A. M. (2000). "Effect of geotextile reinforcement on the mechanical behavior of sand." Geotextiles and Geomembranes, 18(6), pp.385-402.

Hicher P.Y. (1979). "Contribution à l'étude de la fatigue des argiles." Thèse de docteur-ingénieur, L'école Centrale des Arts et Manufactures.

Hyodo, M., Sugiyama, M., Yasufuku, N., Murata, H., and Kawata, Y. (1993) Cyclic shear behaviour of clay subjected to initial shear stress. Technical Report 2.

Hyodo, M., Yamamoto, Y., and Sugiyama, M. (1994). Undrained cyclic shear behaviour of normally consolidated clay subjected to initial static shear stress. Soils and Foundations, 34(4):1-11.

Ibraim, E., Diambra, A., Wood, D. M. and Russell, A. R. (2010). "Static liquefaction of fibre reinforced sand under monotonic loading." Geotextiles and Geomembranes, 28(4), pp.374-385.

Japanese Geotechnical Society, Committee Report Chapter 2, 2.1, 2.2 on test methods and physical properties of cement-modified soil, Proc. of the symposium, 2005, pp.2-22, on the survey, design, construction, and properties evaluation methods of solidifying stabilized soil using cement and cement-treated soil (in Japanese).

Kohata, Y. (2006). Mechanical property of liquefied stabilized soil and future issues, Doboku Gakkai Ronbunshuu, F, Vol.62, No.4, pp.618-627 (in Japanese).

Kohata, Y., Ichikawa, M., Nguyen, C. Giang., and Kato, Y. (2007). Study of damage characteristics of liquefied stabilized soil mixed with fibered material due to triaxial shearing, Geosynthetics Engineering Journal, Vol.22, pp.55-62 (in Japanese).

Kohata, Y., Ito, K., and Koyama, Y. (2011). Effect of cement content on shear properties of liquefied stabilized soil reinforced by fiber material, Japanese Geotechnical Society Hokkaido Branch Technical Report Papers, Vol.26, pp.95-100 (in Japanese).

Kohata, Y., Jiang, G-L., Murata, O., and Tatsuoka, F. (1999). Elastic-properties-based modeling of non-linear deformation characteristics of gravels, Proc. Of the second Inter. Symposium on Pre-Failure Deformation Characteristics of Geomaterials-IS Torino 99, pp. 533-539.

Kuno, G., eds. (1997). Liquefied stabilized soil method-Recycling technology of construction-generated soil and mud, Gihodo publication (in Japanese).

Kaneko, T., Orense, R. P., Hyodo, M. and Yoshimoto, N. (2012). "Seismic response characteristics of saturated sand deposits mixed with tire chips." Journal of Geotechnical and Geoenvironmental Engineering, 139(4), pp.633-643.

Kramer, S. L. (1996). Geotechnical earthquake engineering.

Kim, T. C., & Novak, M. (1981). Dynamic properties of some cohesive soils of Ontario. Canadian Geotechnical Journal, 18(3), 371–389.

Larew, H. G. and Leonards, G. A. A strength criterion for repeated loads. In Proceedings of the 41st Annual Meeting of the Highway Research Board, pages 529{556, Washington, DC, 1962.

Liao, H. J., Huang, C. C., & Chao, B. S. (2003). "Liquefaction resistance of a colloid silica grouted sand." In Grouting and ground treatment (pp. 1305-1313).

Lee, K. H., & Seed, H. B. (1967). Cyclic stress conditions causing liquefaction of sand. Journal of the Soil Mechanics and Foundations Division, ASCE, 93(SM1), 47–70.

Mashiri, M. S., Vinod, J. S., and Sheikh, M. N. (2016). "Liquefaction Potential and Dynamic Properties of Sand-Tyre Chip (STCh) Mixtures," Geotechnical Testing Journal, 39(1), pp. 69-79.

Maheshwari, B.K., Singh, H.P. and Saran, S. (2012). "Effects of reinforcement on liquefaction resistance of solani sand." Journal of Geotechnical and Geoenvironmental Engineering, 138(7), pp.831-840.

Maher, M. H., Ro, K. S., & Welsh, J. P. (1994). "Cyclic undrained behavior and liquefaction potential of sand treated with chemical grouts and microfine cement (MC-500)." Geotechnical Testing Journal, 17(2), 159-170.

Matsui, T., Ohara, H., and Ito, T. (1980). Cyclic stress-strain history and shear characteristics of clay. Journal of the geotechnical Engineering Division, ASCE, 106(GT10):1101-1120.

Maheshwari, B.K., Singh, H.P. and Saran, S. (2012). "Effects of reinforcement on liquefaction resistance of solani sand." Journal of Geotechnical and Geoenvironmental Engineering, 138(7), pp.831-840.

Maher, M. H. and Ho, Y. C. (1993). "Behavior of FiberReinforced Cemented Sand Under Static and Cyclic Loads", Geotechnical Testing Journal, GTJODJ, Vol. 16, No. 3, September 1993, pp. 330-338.

Noorzad, R., and P. Fardad Amini. (2014). "Liquefaction Resistance of Babolsar Sand Reinforced with Randomly Distributed Fibers under Cyclic Loading." Soil Dynamics and Earthquake Engineering 66: 281-292.

Naeini, S. A., and N. Gholampoor. (2014). "Cyclic Behaviour of Dry Silty Sand Reinforced with a Geotextile." Geotextiles and Geomembranes 42 (6): 611-619.

Neaz Sheikh, M., Mashiri, M. S., Vinod, J. S. and Tsang, H. H. (2012). "Shear and compressibility behavior of sand–tire crumb mixtures." Journal of Materials in Civil Engineering, 25(10), pp.1366-1374.

Nielsen, S. D., Shajarati, A., Sørensen, K. W., & Ibsen, L. B. (2012). Behaviour of Dense Frederikshavn Sand During Cyclic Loading. Aalborg: Department of Civil Engineering, Aalborg University. DCE Technical Memorandum No. 15 Aalborg University, 1–9.

Nghiem MH (2009), Soil-pile-structure interaction effects on high rises under seismic shaking. Phd Thesis, University of Colorado Denver USA.

Peralta (2010). Proserpine K. Peralta. Dissertation: Investigations on the Behavior of Large Diameter Piles under Long-Term Lateral Cyclic Loading in Cohesionless Soil, 2010.

Rascol, E. (2009). Cyclic Properties of Sand: Dynamic Behaviour for Seismic Applications. PhD Thesis, École Polytechnique Fédérale de Lausanne.

Towhata, I. (2008). “Mitigation of liquefaction-induced damage.” In Geotechnical Earthquake Engineering (pp. 588-642). Springer Berlin Heidelberg.

Saxena, S. K., Reddy, K. R., & Avramidis, A. S. (1988). “Liquefaction resistance of artificially cemented sand.” Journal of Geotechnical Engineering, 114(12), 1395-1413.

Sangrey, D. A., Henkel, D. J., & Esrig, M. I. (1969). The effective stress response of a saturated clay soil to repeated loading. Canadian Geotechnical Journal, 6(3), 241–252.

Seed H.B., Lee K.L. (1966). “Liquefaction of saturated sands during cyclic loading conditions.” Journal of the Soil Mechanics and Foundations Division, American Society of Civil Engineers, 92(6): 105-134.

Uchimura, T., Chi, N., Nirmalan, S., Sato, T., Meidani, M. and Towhata, I. (2007). “Shaking table tests on effect of tire chips and sand mixture in increasing liquefaction resistance and mitigating uplift of pipe.” In Proceedings, international workshop on scrap tire derived geomaterials—opportunities and challenges, Yokosuka, Japan (pp.179-186).

Vercueil, D., Billet, P. and Cordary, D. (1997). “Study of the liquefaction resistance of a saturated sand reinforced with geosynthetics.” Soil Dynamics and Earthquake Engineering, 16(7-8), pp.417-425.

Vaid, Y ., & Chern, J. (1985). Cyclic and monotonic undrained response of saturated sands. In In Proceedings of Advances in the Art of Testing Soils under Cyclic Loading Conditions (pp. 120–147). Detroit.

Vaid, Y. P., & Thomas, J. (1994). Post-liquefaction behaviour of sand. In Proceedings 13th International Conference on Soil Mechanics and Foundation Engineering (Vol. 3, pp.144 1305–1310). New Delhi: AA BALKEMA.

Vucetic, M. (1994). Cyclic threshold shear strains in soils. Journal of Geotechnical Engineering, 120(12), 2208–2228.

Vucetic, M., & Dobry, R. (1988). Degradation of marine clays under cyclic loading. Journal of Geotechnical Engineering, 114(2), 133–149.

Vucetic, M., & Dobry, R. (1991). Effect of soil plasticity on cyclic response. Journal of Geotechnical Engineering, 117(1), 89–107.

Vucetic, M., Lanzo, G., & Doroudian, M. (1998). Damping at small strains in the cyclic simple shear test. Journal of Geotechnical and Geoenvironmental Engineering, 124(7), 585–594.

Zergoun, M., & Vaid, Y. P. (1994). Effective stress response of clay to undrained cyclic loading. Canadian Geotechnical Journal, 31(5), 714–727.

Zhou, J. and Gong, X. (2001). Strain degradation of saturated clay under cyclic loading. Canadian Geotechnical Journal, 38: 208-212.

Wichtmann T, Triantafyllidis T. (2016). An experimental database for the development, calibration, and verification of constitutive models for sand with a focus on cyclic loading. Part I: tests with monotonic loading and stress cycles. Acta Geotechnica 11(4):739–761.

Wichtmann T, Triantafyllidis T. (2016). An experimental database for the development, calibration, and verification of constitutive models for sand with a focus on cyclic loading. Part II: tests with strain cycles and combined cyclic and monotonic loading. Acta Geotechnica 11(4):763–774.

APPENDIX

Source Delphi Code for Simulation of Undrained Cyclic Triaxial Test.

```
procedure TFrmRO.TmrTimer(Sender: TObject);
var i,j,l,m:integer;
ccpi: real;z
myfile: textfile;
jur20: real;
begin
InvariantJ2Value(jur20,fur0);
if (rev1=0) and (rev1=1) then
begin
eps1[1]:= (sqrt(2/3)*sqrt(jur20)*(1+ps)/(beta*eei)+ gmotp1)*sqrt(2);
eps1[2]:= -0.5*(sqrt(2/3)*sqrt(jur20)*(1+ps)/(beta*eei)+ gmotp1)*sqrt(2);
eps1[3]:= -0.5*(sqrt(2/3)*sqrt(jur20)*(1+ps)/(beta*eei)+ gmotp1)*sqrt(2);
eps1[4]:= 0;
eps1[5]:= 0;
eps1[6]:= 0;
end;
if (rev1=3) and (rev1=4) then
begin
eps1[1]:= (sqrt(2/3)*sqrt(jur20)*(1+ps)/(beta*eei)+ gmotp1)*sqrt(2);
eps1[2]:= -0.5*(sqrt(2/3)*sqrt(jur20)*(1+ps)/(beta*eei)+ gmotp1)*sqrt(2);
eps1[3]:= -0.5*(sqrt(2/3)*sqrt(jur20)*(1+ps)/(beta*eei)+ gmotp1)*sqrt(2);
eps1[4]:= 0;
eps1[5]:= 0;
eps1[6]:= 0;
end;
if (rev1=2) and (rev1=5) then
begin
eps1[1]:= -(sqrt(2/3)*sqrt(jur20)*(1+ps)/(beta*eei)+ gmotp1)*sqrt(2);
eps1[2]:= 0.5*(sqrt(2/3)*sqrt(jur20)*(1+ps)/(beta*eei)+ gmotp1)*sqrt(2);
eps1[3]:= 0.5*(sqrt(2/3)*sqrt(jur20)*(1+ps)/(beta*eei)+ gmotp1)*sqrt(2);
eps1[4]:= 0;
eps1[5]:= 0;
eps1[6]:= 0;
end;
For i:=1 to 6 do
fur1[i]:=fur0[i]+fur00[i];
ccpi:=ccpi0+ccpi;
Assignfile(myfile,'Data.dat');
if fileExists('Data.dat')=true then
append(myfile)
else
Rewrite(myfile);
writeln(myfile,clnum,' ',eps1[1],' ',fur0[1],' ',gmotp1,' ',rev1);
closefile(myfile);
if (fgload=true) and (fgcount=true) and (fur0[1]>= cycq0) then
begin
  CLnum:=CLnum+1;
  fgcount:=false;
  if CLnum=(CLIntvNum + 1) * cycrecintv - cycrecnum Then CLIntvNum := CLIntvNum + 1;
end;
//
numdata:=numdata+1;
If numdata=0 then
Begin
```

```
StrGlst.RowCount:=2;
For i:=0 to StrGlst.ColCount-1 do
StrGlst.Cells[i,1]:='';
End;
If numdata>0 then
StrGlst.RowCount:=numdata+1;
For i:=1 to numdata do
Begin
Strglst.Cells[0,i]:=IntToStr(numdata);
Strglst.Cells[1,i]:=IntToStr(Clnum);
Strglst.Cells[2,i]:=FloatToStr(fur0[1]);
Strglst.Cells[3,i]:=FloatToStr(eps1[1]);
End;
//
if fgLoad=true then
begin
For i:=1 to 6 do
depsrev[i]:=deps1[i];
For i:=1 to 6 do
eps1[i]:=eps1[i]+depsrev[i];
For l:=1 to 6 do
Begin
dfur[l]:=0;
For m:=1 to 6 do
dfur[l]:=dfur[l]+dee1[l,m]*depsrev[m];
End;
ReturnYieldSurfaceRO
if fur0[1]>= (cycq0+cycqampl) then
begin
fgload:=false;
end;
end
else
begin
//
if fgLoad=false then
begin
For i:=1 to 6 do
depsrev[i]:=-deps1[i];
For i:=1 to 6 do
eps1[i]:=eps1[i]+depsrev[i];
For l:=1 to 6 do
Begin
dfur[l]:=0;
For m:=1 to 6 do
dfur[l]:=dfur[l]+dee1[l,m]*depsrev[m];
End;
ReturnYieldSurfaceRO
if fur0[1]<=(cycq0-cycqampl) then
fgload:=true;
fgcount:=true;
end;
end;
end;
```